

Designing and Building Microwave Metamaterials

by

Ruopeng Liu

Department of Electrical and Computer Engineering
Duke University

Date: _____

Approved:

David R. Smith, Advisor

Chris Dwyer

Steven Cummer

Qing H.Liu

Daniel Gauthier

Dissertation submitted in partial fulfillment of the requirements for the degree of
Doctor of Philosophy in the Department of Electrical and Computer Engineering
in the Graduate School of Duke University

2010

ABSTRACT
(Metamaterials)

Designing and Building Microwave Metamaterials

by

Ruopeng Liu

Department of Electrical and Computer Engineering
Duke University

Date: _____

Approved:

David R. Smith, Advisor

Chris Dwyer

Steven Cummer

Qing H.Liu

Daniel Gauthier

An abstract of a dissertation submitted in partial fulfillment of the requirements for
the degree of Doctor of Philosophy in the Department of Electrical and Computer
Engineering
in the Graduate School of Duke University
2010

Copyright © 2010 by Ruopeng Liu
All rights reserved except the rights granted by the
Creative Commons Attribution-Noncommercial Licence

Abstract

Metamaterials are a type of artificially structured materials. They are usually constructed with arrays of subwavelength conducting structures and can achieve electromagnetic properties beyond those of existing materials. Although the field of electromagnetic artificial media has been around since the 1940s, the new field of metamaterials has been heavily researched in the recent decade because of its promise of novel properties such as negative index of refraction and cloaking effect. In this dissertation, I discuss the concept of metamaterials and review the recent progress in microwave metamaterials research. The main achievement in this work has been to develop analytical formulas based on discrete Maxwell's equations to describe the dispersion behavior of metamaterial structures. The formulas have been verified by comparing with other physical models and numerical calculations. I make use of these analytical formulas to fit the response of metamaterial structures and to create rapid designs for metamaterial devices. Utilizing this technology, I design and fabricate practical metamaterial samples, such as an invisibility cloak. The experimental measurement of the metamaterial samples agrees well with design and thus demonstrates the efficiency and accuracy of the proposed sophisticated design methodology. This new design methodology will help transition fundamental metamaterial research to practical applications.

As the field of metamaterials highly relies on numerical simulation technology and physics modeling, I start my work from the design methodology, namely: build-

ing a structure, making a standard retrieval process and analyzing the achieved material parameters. In this study, I find that design efficiency is limited by the complexity of the unknown dispersion of metamaterials. To address this difficulty, I study the effective medium theory and spatial dispersion of metamaterials based on Maxwell's equations. Using the lattice model of periodic metamaterial structures, discrete Maxwell's equations are formulated by averaging the electric and magnetic field within a unit cell. A set of analytical formulas are thus derived to predict the spatial dispersion of a metamaterial structure with approximately ten fitting parameters. Subsequently, those fitting parameters can be used to represent the structure's response instead of complex dispersion curves. An abstract space is therefore created in which the geometrical dimensions of metamaterials can be varied. I perform full-wave simulations at a few points in this abstract space to estimate the values of the fitting parameters in-between the sampling points. A rapid design approach is thereupon initiated. This algorithm is further enhanced by Bayesian statistics by introducing advanced regression and searching techniques that facilitate the rapid design approach. To demonstrate the advantage of the rapid design approach, three different cylindrical cloaking devices are built by automatic design. The three cloaking devices work at 8.5 GHz, 9 GHz and 10 GHz, respectively, and measurements demonstrate the expected invisibility phenomenon for all three cloaks. The rapid design approach decreases the design time by at least a factor of a million in this experiment.

The next effort in this work is to integrate printed circuit board fabrication technology, rapid design approach and experimental design to implement various metamaterial devices at microwave frequencies. I discuss the implementation of waveguided metamaterials. This type of metamaterial is composed of complementary structures inside a planar waveguide and has an electric or magnetic response equivalent to the insertion of a material inside the waveguide. Lensing and tunneling

effects are demonstrated using integrated waveguided metamaterials. In addition, I also discuss gradient index metamaterials – a media whose properties vary with space. I demonstrate experimentally a beam-steering metamaterial lens and a focusing metamaterial lens using both narrowband resonant metamaterial structures and broadband non-resonant elements. The broadband metamaterial designs operate from 7 GHz to 12 GHz. In addition to these devices, I also construct and characterize a broadband ground-plane cloak operating from 13 GHz to 16 GHz, verifying both the design of broadband metamaterials and transformation optics.

Contents

Abstract	iv
List of Tables	ix
List of Figures	x
Acknowledgements	xviii
1 Literature Review and Introduction to Metamaterials	1
2 Effective medium theory and general fitting formulas for metamaterials	10
2.1 Effective medium theory for fundamental electric or magnetic resonant particles	10
2.2 A general fitting formula for metamaterials	19
2.3 A thin slab model and numerical analysis	24
2.4 Negative-index material composed of electric and magnetic resonators	42
3 Rapid design approach for metamaterials	50
3.1 Advanced rapid design of metamaterials	50
3.2 Advanced Bayesian statistics approach to metamaterial design	60
4 Waveguided metamaterials and electromagnetic tunnelling experiment	73
4.1 Concept of waveguided metamaterials	73
4.2 Integrating metamaterials into waveguide	76
4.3 Electromagnetic tunneling experiment by waveguided metamaterials .	84

5	Experiment on gradient index metamaterials	104
5.1	Concept of gradient index metamaterials	104
5.2	Gradient index lens by ELC structures	106
5.3	Broadband gradient index metamaterials and complex lens design . .	111
5.4	Random gradient index metamaterials	123
6	Cloaking Devices Design and Experiment	128
6.1	Introduction to transformation optics	128
6.2	Invisibility cloak design in free space	132
6.3	Broadband ground-plane cloak	136
A	Appendix A	150
	Bibliography	157
	Biography	162

List of Tables

5.1	An optimized solution on the beam steering gradient index design from rapid design system	110
5.2	The predicted and actual zero-frequency permittivity values as a function of the unit cell dimension, a.	113

List of Figures

1.1	An external electric field excites dipoles inside a material	2
1.2	An split ring resonator on the substrate.	2
1.3	A collection of SRRs forming a homogeneous metamaterial	4
1.4	A comparison of the permeability in a Drude-Lorentz magnetic medium and a metamaterial composed by [composed of] SRRs	6
1.5	From Ref.[19]. The effect of partial focusing by indefinite medium	7
1.6	From Ref.[20]. The design of gradient index metamaterials by placing inhomogeneous SRRs transverse to the propagation direction	8
1.7	From Ref.[25]. The design of a reduced parameter invisible cloak and the simulations and measurements of a cloak and metal cylinder	9
2.1	Metamaterial composed of periodic particles, where a plane wave is incident along the z direction.	12
2.2	Comparison of theoretical-prediction results and retrieval results from S parameters for the SRR structure. The parameters used in the theoretical calculation are chosen as $f_0 = 9.975GHz$, $\varepsilon_a = 4.4\varepsilon_0$, $\mu_a = \mu_0$, $\gamma = 5 \times 10^7$, $p = 2.5$ mm, and $F=0.23$. The SRR structure is inserted in (b). The substrate is FR4 ($\varepsilon = 4.4 + 0.044i$) with a thickness of 0.25mm. The dimensions are: $a = 2.5$ mm, $c = 2.2$ mm, $g = 1.1$ mm, $b = e = 0.2$ mm and $d = f = 0.22$ mm. Ref.[7]	17
2.3	The ELC Structure. Comparison of the theoretical-prediction results and the retrieval results from the S scattering parameters for the ELC structure. The parameters used in the theoretical calculation are that $f_0 = 12.2GHz$, $\varepsilon_a = 4.2\varepsilon_0$, $\mu_a = \mu_0$, $\gamma = 4 \cdot 10^7$ $p = 3.333mm$ and $F=0.19$ The substrate is FR4 ($\varepsilon = 4.4 + 0.001i$) whose thickness is 0.2026mm. The dimension is that $a=3.333mm$, $b=3mm$, $c=d=g=f=0.2mm$ and $e=1.4mm$ Ref[7]	18

2.4	A full wave simulation on [simulation of an] an SRR structure and the extracted permittivity and permeability from 5 GHz to 30GHz	21
2.5	A numerical particle retrieval on an SRR structure. The spatial dispersion effect can be removed by using the generalized formula	23
2.6	Fitting the response of the SRR-ELC NIM particle structure. Ref.[4] . . .	25
2.7	Particle retrieval to a 4-cell combination structure. (a) 4-cell-combination structure, and (b) 4 cells in the combination structure. The combination structure is generated from a SRR-ELC NIM particle (Ref[4]) by shortening the ELC's arm and shrinking the SRR's gap in half and attaching it to the other side of the substrate, (c)-(d) the effective permittivity and permeability by numerical simulation (e)-(f) particle retrieval for ϵ_m and μ_m	26
2.8	The configuration of the thin slab model	27
2.9	Calculation of metamaterial parameters by using both the thin slab model and the field averaging approach	29
2.10	Field distribution in the thin slab model	31
2.11	Field distribution by the field averaging assumption	31
2.12	A practical SRR structure model created with the full wave simulation software. The numerical solution on the S-parameter is shown. The maximum transmission frequency is 8.5GHz	32
2.13	Numerical observation of the field distribution on an SRR structure . . .	33
2.14	Electric and magnetic field distribution extracted from the full wave simulation	33
2.15	Comparison of the polar field plot between the thin slab model and the assumption	34
2.16	Numerical Eigen-mode solution of the SRR and the electric and magnetic field distribution	35
2.17	The wave impedance along the propagation direction calculated by the thin slab model	36
2.18	The field distribution within a unit cell by the thin slab model, the Eigen-mode solution on 3D SRR, and the field assumption	36

2.19	Eigen-mode solution on a nearly 2D SRR structure. Notice that the wave is propagating along the z-axis. To get a continuous field, we leave a tiny gap on the x-axis and observe the field distribution in that gap.	37
2.20	We compared the A and F values by using the thin slab model and the assumption in Section 2.2	37
2.21	We compare the impedance calculated by three different methods	38
2.22	We compared the average parameters	38
2.23	A full wave simulation on the six SRR slab	39
2.24	The electric and magnetic field distribution solved by full wave simulation software	40
2.25	Field plot along the propagation direction	40
2.26	A full wave simulation on the six ELC slab	41
2.27	The electric and magnetic field distribution solved by full wave simulation software	41
2.28	SRR and ELC composite structures [10]	43
2.29	Retrieval of (a) SRR's permeability; (b) ELC's permittivity (c) SRR-ELC's index (d) SRR-ELC's impedance [10]	45
2.30	Phase variation in a (a) positive index regime; (b) negative index region (c) zero-index region [10]	46
3.1	Flow chart of rapid design approach for metamaterials	55
3.2	SRR unit cell structure	55
3.3	Particle retrieval of SRR unit cell structure	56
3.4	Reconstruction curve from particle retrieval	58
3.5	Calculation on SRR unit cell structure	59
3.6	Nonlinear regression on the parameters' response in SRR design	60
3.7	Prediction of the SRR's response is indicated by the colored line, compared to the full wave simulation, indicated by the solid line.	61
3.8	The impedance design at a particular point in the search process.	62

3.9	The index design at a particular point in the searching process. The lowest valley indicates the optimized location in the space	62
3.10	Demonstration of SMC approach to design a gradient index media	63
3.11	Refractive index value changing [changes with] with the dimension s and r.	63
3.12	The optimization of the gradient index design from n=2.3 to n=3.6 by ten layers	64
4.1	Configuration of waveguided metamaterials[58]	74
4.2	Retrieval results, dimensions of CSRRs and simulation setup. (a) Extracted permittivity and CSRRs' dimensions, in which, a=3.333 mm, b=3 mm, c=d=0.3 mm and f=1.667 mm. (b) Simulation configuration for CSRR unit cell. d=11 mm, h=1 mm and L=23.333 mm [63]	75
4.3	The CSRR structure and retrieval results, in which rr=0.6 mm,w=0.25 mm, g=0.25 mm, l=3.2 mm, $a_x=3.45$ mm, and $a_z=3.5$ mm.[58]	77
4.4	Relationship between the dimension rr in CSRR and its effective index and impedance.[58]	77
4.5	Experimental configuration[58]	78
4.6	2D field mapping for beam steering gradient index lens and focusing gradient index lens[58]	78
4.7	The CELC structure is chosen as the unit cell to realize the indefinite metamaterial.[59]	81
4.8	(a) The experimental setup for the partial focusing. (b) Details of the fabricated CELC[59]	93
4.9	Simulation setups for the the anisotropic CELC unit when the plane waves are incident from two directions.[59]	94
4.10	The effective permittivity and permeability curves for the simulation setup in Fig. 4(a). (a) ϵ_z . (b) μ_x .[59]	95
4.11	The effective permittivity and permeability curves for the simulation setup in Fig. 4(b). (a) ϵ_z . (b) μ_y .[59]	95
4.12	The distribution of simulated electric fields in a section of the planar waveguide at 11.5 GHz.[59]	96
4.13	The experimental result for the electric-field distributions inside the 2D mapper at 11.5 GHz.[59]	97

4.14	Figure from Ref.[63], the configuration of electromagnetic waves' tunnelling through narrow channel	98
4.15	Figure from Ref.[63], electromagnetic wave tunnel through a narrow channel as U-turn	98
4.16	Experimental setup, in which $h=11$ mm, $hw=10$ mm, $d=18.6$ mm (16.6 mm for CSRR Regime), $w=200$ mm. Lower figure is the sample inside chamber. [60]	98
4.17	Configuration of tunneling effect simulation[60]	99
4.18	Poynting vector and medium model (a) Poynting vector (b) Simplified Model[60]	99
4.19	Experimental, theoretical and simulated transmissions for the tunneling and control samples. [60]	99
4.20	2-D Mapper results at 8.04 GHz. (a) Field distribution of tunneling sample (b) Field distribution of control[60]	100
4.21	Phase Shift for 5 unit-cell tunneling sample at 8.04 GHz and control at 7 GHz.[60]	100
4.22	The circuit tunneling structure. (a) Top layer. (b) Middle layer. (c) Bottom layer. (d) Side view. (e) Top and bottom views of the fabricated circuit.[67]	101
4.23	(a) The effective permittivity for CSRR (inset: the CSRR structure). (b) The measured and simulated S parameters for the tunneling structure shown in Fig.4.22 without any patterns on the bottom metallic layer. (c) The measured and simulated reflection coefficients S11 for the tunneling structure shown in Fig.4.22. (d) The measured and simulated transmission coefficients S21 for the tunneling structure shown in Fig.4.22.[67]	102
4.24	A circuit bend using the tunneling structure. Left: top view. Right: bottom view[67]	102
4.25	The measured and simulated S parameters for the circuit bend shown in Fig.4.24 with/without CSRR patterns on the bottom. (a) S11 without CSRR patterns. (b) S21 without CSRR patterns. (c) S11 with CSRR patterns. (d) S21 with CSRR patterns.[67]	103
5.1	From Ref.[18]. The design of gradient index metamaterials by placing inhomogeneous SRRs transverse to propagation direction	106
5.2	An ELC structure that has electric resonance. The change of geometry parameter s and r can lead to varies on the quantity of the response.	107

5.3	The effective electromagnetic parameters of an ELC structure with the periodicity 3.333mm and s=0.835mm and r=0.28mm	108
5.4	The effective electromagnetic parameters of an ELC structure with the periodicity 3.333mm and s=0.32mm and r=0.43mm	109
5.5	A field mapping in experiment on the ELC gradient index lens	111
5.6	(a) Retrieved permittivity for a metamaterial composed of the repeated unit cell shown in the inset; (b) retrieved permeability for a metamaterial composed of the repeated unit cell shown in the inset. (c) The distortions and artifacts in the retrieved parameters are due to spatial dispersion, which can be removed to find the Drude-Lorentz like resonance shown in the lower figure.[54]	113
5.7	Retrieval results for the closed ring medium. In all cases the radius of curvature of the corners is 0.6 mm, and w=0.2 mm. (a) The extracted permittivity with a=1.4 mm. (b) The extracted index and impedance for several values of a. The low frequency region is shown. (c) The relationship between the dimension a and the extracted refractive index and wave impedance. [54]	114
5.8	Refractive index distributions for the designed gradient index structures. (a) A beam-steering element based on a linear index gradient. (b) A beam focusing lens, based on a higher order polynomial index gradient. Note the presence in both designs of an impedance matching layer (IML), provided to improve the insertion loss of the structures.	115
5.9	Refractive index distributions for the designed gradient index structures. (a) A beam-steering element based on a linear index gradient. (b) A beam focusing lens, based on a higher order polynomial index gradient. Note the presence in both designs of an impedance matching layer (IML), provided to improve the insertion loss of the structures.[54]	116
5.10	Fabricated sample, in which, the metamaterial structures vary with space coordinate.[54]	117
5.11	Field mapping measurements of the beam steering lens. The lens has a linear gradient that causes the incoming beam to be deflected by an angle of 16.2 degrees. The effect is broadband, as can be seen from the identical maps taken at four different frequencies that span the X-band range of the experimental apparatus.[54]	118

5.12	Field mapping measurements of the beam focusing lens. The lens has a symmetric profile about the center (given in the text) that causes the incoming beam to be focused to a point. Once again, the function is broadband, as can be seen from the identical maps taken at four different frequencies that span the X-band range of the experimental apparatus.[54]	119
5.13	Index distribution of gradient random medium	123
5.14	The fabricated sample on the designed random gradient index metamaterials	124
5.15	2D mapping result for gradient random medium	125
5.16	Angular resolution detection of gradient random medium	126
6.1	An example of a coordinate transform	129
6.2	From Ref.[25]. The design of reduced parameter invisible cloak and the simulations and measurements of cloak and metal cylinder, in which, A. ideal simulation B. simulation on reduced cloak, C. control experiment D. experiment on the reduced cloak	131
6.3	Rapid design for a reduced cloak, working at 10GHz	133
6.4	Fabricated invisible cloak by rapid design system	133
6.5	Invisible cloak measurement	134
6.6	The transformation optics design for carpet cloak embedded with background materials and impedance matching layers. The white part is the object supposed to be hid and meshing line indicates the quasi-conformal mapping. The color map shows the designed refractive index distribution.[26]	137
6.7	The unit cell design of the non-resonant element and fabricated sample according to the relationship between the geometry dimension and effective index.[26]	138
6.8	Effective permittivity, permeability, impedance and refractive index of I-Shape unit-cell with the dimension a=1.4mm.[26]	140
6.9	Ground-plane cloak mask (transformation region) generated by automatic design system. Not shown here are the cutting outlines, with slots for assembly, around which each strip (5 unit cells, 10mm, in height) is cut out by circuit board prototype milling machine (LPRF)[26]	142

6.10	Ground-plane cloak mask (Experimental apparatus for the ground-plane cloak measurement. The apparatus consists of two metal plates separated by 1cm, which form a 2 dimensional planar waveguide region.[26]	143
6.11	Measured field mapping (E-field) of the ground, perturbation and ground-plane cloaked perturbation. The rays display the wave propagation direction and the dash line indicates the normal of the ground in the case of free space and that of the ground-plane cloak in the case of the transformed space. (A) a collimated beam incident on the ground plane at 14GHz, (B) a collimated beam incident on the perturbation at 14GHz (control), (C) a collimated beam incident on the ground-plane cloaked perturbation at 14GHz, (D) a collimated beam incident on the ground-plane cloaked perturbation at 13GHz, (E) a collimated beam incident on the ground-plane cloaked perturbation at 15GHz, (F) a collimated beam incident on the ground-plane cloaked perturbation at 16GHz.[26]	145
6.12	Measured field magnitude (E-field) of the ground, perturbation and ground-plane cloaked perturbation. The rays display the wave propagation direction and the dash line indicates the normal of the ground in the case of free space and that of the ground-plane cloak in the case of the transformed space. (A) a collimated beam incident on the ground plane at 14GHz, (B) a collimated beam incident on the perturbation at 14GHz (control), (C) a collimated beam incident on the ground-plane cloaked perturbation at 14GHz, (D) a collimated beam incident on the ground-plane cloaked perturbation at 13GHz, (E) a collimated beam incident on the ground-plane cloaked perturbation at 15GHz, (F) a collimated beam incident on the ground-plane cloaked perturbation at 16GHz.[26]	146
6.13	2D field mapping (E-field) of the perturbation and ground-plane cloaked perturbation, illuminated by the waves from the left side (A) perturbation, (B) ground-plane cloaked perturbation. The grid pattern indicates the quasi-conformal mapping of the transformation optics material parameters.[26]	147
6.14	Power plot of the standing waves of the carpet cloak and control by simulation and experiment. (a) simulated power plot of only ground at 14GHz (b) simulated power plot of carpet cloak at 14GHz (c) simulated control scatter at 14GHz (d) experimental power plot of only ground at 14GHz (e) experimental power plot of carpet cloak at 14GHz (g) experimental power plot of control scatter at 8GHz (h) experimental power plot of carpet cloak at 8GHz[26]	149
A.1	Metamaterial composed of periodic particles, where a plane wave is incident along the z direction.	151

Acknowledgements

I'd love to show my great gratitude to my advisor Dr. David Smith for his great support and all the committee members for your service to my thesis defense. I'd also want to thank my wife Weizi Huang and my parents for their endless support.

Literature Review and Introduction to Metamaterials

Electromagnetic metamaterials have received attention from the scientific community recently because of their novel properties, properties which are not easily found in natural materials. Metamaterials are normally constructed from subwavelength structures. The subwavelength structure, or unit cell, can respond to either electric fields or magnetic fields, and thus resemble the dipole moments in natural materials. Fig.1.1 illustrates a material's electric response, in which a collection of dipoles react to an external electric field. In natural materials, the dipole response is attributed to the molecules in the material. To achieve different material parameters, one can find different chemical species or artificially create a hybrid medium by mixing various materials. Dielectric materials and optical materials have been widely used and even engineered in sophisticated ways for many applications. However, these materials' properties are still limited by the choice of chemical species. To address this challenge, the methodology of metamaterials attempts to engineer a material's property through its sub-level particle, or unit cell. A sub-wavelength unit cell structure can be used to generate a dipole response. Fig. 1.2 shows one of the candidates for such a

unit cell structure, called a Split Ring Resonator(SRR), whose functionality will be discussed in detail later. Because the metamaterial's properties can be engineered by modifying each individual unit cell, the advantage of a metamaterial derives from its flexibility in achieving various functionalities.

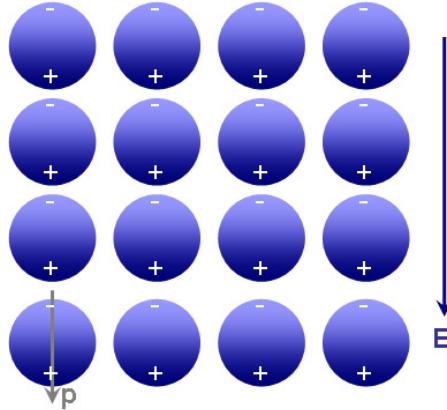


FIGURE 1.1: An external electric field excites dipoles inside a material

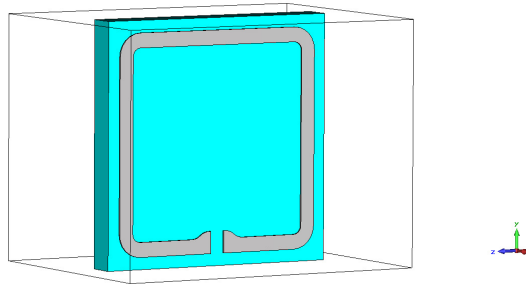


FIGURE 1.2: An split ring resonator on the substrate.

To characterize an electromagnetic material, we can study the classical description of electromagnetic media, a constitutive relationship. As shown in Fig.1.1, we can average the field intensity and strength to obtain the local response by the dipole moment inside the media.

$$\begin{aligned}\overline{D} &= \epsilon_0 \langle \overline{E} \rangle + \overline{P} \\ \overline{B} &= \mu_0 (\langle \overline{H} \rangle + \overline{M})\end{aligned}\tag{1.1}$$

in which, $\langle \bar{E} \rangle$ and $\langle \bar{H} \rangle$ are the statistical average of the local electric and magnetic field. \bar{D} and \bar{B} are the electric and magnetic net flux from the the interaction of the external field and the material's response. \bar{P} and \bar{M} are the polarization and magnetization, respectively. For linear electromagnetic materials, we can assume that \bar{P} is proportional to $\langle \bar{E} \rangle$ and \bar{M} is proportional to $\langle \bar{H} \rangle$. Then the electric and magnetic susceptibility χ_e and χ_m can be defined as $\bar{P} = \epsilon_0 \chi_e \langle \bar{E} \rangle$ and $\bar{M} = \chi_m \langle \bar{H} \rangle$. By grouping the susceptibility with the local field in Eq.(1.1), we obtain the definition of the permittivity $\epsilon = \epsilon_0(1 + \chi_e)$ and permeability $\mu = \mu_0(1 + \chi_m)$. Recall that the permittivity and permeability are the most important macro parameters to describe an electromagnetic material's properties. The wave propagation can be solved by Maxwell's Equations based on ϵ and μ . The entire process of extracting the macro parameter ϵ and μ from the polarization and magnetization is regarded as a homogenization approach on the effective medium.

The critical point is that a homogenous electromagnetic medium can be formed by a collection of subwavelength scatters, whose optical properties can be characterized by the field averaging technique. The methodology for creating metamaterials follows the same procedure but by replacing the molecule with an artificial subwavelength structure, shown in Fig.1.3.[1] An array of subwavelength SRRs can form a metamaterial with a certain magnetic response. As discussed previously, the ϵ and μ of the metamaterial depends on the dipole moment generated by the unit cell structure. Therefore, modifying the geometry of a particular unit cell structure can render the local optical property of metamaterial designable.

To analyze the structure of metamaterials, we propose an approximate model to describe the mechanism of forming such artificial media. Fig.1.3 shows a two-dimensional split ring resonator structure from different perspectives. Assuming the unit cell structure is arrayed within the entire space with the periodicity p , a uniform magnetic field $H_0 e^{-i\omega t}$ is applied along the $-z$ axis. According to Lenz's Law, an

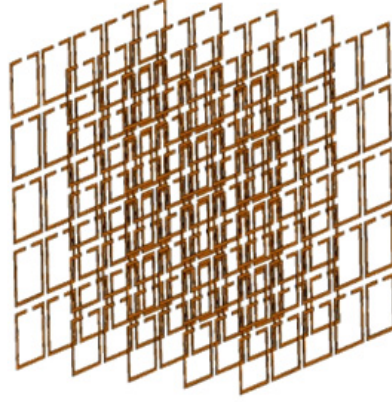


FIGURE 1.3: A collection of SRRs forming a homogeneous metamaterial

induced current will be excited I . We assume that the magnetic field intensity caused by the induced current is H_1 . Notice that H_1 is a function of the position (x, y, z) and is the contribution from all the array. The depolarization field is H_2 and has the same character as H_1 . It is easy to show that

$$\int_{-p/2}^{p/2} \int_{-p/2}^{p/2} (H_{1z} + H_{2z}) dx dy = 0 \quad (1.2)$$

in which H_{1z} and H_{2z} indicate the z-axis component of H_1 and H_2 . According to the field average [field averaging technique?] technique[1], we define the average permittivity as

$$\bar{\mu} = \frac{\overline{B}}{\overline{H}} = \frac{\frac{1}{p^2} \int_{-p/2}^{p/2} \int_{-p/2}^{p/2} B_z dx dy}{\frac{1}{p} \int_{-p/2}^{p/2} H_z dz} \quad (1.3)$$

To calculate the average magnetic flux, we can write

$$\overline{B} = \frac{1}{p^2} \int_{-p/2}^{p/2} \int_{-p/2}^{p/2} B_z dx dy = \frac{1}{p^2} \int_{-p/2}^{p/2} \int_{-p/2}^{p/2} \mu_0 (H_0 + H_1 + H_2) dx dy = \mu_0 H_0 \quad (1.4)$$

The average magnetic intensity can be calculated by

$$\overline{H} = \frac{1}{p} \int_{-p/2}^{p/2} H_z dz = \frac{1}{p} \int_{-p/2}^{p/2} (H_0 + H_2) dz = H_0 + \frac{1}{p} \int_{-p/2}^{p/2} H_2 dz \quad (1.5)$$

. For practical structures, H_2 is difficult to calculate because of the unit cell interaction and the integral of the contribution from the entire array. Therefore, a full wave simulation is usually needed to solve such complex scatter systems. However, to demonstrate the concept and the field averaging technique, we discuss a simplified model to predict the SRR's response.[1] Let's assume that the unit cell is a two-dimensional structure and is small in the $x - y$ plane. The H_{1z} is uniform within the split ring area and H_{2z} is uniform within the entire unit cell. We can then calculate the local field within the split ring area:

$$B_{loc} = H_0 + H_{1z} + H_{2z} \quad (1.6)$$

. H_{1z} is excited by the induced current. It can be approximated as $H_1 = I$ according to Eq.1.2, $H_{2z} = -\frac{S_0}{S_1}H_{1z}$, in which S_0 is the area of a split ring resonator and $S_1 = p^2$ is the unit cell area.

According to Lenz's Law, we establish a circuit calculation that

$$i\omega B_{loc}S_0 = I(R - 1/i\omega C) \quad (1.7)$$

Solving Eq.1.2-1.7, we can see that

$$\bar{\mu} = \mu_0 \left(1 - \frac{F\omega^2}{\omega^2 - \omega_0^2 + i\gamma\omega} \right) \quad (1.8)$$

in which, $F = \frac{S_0}{S}$, $\omega_0 = \frac{1}{\sqrt{\mu_0 S_0 C}}$ and $\gamma = \frac{R}{\mu_0 S_0}$.

It might be helpful to compare metamaterials with existing natural materials. They are both constructed by subwavelength scatters, and their optical properties are both described by ϵ and μ . The distinction is the unit cell component. A resonator is needed to form a metamaterial unit cell. Thus, the fabrication technique in reality limits the unit cell's size. Normally the unit cell is much larger than the molecule in a dielectric material. At microwave frequencies, the scale of a metamaterial's unit cell is

usually one-tenth of the wavelength. This difference underlies the distinction between metamaterials and natural materials in physics.[2, 3, 4] Because the metamaterial unit cell scale has been comparable to the wavelength, it also behaves like a photonic crystal. Much effort has been devoted to explaining and describing the unusual dispersion relationship.[4, 5, 6, 7, 8] It has been noted that a large unit cell size will introduce a spatial dispersion (dispersion depending on the lattice factor) into a metamaterial’s properties. Fig. 1.4 illustrates a comparison between a Drude-Lorentz media dispersion and a metamaterial dispersion. A dispersion in existed materials can be usually calculated using a Drude-Lorentz model. While the metamaterial’s dispersion can be calculated by a full wave simulation and a parameter retrieval process.[2, 6] From Fig.1.4, we can observe the dramatic distortion in the permeability dispersion of metamaterials. Such distortion results in a more complex response compared to that of natural materials. To address the difficulty in describing this spatial dispersion and to provide a set of general fitting formulas, we provide our approach to this problem in Chapter 2.

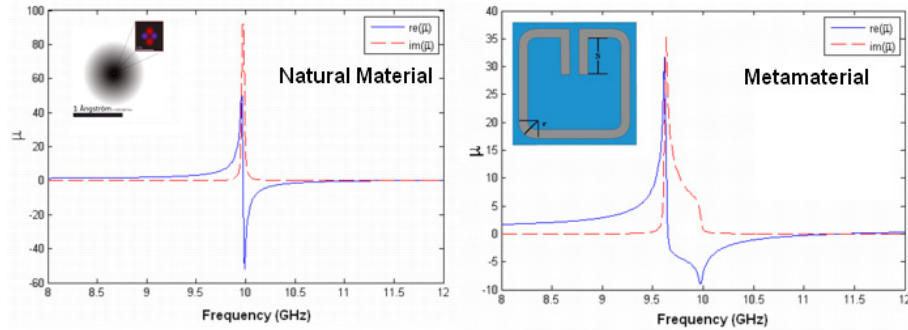


FIGURE 1.4: A comparison of the permeability in a Drude-Lorentz magnetic medium and a metamaterial composed by [composed of] SRRs

Although designing metamaterials is still complex, it has been demonstrated that metamaterials can exhibit novel electromagnetic properties which are impossible or difficult to find in existing materials. One of the compelling technologies based on metamaterials is a negative index material that has a permittivity and permeability

which are simultaneously negative.[9] The first experiment with a negative index material was reported in 2000, in which a SRR with a wire structure was used to form a negative index at microwave frequencies.[10] Since this demonstration, many experiments have been done based on negative index material technology.[10, 11, 12, 13] One of the most controversial topics is the super lens composed by the negative permittivity or permeability, or both, in metamaterials[14, 15]. The diffraction limit of optical imaging theory is predicted to be overcome by enhancing the evanescent waves using negative index materials. Disagreement ensued after more careful study [15] and the theorem for a super lens was improved by the debate[16]. The first experiment on an optical super lens was demonstrated by Professor Xiang Zhang's group at the University of California, Berkeley, in 2005 [17]. By using a $17nm$ silver slab, they achieved a $1/6$ wavelength imaging resolution.

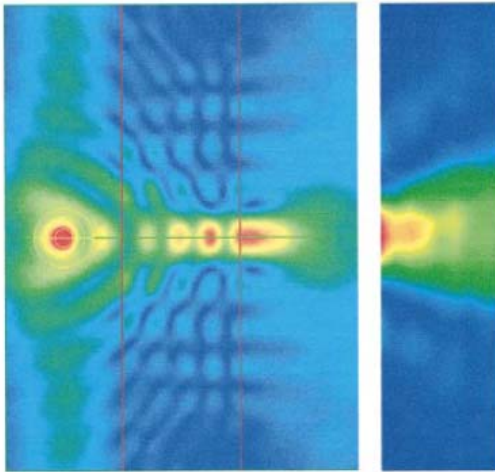


FIGURE 1.5: From Ref.[19]. The effect of partial focusing by indefinite medium

Research on negative index media, or indefinite media [18, 19], produced another type of metamaterial with negative permittivity or permeability in one direction and positive in the other direction. Such anisotropic media can achieve partial focusing due to their interesting dispersion diagram, as shown in Fig.1.8. Indefinite media are only one example of the complex anisotropic materials that can be designed by

metamaterial technology.

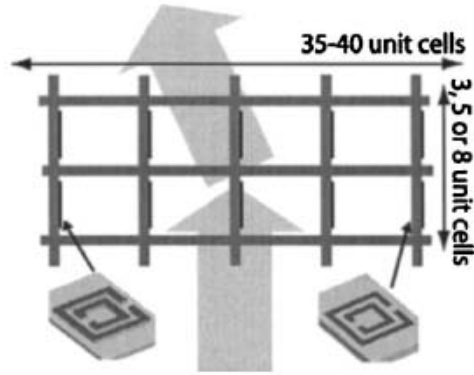


FIGURE 1.6: From Ref.[20]. The design of gradient index metamaterials by placing inhomogeneous SRRs transverse to the propagation direction

As discussed above, the unit cell design largely determines the local electromagnetic properties of metamaterials. By varying the unit cell geometry, the refractive index and impedance can be engineered throughout a metamaterial. A gradient index metamaterial was firstly demonstrated in 2004, shown in Fig. 1.9[20]. The slight variation in the substrate cut forms an inhomogeneous electromagnetic medium. More recent work on the gradient index lens design will be discussed in Chapter 5.

Thus, the ability to modify each resonant particle in a structure allows investigators to explore unusual electromagnetic properties not found in natural materials. There are other examples of negative index materials [10, 11] or even much more complicated inhomogeneous anisotropic medium systems which can control the wave propagation around a designated region, e.g. the invisible cloak[24, 25, 26] shown in Fig.1.2.

Since the resonant frequency is related to the unit cell size, scaling down the structure can lead to a higher frequency response, via terahertz metamaterials for example [21, 22]. Although this scaling technique is affected by the effective mass of the electron, which will limit the maximum resonant frequency[23], it is still a useful technique to control operational frequency of metamaterials. Recently many optical

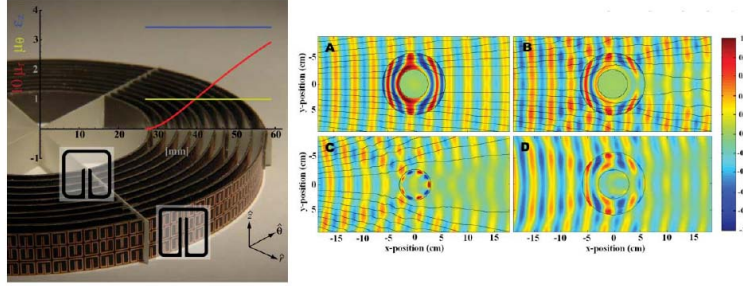


FIGURE 1.7: From Ref.[25]. The design of a reduced parameter invisible cloak and the simulations and measurements of a cloak and metal cylinder

metamaterials also have been demonstrated using this technology.[22, 23, 24, 25]

A technique, transformation optics, has been proposed most recently to control electromagnetic waves via the design of complex media.[24, 25, 26, 27, 28, 29, 30, 31, 32, 33, 34] The idea is to utilize certain complex media to realize the coordinate transform to electromagnetic waves. Such complex media are usually anisotropic and inhomogeneous, and thus difficult to find in nature. Metamaterials become a useful element candidate to form such complex media. One of the most fascinating studies is the research on an invisibility cloak that can control the electromagnetic wave propagation that avoid an object as if the object were absent.[25] Fig.1.7 shows the first experiment on a reduced cloak.

In conclusion, the concept of metamaterials is established from effective media theory and field averaging in a homogenization process. The flexibility afforded in engineering their optical properties make metamaterials attractive for the development of novel electromagnetic devices. Experimental demonstrations of metamaterials have presented the possibility of a negative index and an invisibility cloak at microwave frequencies.

Effective medium theory and general fitting formulas for metamaterials

2.1 Effective medium theory for fundamental electric or magnetic resonant particles

As discussed in the Introduction, practical metamaterial structures behave differently from conventional dielectric materials due to the spatial dispersion. This fact introduces difficulties when describing metamaterial behavior. In this section we will develop an effective medium theory for fundamental electric or magnetic resonant particles and explain the physics behind their dispersion behavior.

First I will review the history of artificially structured electromagnetic metamaterials, which have received considerable attention in the past several years due to their ability to exhibit a wide range of electromagnetic responses rarely found in natural materials or composites. Since the demonstration of an artificial medium with a negative refractive index in 2000 [11], metamaterial designs have increased in complexity and sophistication, to the point that precisely controlled gradients in both permittivity and permeability can be introduced to form advanced lenses and optics [16], or even invisibility cloaks [24, 25, 26], according to Ref.[7].

While not a necessary requirement, periodicity is a feature typically found in metamaterials, which are usually based on repeated unit cells containing one or more conducting subwavelength resonators. Unlike photonic crystals, the unit cell size in metamaterials is much smaller than the free-space wavelength, so that an inhomogeneous structure can be homogenized from an electromagnetic point of view, and be represented by its macro-scale parameter permittivity and permeability[7].

Although the use of effective constitutive parameters has proved successful in describing and predicting the properties of waves propagating in metamaterials, the retrieved parameters nevertheless display anomalous and often non-intuitive behavior. For example, it was found from scattering- (S-) parameter simulations that when either the retrieved permittivity or permeability possesses a resonance form, there is an accompanying anti-resonance in the non-resonant parameter over the same frequency range, with the sign of the imaginary part of the anti-resonant parameter opposite to that of the resonant parameter [35]. Considerable discussion has ensued over the applicability of retrieval methods and even the validity of effective constitutive parameters in general, for metamaterial structures [36, 37].(Ref.[7])

The unusual form of the constitutive parameters obtained from retrieval methods has recently been analyzed with increasing rigor by numerous researchers [5, 38, 39, 40, 41]. The consensus that has emerged is that the periodicity associated with most reported metamaterials, usually a factor of ten smaller than the free-space wavelength, plays a significant role in the metamaterial properties. As a result, the closed form expressions obtained by researchers in the static and quasi-static limits for the constitutive parameters [1, 42, 43], which typically obey Drude or Drude-Lorentz models, must be modified to include the effects of spatial dispersion.[7, 38]

Before those work, there has not been an analytical approach that connects the simple medium dispersion models to the actual retrieved parameters of the metamaterial structures. As a result, the detailed design of metamaterials has relied entirely

on numerical approaches that first solve Maxwell’s equations for a structure, and then perform a numerical retrieval to obtain the effective constitutive parameters. Well known effective medium approaches can be used to form an initial metamaterial design and develop a working intuition, but do not predict the ultimate frequency-dependent form that the actual parameters will take. Our aim here is to present an analytical theory that provides a simplified yet accurate description of metamaterials, and is also entirely consistent with previous numerical approaches.[7]

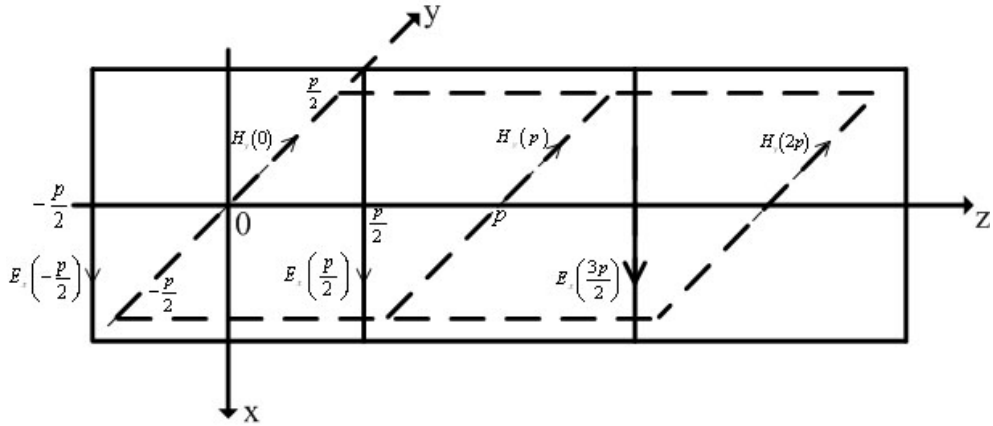


FIGURE 2.1: Metamaterial composed of periodic particles, where a plane wave is incident along the z direction.

Recently, a rigorous approach to the numerical retrieval of the constitutive parameters was presented, in which field averages over the metamaterial unit cell were used to determine the macroscopic fields [5]. (A similar approach has also been applied to the transmission line formulation of metamaterials [44]). This process results in a discrete form of Maxwell’s equations, in which the metamaterial unit cell is replaced by an effective medium. The discrete set of equations, however, implies that the fields are effectively sampled on a finite grid, so that spatial dispersion is inherent in the formulation. Although ultimately a numerical implementation, the method presented in [5, 47, 48] forms a useful starting point for the present discussion[7].

If we start with the integral form of Maxwell’s equations, and imagine averaging

the fields over a unit cell, we arrive at a finite-difference form of Maxwell's equations, in which the averaged electric fields are defined on the edges of one cubic lattice, while the averaged magnetic fields are defined on the edges of a second offset lattice [45]. To simplify the analysis, we assume a wave whose electric field is polarized in the x direction and propagates along the z axis. The unit cell of the metamaterial is assumed to have a periodicity p . Under these conditions, one of the Maxwell curl equations reduces to

$$\overline{E}_x[(n + 1/2)p] - \overline{E}_x[(n - 1/2)p] = i\omega\overline{\mu}p\overline{H}_y[np], \quad (2.1)$$

in which $n = 0, \pm 1, \dots$, and the averaged electric field \overline{E}_x and magnetic field \overline{H}_y are defined by the line integrals

$$\overline{E}_x(z) = \frac{1}{p} \int_{-p/2}^{+p/2} E(x, 0, z) dx, \quad (2.2)$$

$$\overline{H}_y(z) = \frac{1}{p} \int_{-p/2}^{+p/2} H(0, y, z) dy. \quad (2.3)$$

. Under this form of averaging, the average permeability $\overline{\mu}$ has the form [8]

$$\overline{\mu} = \frac{1}{p^2\overline{H}_y(0)} \int_{-p/2}^{+p/2} \int_{-p/2}^{+p/2} \mu_a H(x, 0, z) dx dz. \quad (2.4)$$

.

Similarly, the other Maxwell curl equation in integral form can be simplified to

$$\overline{H}_y[(n + 1)p] - \overline{H}_y[(np)] = i\omega\overline{\varepsilon}p\overline{E}_x[(n + 1/2)p] \quad (2.5)$$

after introducing the average permittivity

$$\overline{\varepsilon} = \frac{1}{p^2\overline{E}_x(p/2)} \int_{-p/2}^{+p/2} \int_{-p/2}^{+p/2} \varepsilon_a E(0, y, z) dy dz. \quad (2.6)$$

. In Eqs. (2.4) and (2.6), ε_a and μ_a are the permittivity and permeability of the background medium, respectively. Eqs. (2.1) and (2.5) together represent a discrete set of Maxwell's equations (DME)[7].

In order that the DME represents an infinite periodic structure, we apply the Bloch boundary conditions: $\overline{E}_x[(n + 1/2)p] = \overline{E}_x[p/2]e^{i(n\theta+\theta/2)}$ and $\overline{H}_y[(np)] = \overline{H}_y[0]e^{in\theta}$, in which θ is the phase advance across one cell. Substituting the boundary conditions into the DME, we obtain the dispersion equation

$$\sin(\theta/2) = S_d \omega p \sqrt{\overline{\mu\varepsilon}}/2, \quad (2.7)$$

where $S_d = 1$ if the wave is propagating in a material where $\overline{\varepsilon}$ and $\overline{\mu}$ are both positive, and $S_d = -1$ if the wave is propagating in a material where $\overline{\varepsilon}$ and $\overline{\mu}$ are both negative. Eq.(2.7) shows that the phase advance is related not only to the average constitutive parameters, but also to the periodicity p . [7]

N.b. I'm not going to put periods after the citation hereafter, since these may be footnotes, not citations as in a journal article.

To obtain a complete description of wave propagation in a medium, it is also necessary to determine the wave impedance of the medium, which is defined as $\eta(z) = \overline{E}_x(z)/\overline{H}_y(z)$. Part of the difficulty in obtaining an analytic expression for the averaged impedance is that averaged electric and magnetic fields for the effective finite-difference Maxwell's equations are defined on the edges of lattices that are offset from each other, whereas the definition of impedance requires the ratio of the electric and magnetic fields at the same point. We state without justification here that we can interpolate the field value on a point midway between two lattice edges by taking the linear average of fields located at the nearest neighbors. [7]

Using the linear average, we arrive at two possible definitions of the impedance; one is obtained by averaging the magnetic field defined on two adjacent edges of the magnetic lattice, while the other is obtained by averaging the electric field defined

on two adjacent edges of the electric lattice. The two averages lead to two different expressions for the impedance that can be summarized as

$$\eta = \sqrt{\bar{\mu}/\bar{\varepsilon}}(\cos \theta/2)^{S_b} \quad (2.8)$$

. $S_b = 1$ for unit cells that have a predominantly electric response, but $S_b = -1$ for unit cells that have a predominantly magnetic response. The ambiguity in the impedance expression is resolved by a rigorous derivation leading to an exact formula, which will be presented elsewhere. In the limit that the unit cell has a resonant electric or magnetic response, the general expression reduces to Eqs.(2.8).[7]

With the phase advance Eqs.(2.7) and impedance Eqs.(2.8), we can now obtain an analytic solution for the constitutive parameters of metamaterial. Denoting the effective permittivity and permeability as ε_{eff} and μ_{eff} , then the phase shift θ and wave impedance η can be expressed in terms of ε_{eff} and μ_{eff} as: $\theta = \omega p \sqrt{\mu_{\text{eff}} \varepsilon_{\text{eff}}}$ and $\eta = \sqrt{\mu_{\text{eff}}/\varepsilon_{\text{eff}}}$. Considering Eqs. (2.7) and (2.8), we obtain the general solution for the effective permittivity and permeability as[7]

$$\varepsilon_{\text{eff}} = \bar{\varepsilon} \cdot \frac{(\theta/2)}{\sin(\theta/2)} [\cos(\theta/2)]^{-S_b}, \quad (2.9)$$

$$\mu_{\text{eff}} = \bar{\mu} \cdot \frac{(\theta/2)}{\sin(\theta/2)} [\cos(\theta/2)]^{S_b}. \quad (2.10)$$

.
When $0 < \bar{\mu}\bar{\varepsilon} < 4/(\omega p)^2$, θ is real and thus the corresponding modes are propagating. The effective constitutive parameters are predicted by Eqs. (2.9) and (2.10) provide useful insight. The wave impedance approaches zero for an electric resonator, or infinity for a magnetic resonator when $\theta = \pi$ or $-\pi$. This behavior implies that when either $\bar{\varepsilon}$ or $\bar{\mu}$ takes large values, then $\bar{\mu}$ or $\bar{\varepsilon}$ will take accordingly small values. The medium as a whole in these cases can be viewed as a spatial resonator.[7]

When the averaged permittivity and permeability satisfy $\bar{\mu}\bar{\varepsilon} < 0$, only evanescent waves exist in the metamaterial based on Eq. (2.7). In such cases, Eqs. (2.9)

and Eqs.(2.10) represent purely evanescent modes with either electric or magnetic character, depending upon the signs of $\bar{\mu}$ and $\bar{\varepsilon}$. [7]

When $\bar{\mu}\bar{\varepsilon} > 4/(\omega p)^2$, Eq. (2.7) shows that θ will be a complex number $\theta = S_d\pi + i\theta_I$, which corresponds to a resonant crystal bandgap mode. Here, S_d is the dispersion sign defined earlier corresponding to left- or right-handed average parameters, and $\theta_I = 2\ln(u + \sqrt{1+u^2})$. The resonant crystal bandgap results from the periodicity inherent in the metamaterial combined with the large effective constitutive parameters associated with the resonant metamaterial elements. In this case, the effective permittivity and permeability are expressed as [7]

$$\varepsilon_{\text{eff}} = -S_b \cdot \bar{\varepsilon} \cdot \frac{\theta_I - i\pi}{\cosh(\theta_I/2)} [\sinh(\theta_I/2)]^{-S_b}, \quad (2.11)$$

$$\mu_{\text{eff}} = S_b \cdot \bar{\mu} \cdot \frac{\theta_I - i\pi}{\cosh(\theta_I/2)} [\sinh(\theta_I/2)]^{S_b}. \quad (2.12)$$

From Eqs. (2.11) and Eqs.(2.12) we observe three important features. First, only evanescent waves are supported in the crystal bandgap regime. Second, the phase shifts by $\pm 180^\circ$ from one cell to an adjacent cell, where the sign depends on whether the averaged parameters are both positive or negative. Finally, the imaginary parts in the effective permittivity and permeability appear in conjugate forms. Hence one of the constitutive parameters will always acquire a negative imaginary part (i.e., *negative loss* assuming an $\exp(-i\omega t)$ time dependence). The negative loss compensates for the positive loss in the other parameter to generate an overall lossless behavior. [7]

To validate the analytic theory, we consider a metamaterial formed from split ring resonators (SRRs), which possesses a strong magnetic resonance [1]. Since the SRR is a magnetic-response structure, $S_b = -1$ must be chosen. Were we to analyze a structure with an electric resonance, such as the ELC introduced in [46], we would choose $S_b = 1$. From an analytic, quasistatic theory, the SRR structure shown in

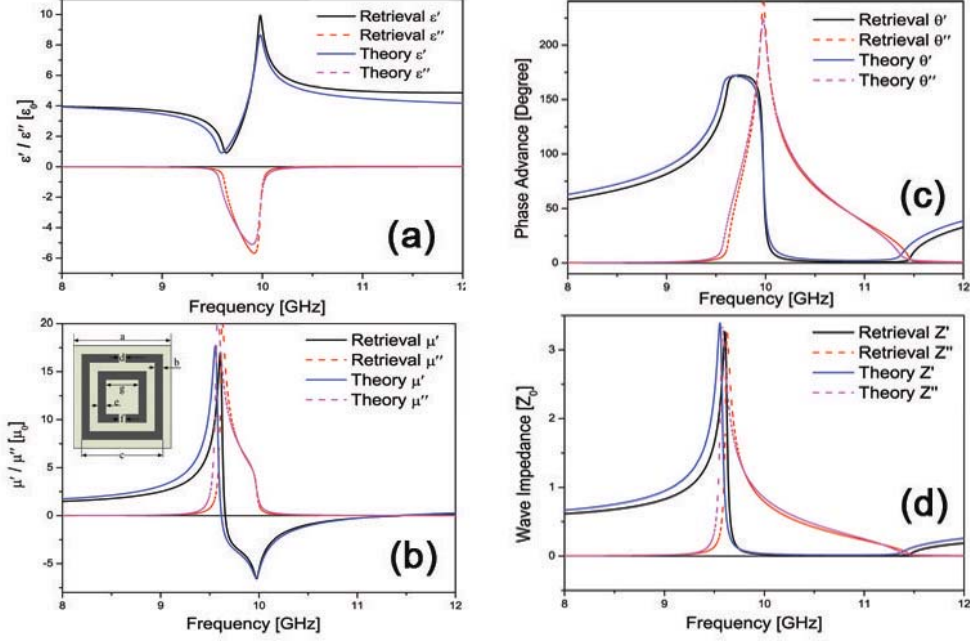


FIGURE 2.2: Comparison of theoretical-prediction results and retrieval results from S parameters for the SRR structure. The parameters used in the theoretical calculation are chosen as $f_0 = 9.975GHz$, $\epsilon_a = 4.4\epsilon_0$, $\mu_a = \mu_0$, $\gamma = 5 \times 10^7$, $p = 2.5$ mm, and $F=0.23$. The SRR structure is inserted in (b). The substrate is FR4 ($\epsilon = 4.4 + 0.044i$) with a thickness of 0.25mm. The dimensions are: $a = 2.5$ mm, $c = 2.2$ mm, $g = 1.1$ mm, $b = e = 0.2$ mm and $d = f = 0.22$ mm. Ref.[7]

Fig. 2.2(a) possesses an averaged permeability in the absence of spatial dispersion of the form

$$\bar{\mu}_{SRR} = \mu_a \left[1 - F f^2 / (f^2 - f_0^2 + i\gamma f) \right], \quad (2.13)$$

in which f_0 is the magnetic resonant frequency, and γ is the loss factor. The SRR usually does not exhibit a strongly dispersive permittivity, so we take for the averaged permittivity $\bar{\epsilon}_{SRR} = \epsilon_a \sin(v)/v$ as a homogeneous model for the background medium, in which $v = \omega p \sqrt{\epsilon_a \mu_a} / 2$. [7]

Based on the ideal form, we calculate the effective permittivity and permeability using the analytic formulas above. Fig. 2.2 compares the predicted parameters for the SRR structure with those from the numerical S-parameter retrieval. The S-parameters are simulated using HFSS (Ansoft), a commercial, full-wave electromag-

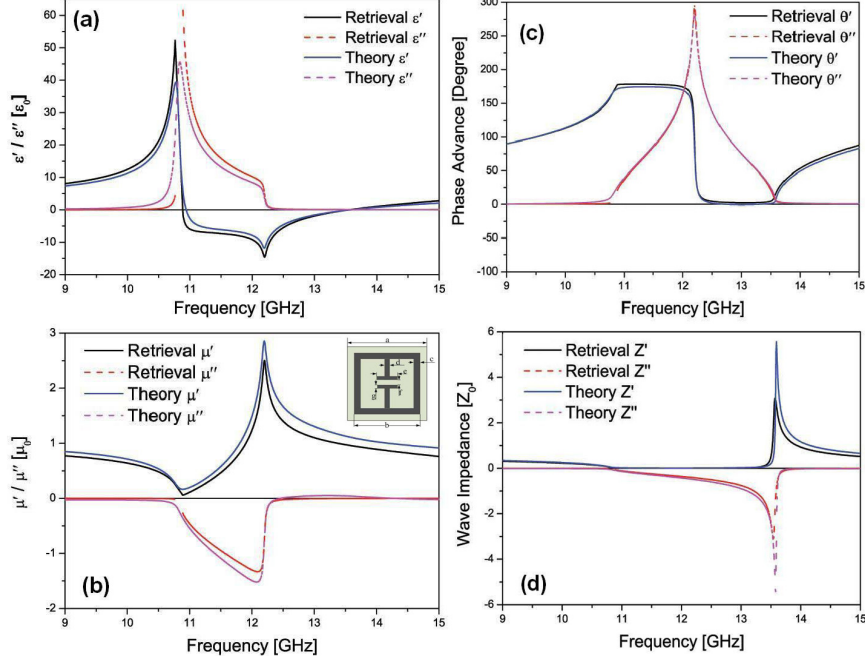


FIGURE 2.3: The ELC Structure. Comparison of the theoretical-prediction results and the retrieval results from the S scattering parameters for the ELC structure. The parameters used in the theoretical calculation are that $f_0 = 12.2GHz$, $\epsilon_a = 4.2\epsilon_0$, $\mu_a = \mu_0$, $\gamma = 4 \cdot 10^7$, $p = 3.333mm$ and $F=0.19$. The substrate is FR4 ($\epsilon = 4.4 + 0.001i$) whose thickness is 0.2026mm. The dimension is that $a=3.333mm$, $b=3mm$, $c=d=g=f=0.2mm$ and $e=1.4mm$. Ref[7]

netic solver whose accuracy has been verified earlier [5, 47, 48]. In the simulations, a single unit cell is simulated along the z direction, with periodic boundaries applied along the x and y directions. From Fig. 2.2, excellent agreement is found between the analytic theory and simulations.[7]

The frequency regimes of various modes can easily be identified from the phase advance shown in Fig. 2.2(c). Below the frequency 9.6 GHz, the wave is propagating. From 9.6 GHz to 10 GHz, the phase advance reaches 180 degrees and hence the wave is in the resonant crystal bandgap region. From 10 GHz to 11.5 GHz, the modes are evanescent. The resonant frequency of SRR occurs at 10 GHz; above 11.5 GHz, all modes again become propagating.[7]

The above analysis provides insight into the behavior of the effective constitutive

parameters for the SRR metamaterial. For example, the large discontinuity in the permeability and corresponding damping of permittivity at 9.6 GHz occurs because $\theta = 180$ at this frequency, which is the transition frequency between propagating modes and resonant crystal modes. The wave impedance becomes very large at this frequency, as shown in Fig. 2.2(d). The critical frequency of the resonant crystal bandgap has previously been misidentified as the resonant frequency of the permeability, which actually occurs at 10 GHz.[7]

Similarly, the other type of particle, the ELC resonator (which can provide electric resonance as shown in Fig. 2.3), can be calculated from the form

$$\bar{\epsilon}_{\text{ELC}} = \epsilon_a \left[1 - F f^2 / (f^2 - f_0^2 + i\gamma f) \right], \quad (2.14)$$

and $\bar{\mu}_{\text{ELC}} = \mu_a \sin(v)/v$. Here, f_0 is the electric resonant frequency.[7]

The relatively analytic formulas presented here provide an accurate description of electromagnetic metamaterials. Because the equations are closed form and relatively simple, the influence of spatial dispersion can be clearly identified and the anomalous form of the constitutive parameters understood. This is a large step toward a full characterization of metamaterials. However, as one can see, this model is only valid for a fundamental electric or magnetic resonant particle. The request on fitting the spatial dispersion curves for a complex unit cell structure (such as a dual resonance with electric and magnetic resonators) requires a general fitting formula.

2.2 A general fitting formula for metamaterials

The last section has introduced the ground step for establishing a relatively analytical model for a fundamental electric or magnetic resonant particle. However, a practical metamaterial design usually requests control of both the electric and magnetic response. In this section, we will propose generalized fitting formulas that can be widely applicable to analyzing complex metamaterial structures.

Going through the process of precise design of the structural response of metamaterials, the standard retrieval procedure through the reflection and transmission is the linchpin by which the effective electromagnetic parameters of a particular physical structure can be extracted [3]. However, such a standard retrieval procedure is an approach to measurement by which, people have to either conduct an experiment or run full wave numerical simulations for the specific metamaterial unit cell. Both of these approaches to obtain reflection and transmission data consume a large amount of time. Thus, the need to develop an advanced rapid metamaterial design system becomes essential to the field. However, the lack of an advanced design system for metamaterials is mostly due to the complexity of a non-infinitesimal structural system, in which enormous spatial dispersion and wave impedance are involved. The sophisticated design of metamaterials requires accuracy on both permittivity and permeability over the entire frequency range of interest. Unfortunately, no general fitting formulas are currently available due to the gap between the practical structure and the theoretical modelling. The most recent progress in effective medium theory [7] proposed more precise descriptions of periodic-based structural metamaterials, where the spatial dispersion has been appropriately considered. The descriptions of metamaterials in Ref[7] has modeled the fundamental magnetic or electric resonators very well by separating the particle response and the system behavior, and has illustrated accurate fitting to some simple practical structures.

However, as the complexity of the structure increases, the analysis in Ref[7] is insufficient to fit the performance of a complex medium such as SRR-ELC combination structures [49] or a structure (like SRR) that contains different resonances at different frequencies. Moreover, metamaterials have the potential to implement transformation optics [25, 26], in which special anisotropic properties are required. Therefore, the demand for accurate prediction of metamaterial structures requires a general fitting model for complex resonant particles. In this section, we will pro-

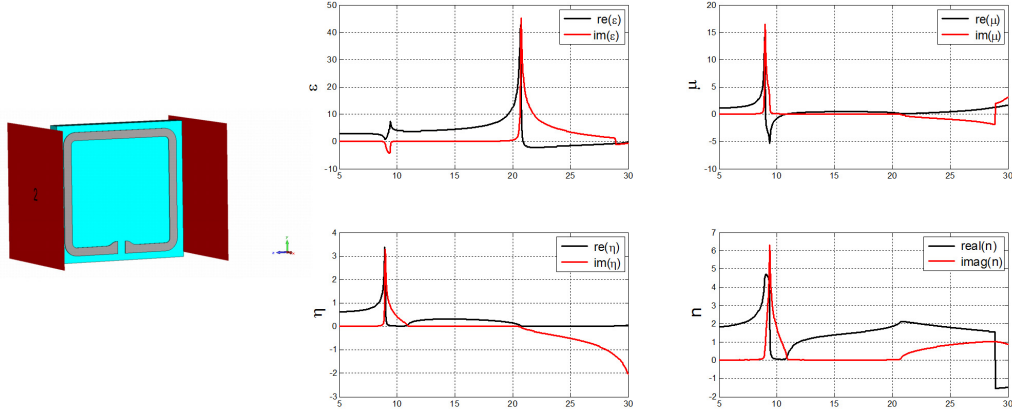


FIGURE 2.4: A full wave simulation on [simulation of an] an SRR structure and the extracted permittivity and permeability from 5 GHz to 30GHz

pose a formula transformation that can turn a complex response curve into a simpler Drude-Lorentz-like resonance, and then we propose an analytical formula that can fit the response of a complex metamaterial structure.

To illustrate the practical metamaterial structure's response, we selected an SRR structure and conducted the standard retrieval shown in Fig.2.4, in which a fundamental magnetic resonance is observed at 9GHz and a higher electric resonance occurs at about 20GHz. We can see that both the magnetic and electric resonance affects the structure's response in the frequency range of interest. However, according to the field averaging theorem, we cannot fit and model both resonances by the same simple analytical formula. Thus there is an increase in the difficulty of the structure's design. To resolve this difficulty, we re-derived the field averaging formulas (Appendix A) and achieved the new set of fitting formulas given below,

$$\sin(\theta/2) = S_d \omega p \sqrt{\mu_1 \varepsilon_1} \sqrt{AF} / 2$$

$$\eta = \frac{E}{H} = \sqrt{\frac{A}{F}} \cdot \sqrt{\frac{\mu_1}{\varepsilon_1}} \quad (2.15)$$

in which $S_d = 1$ or -1 , depending on the restriction of the positive imaginary part of θ . A and F , are spatial dispersion factors according to Appendix A,

$$F = \frac{\bar{\mu}H}{\bar{\mu}_1 H_1} = \frac{B}{B_1}, A = \frac{\bar{\epsilon}E}{\bar{\epsilon}_1 E_1} = \frac{D}{D_1} \quad (2.16)$$

A and F are usually unknown because of the lack of sufficient field distribution information in the field averaging approach. However, we can group A and F with $\bar{\epsilon}_1$ and $\bar{\mu}_1$ to generate an arbitrary average parameters *overline* ϵ_m and $\bar{\mu}_m$ such that,

$$\begin{aligned} \sin(\theta/2) &= S_d \omega p \sqrt{\bar{\mu}_1 \bar{\epsilon}_1} \sqrt{AF}/2 \\ &= S_d \omega p \sqrt{\bar{\mu}_m \bar{\epsilon}_m} \cos(\theta/2)/2 \\ \eta = \frac{E}{H} &= \sqrt{\frac{A}{F}} \cdot \sqrt{\frac{\bar{\mu}_1}{\bar{\epsilon}_1}} = \sqrt{\frac{\bar{\mu}_m}{\bar{\epsilon}_m}} \end{aligned} \quad (2.17)$$

Although the $\bar{\epsilon}_m$ and $\bar{\mu}_m$ no longer represent any sensitive physical parameters, they can remain in Drude-Lorentz form from $\bar{\epsilon}_1$ and $\bar{\mu}_1$ mathematically, and can be used as generalized fitting parameters. The intuition to make such a transformation is discussed in Appendix A. Therefore, we can achieve the general fitting formulas that

$$\begin{aligned} \epsilon_{eff} &= \frac{\theta/2}{\tan(\theta/2)} \bar{\epsilon}_m \\ \mu_{eff} &= \frac{\theta/2}{\tan(\theta/2)} \bar{\mu}_m \end{aligned} \quad (2.18)$$

in which

$$\begin{aligned} \bar{\epsilon}_m &= \epsilon_a \left(1 - \sum_i \frac{F_{ei} f^2}{f^2 - f_{ei}^2 + i\gamma_{ei} f} \right) \\ \bar{\mu}_m &= \mu_a \left(1 - \sum_i \frac{F_{ui} f^2}{f^2 - f_{ui}^2 + i\gamma_{ui} f} \right) \end{aligned} \quad (2.19)$$

or we can remove the spatial dispersion by taking the inverse formulas

$$\begin{aligned}\bar{\epsilon}_m &= \frac{\tan(\theta/2)}{\theta/2} \epsilon_{eff} \\ \bar{\mu}_m &= \frac{\tan(\theta/2)}{\theta/2} \mu_{eff}\end{aligned}\tag{2.20}$$

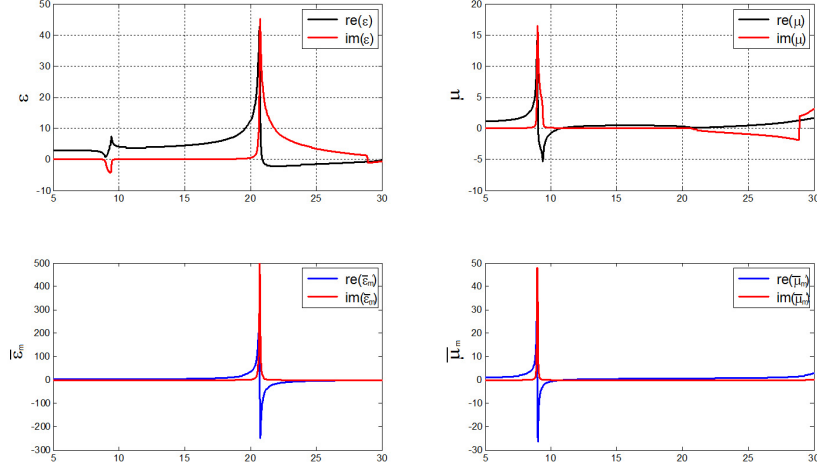


FIGURE 2.5: A numerical particle retrieval on an SRR structure. The spatial dispersion effect can be removed by using the generalized formula

To illustrate the use of the generalized fitting formula, we can apply Eq.2.20 to remove the spatial dispersion effect on the simulated structure in Fig. 2.4, in which the blue curve is the extracted $\bar{\epsilon}_m$ and $\bar{\mu}_m$. Both the magnetic and the electric resonance can be reduced to a simple Drude-Lorentz resonance-like curve. The reduced curve can then be easily fitted by Eq.2.19. Therefore, we can fit the structure's response over the entire frequency range from 5GHz to 30GHz. To further validate and demonstrate the general fitting formulas derived here, we examined the recent [omit "recent"] structure of a SRR-ELC NIM particle [49] and also generated a more complicated combination structure based on the SRR-ELC NIM particle.

In the fitting process, we only took the fundamental electric and magnetic resonance, that is, only one electric resonant frequency and one magnetic resonant

frequency exist in Eq.2.19. Fig. 2.6 indicates the excellent matching of the theoretical curves and the HFSS simulated results achieved by setting $f_e = 10.205\text{GHz}$, $f_u = 10.703\text{GHz}$, $F_e = 0.2445$, $F_u = 0.2688$, $\gamma_e = 0.02\text{GHz}$, $\gamma_u = 0.0245\text{GHz}$. Notice that the physics behind the SRR-ELC structure is rather complex and might include magnetoelectric coupling.[8] Here we have only focused on the confined polarization situation. This structure will be discussed further in the next section.

To verify the generality of Eq.(2.19)-(2.20), we consider an example of another complex structure composed of four different resonant particles in one cell, as shown in Figure 2.7(a). The coupling between each unit cell and the spatial dispersion for different frequency ranges make the effective permittivity and permeability "disordered", as depicted in Figure 2.7(c) and (d). Nevertheless, applying particle retrieval to the complex medium proposed by Eq.(2.20), the multiple electric and magnetic responses are clearly separated into ϵ_m and μ_m , yielding the Drude-Lorentz form. Estimating the parameters in Eq.(2.19), the overall frequency responses can be surprisingly backed up; the fitting will not be repeated redundantly here.

Therefore, we propose a general fitting formula inspired by the effective medium theory described in Ref.[7] (Appendix A). We tested the algorithm on different types of structures, and the simulated results revealed the generality of the proposed procedure. The algorithm will greatly benefit the design and understanding of metamaterials and other types of dispersive materials, and can be extended to optical metamaterials or plasmonic structures.

2.3 A thin slab model and numerical analysis

In this chapter, we have introduced the effective medium theory based on the field average approach. The entire theory is based on Maxwell's Equations in a periodic lattice environment. We defined the average parameters by taking the surface and line integration of the field in the Bloch wave propagation. However, the Bloch

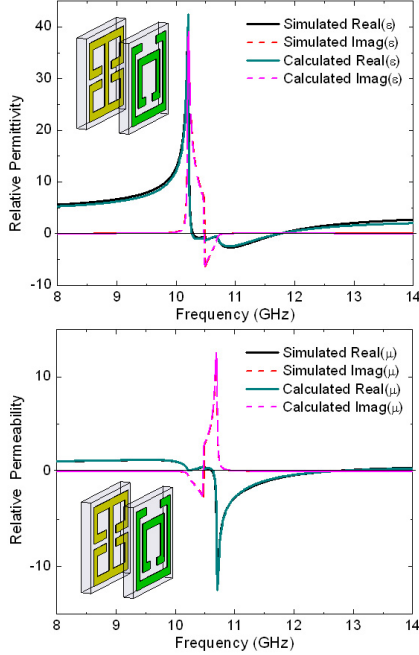


FIGURE 2.6: Fitting the response of the SRR-ELC NIM particle structure. Ref.[4]

wave propagation only gives us the Bloch wave mode information (a constant phase advance per unit cell) but no detailed field distribution. The lack of sufficient information in the model results in the introduction of parameters such as A and F in the fitting formulas, or the assumption of the field interpolation in Section 2.1 to solve the Bloch impedance and wave vector. The advantage of the field averaging approach is that we can know the minimum information that can determine the spatial dispersion behavior of any given metamaterial unit cell. However, the framework of the field averaging approach we introduced cannot provide more field sampling information within one unit cell[5, 7]. To address this difficulty, a series of assumptions [assumptions about the] on the field distribution in the Bloch wave were made to calculate the field properties every half-periodicity. The sensitive spatial dispersion curves have been demonstrated, compared to the numerical retrieval[7]. This demonstrates the practical utility of the theory, to analyze and fit the metamaterial's complex response. However, a rigorous justification cannot be simply made

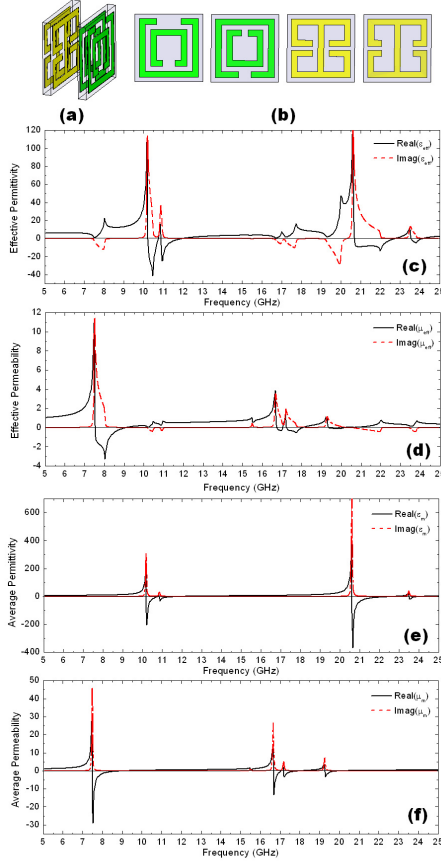


FIGURE 2.7: Particle retrieval to a 4-cell combination structure. (a) 4-cell-combination structure, and (b) 4 cells in the combination structure. The combination structure is generated from a SRR-ELC NIM particle (Ref[4]) by shortening the ELC's arm and shrinking the SRR's gap in half and attaching it to the other side of the substrate, (c)-(d) the effective permittivity and permeability by numerical simulation (e)-(f) particle retrieval for ϵ_m and μ_m

for all these field assumptions. In addition, the metamaterial structure is of such complexity that no analytical solution can be provided. It is difficult to justify the assumptions by solving the full unit cell structure in a closed form.

To address this difficulty, we introduced a thin slab model with a specific physical structure and the numerical analysis of the practical metamaterial structure. The idea of the thin slab model is to confine the dipole moment in an extremely thin slab to represent the practical metamaterial's structure; thus an analytical solution can be achieved. The numerical analysis is to extract field distribution in the full wave

simulations to demonstrate the coherence between the effective medium model and a practical situation. We expect that the thin slab model and numerical analysis can support the field averaging approach by providing detailed field distribution information.

To establish the thin slab model, Fig. 2.8 illustrates the configuration of the thin slab model, in which the slab is periodically aligned along the propagation direction. The thickness of each slab is l and the distance of the air space between two adjacent slabs is d . The permittivity and permeability are ϵ_s and μ_s . The thin sheet represents the dipole moment of a metamaterial structure and confines them periodically. Applying a quasi-static analysis to the thin slab model, the average permittivity and permeability can be expressed as

$$\begin{aligned}\bar{\epsilon} &= (d\epsilon_0 + l\epsilon_s)/p \\ \bar{\mu} &= (d\mu_0 + l\mu_s)/p\end{aligned}\tag{2.21}$$

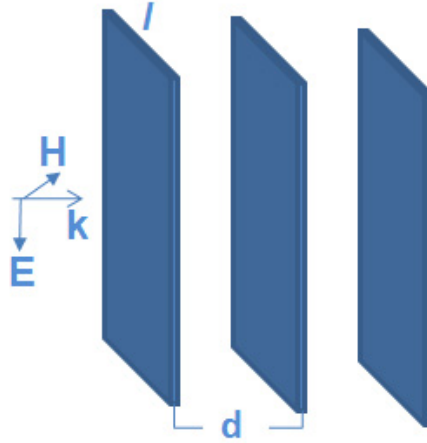


FIGURE 2.8: The configuration of the thin slab model

For the magnetic resonance, we can further apply the Drude-Lorentz model to the $\bar{\mu}$ and a constant $\bar{\epsilon}$. In the model calculation, the ϵ_s and μ_s can therefore be

determined by setting l and p .

To solve the model, we introduced the transformation matrix in the propagation direction in Eq.(2.22), in which E' and H'_{red} are one periodicity forward to the E and H_{red} , and $H_{red} = i\omega\mu_0 H$ [50].

$$\begin{pmatrix} E' \\ H'_{red} \end{pmatrix} = \overline{\overline{T}} \begin{pmatrix} E \\ H_{red} \end{pmatrix} \quad (2.22)$$

We start from the center of the air space, the first T matrix is the wave propagation in the $d/2$ air, and thus

$$\overline{\overline{T}}_{air} = \begin{pmatrix} \cos(k_0 d/2) & -\sin(k_0 d/2)/k_0 \\ k_0 \sin(k_0 d/2) & \cos(k_0 d/2) \end{pmatrix} \quad (2.23)$$

, in which $k_0 = \omega\sqrt{\epsilon_0\mu_0}$. Then the wave will propagate in the thin slab and the T matrix can be written as

$$\overline{\overline{T}}_{slab} = \begin{pmatrix} \cos(k_s l) & -(z_{sr}/k_s) \sin(k_s l) \\ (k_s/z_{sr}) \sin(k_s l) & \cos(k_s l) \end{pmatrix} \quad (2.24)$$

, in which $k_s = \omega\sqrt{\epsilon_s\mu_s}$ and $z_{sr} = \sqrt{\mu_s/\epsilon_s}/\sqrt{\mu_0/\epsilon_0}$. The third part of the propagation will be another $d/2$ air and has the same T matrix as $\overline{\overline{T}}_{air}$. The total $\overline{\overline{T}}_{total}$ can be calculated through

$$\overline{\overline{T}}_{total} = \overline{\overline{T}}_{air} \overline{\overline{T}}_{slab} \overline{\overline{T}}_{air} \quad (2.25)$$

Now we assume that we locate the thin slab in the center of the unit cell as in Fig. 2.4. The thin slab location is from $z = p/2 - l/2 + Np$ to $z = p/2 + l/2 + Np$, in which $N = 1, 2, 3 \dots$. Through the T matrix calculation, we can obtain the Bloch wave vector (or phase advance θ), the Bloch wave impedance, and the detailed $E_x(z)$ and $H_y(z)$ field distribution in the thin slab model. The phase advance and Bloch

wave impedance can be calculated by

$$\cos(\theta) = (\bar{\bar{T}}_{total11} + \bar{\bar{T}}_{total22})/2$$

$$\eta = i\omega\mu_0\sqrt{\bar{\bar{T}}_{total12}/\bar{\bar{T}}_{total21}} \quad (2.26)$$

. Therefore, we can make use of the thin slab model to calculate the same metamaterial properties that we have calculated using the field averaging technique. Moreover, the advantage is that a detailed field distribution also can be provided by the specific physical model.

For example, we can calculate a magnetic resonant structure by setting the Drude-Lorentz model to the $\bar{\mu}$ and $l = p/100$. Fig. 2.9 provides a comparison of the field averaging model proposed in the PRE paper[7] and the thin slab model. From Fig.

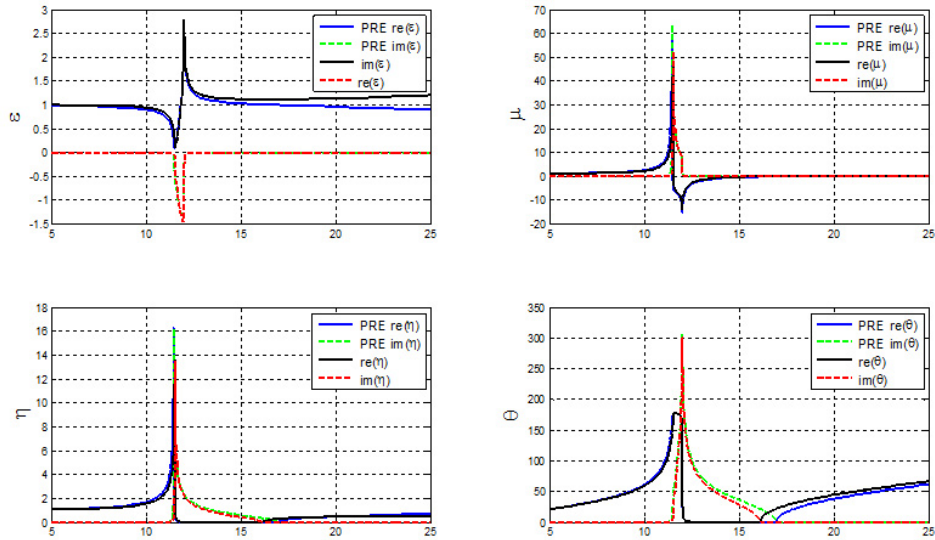


FIGURE 2.9: Calculation of metamaterial parameters by using both the thin slab model and the field averaging approach

2.9 we can see that the trend and basic features of the two models agree well with each other. Whereas there is a slight discrepancy between them, especially at higher

frequencies, this is because in the field average approach, we only consider the fundamental resonance. Yet in the thin slab model, the photonic crystal setup automatically introduces the [introduces a] higher order mode resonance and will contribute to the dispersion and the impedance in the frequency range of interest to us. Once we reduce $\sin(k_s l) = k_s l$, $\sin(k_0 d/2) = k_0 d/2$ and $\cos(k_0 d/2) = 1 - (k_0 d/2)^2$, we can find mathematically that the thin slab model is reduced to the field averaging approach Eq.2.7 and Eq.2.8. However, to be precise, we would not mathematically reduce the solution but compare the two models and their assumptions to the numerical analysis.

To make further use of the thin slab physical model, we calculated the field distribution at 10.5 GHz in this particular example. Fig. 2.10 shows the electric and magnetic field distribution in the thin slab model. To make the comparison, we also illustrate the field distribution based on the assumption in the field average approach in Fig. 2.11. However, we can see the discrepancy between the thin slab model and the field assumption in the field averaging approach, although the spatial dispersion and the wave impedance appear to be very similar. The assumption of a uniform phase of the magnetic field within a strong resonant unit cell does not appear in the calculation of the thin slab model. Such a discrepancy will definitely lead to a different value for the impedance calculation. We calculated the impedance at this particular frequency and found that the relative impedance by the thin slab model is $1.8221 + 0.0051i$, and that by the PRE method is $1.9808 + 0.0057i$. They are different, but close to each other. We understand that the higher order mode affects the calculation in the thin slab model. The basic features of the field distribution in magnitude, however, match well between the two models. To further evaluate the assumption and the thin slab model, we first created an SRR structure as shown in Fig. 2.12, and performed a numerical analysis based on the particular magnetic structure under the standard retrieval environment, because the numerical extracted

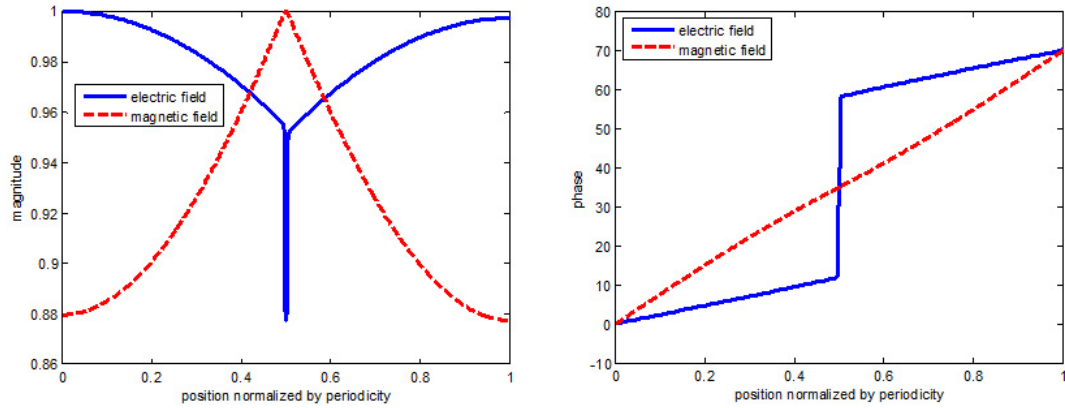


FIGURE 2.10: Field distribution in the thin slab model

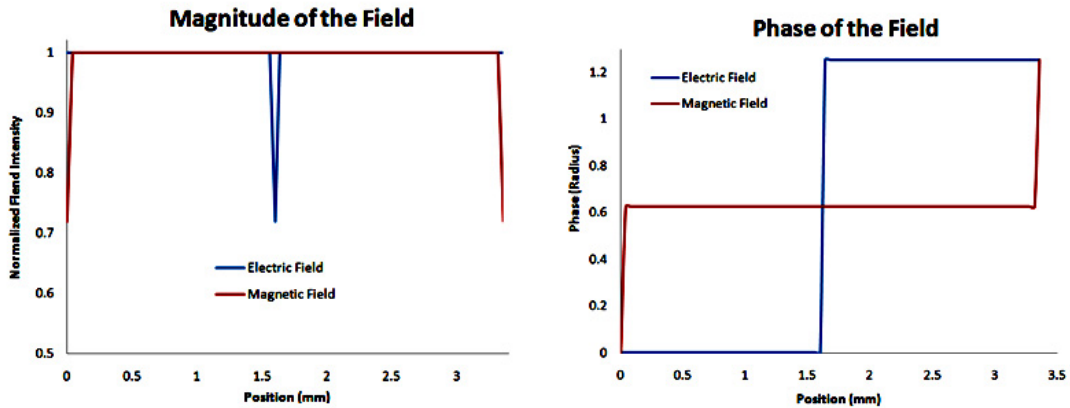


FIGURE 2.11: Field distribution by the field averaging assumption

permittivity and permeability are calculated from this model. We observed the field distribution at the maximum transmission frequency to avoid the standing wave issue in Fig. 2.13. We notice that in the practical 3D structure, the field is highly complex and localized. The point of our observation is to select the place where the field's intensity is strong and can dominate the main feature (or the largest contribution to the integration). In this model, we select the x-z plane at the bottom to observe E_y because the resonance at the gap of the ring causes an extremely strong local electric field, and the y-z plane near the structure causes the magnetic resonance of the current loop to generate a strong local magnetic field. From the field distribution

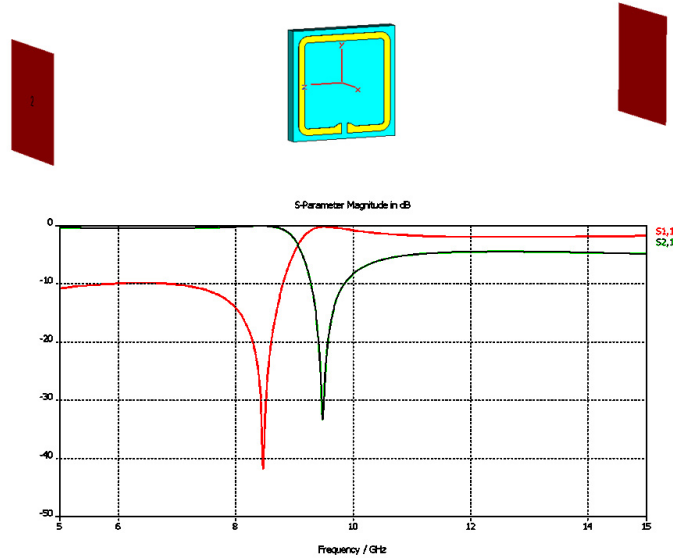


FIGURE 2.12: A practical SRR structure model created with the full wave simulation software. The numerical solution on the S-parameter is shown. The maximum transmission frequency is 8.5GHz

appearing in Fig.2.14, we can see the step function is in phase with the magnetic field and electric field that partially represents the assumption in the field averaging approach. We also extracted the field distribution, shown in Fig. 2.15. We can see that the local field in the practical structure is highly inhomogeneous. The phase is similar to the assumption in field averaging approach but the magnitude differs from both of the models. Therefore, we should say that any simplified physical or lattice model of the metamaterial structure is the ideal case of the dipole moment. The reality is much more complicated than any of those models, and can only be solved numerically. However, it is still worth having a theoretical model to describe the underlying physics and to approximate the unit cell's response. We should also note that to make a complete comparison with the theoretical model, we should calculate an Eigen-mode numerical solution and average the field everywhere inside the unit cell, so that the calculated structure is in an infinite array environment, which will

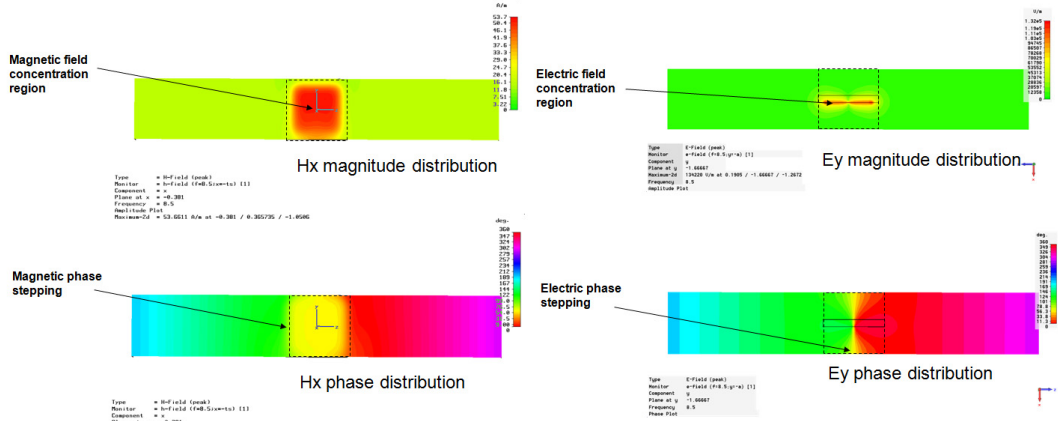


FIGURE 2.13: Numerical observation of the field distribution on an SRR structure

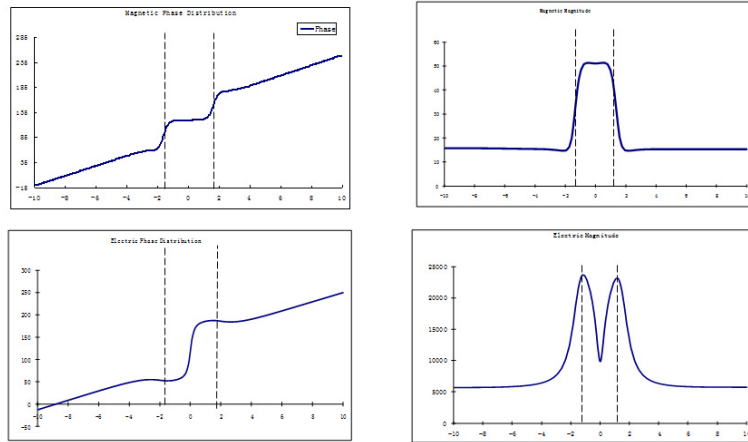


FIGURE 2.14: Electric and magnetic field distribution extracted from the full wave simulation

be discussed below.

Now we are going to examine another assumption which is made in the field averaging approach. We assumed before that the electric field and magnetic field, if plotted on a polar graph, would be multiple line segments rather than a circular curve because of the spatial dispersion. The field in the center of the line segment will then be the linear average of the field at the end points of the segment, as interpreted in Section 2.1. As we can extract the field distribution from the thin slab model and the numerical analysis, we can create the polar plots and compare them to the assumption. Fig. 2.15 shows the polar plots of the fields calculated by

the thin slab model and the assumption in the field averaging approach. To make

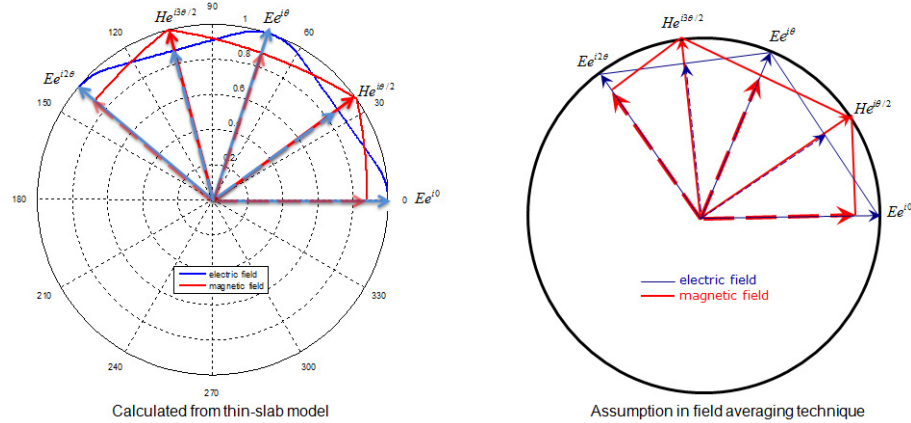


FIGURE 2.15: Comparison of the polar field plot between the thin slab model and the assumption

an equivalent study, we conducted an Eigen-mode numerical solution on an infinite SRR array, as shown in Fig. 2.16. This figure also shows the polar plots of the fields in the full wave simulations. Surprisingly, we found that the three solutions are very well matched. They have the identical feature on wave propagation, demonstrated in those polar plots. Therefore, although the detailed field distribution along the propagation direction differs greatly in the three solutions, the polar fields are very similar to each other and can further explain the assumption of linear interpolation in the field averaging approach. Correspondingly, the impedance will vary periodically along the propagation direction. Fig. 2.16 demonstrates the spatial wave impedance by calculating the impedance in the thin slab model.

To compare Fig. 2.10, Fig. 2.11 and Fig. 2.16, we plotted the field distribution in a unit cell in Fig. 2.18. We find that the Eigen-mode numerical solution occupies a middle status between the thin slab model and the field assumption. To discover this phenomenon, we found a physical model that reflects the field distribution feature in the field averaging assumption in Fig. 2.19. The 2D SRR structure demonstrates well the extreme case of the field assumption if the structures are very close to

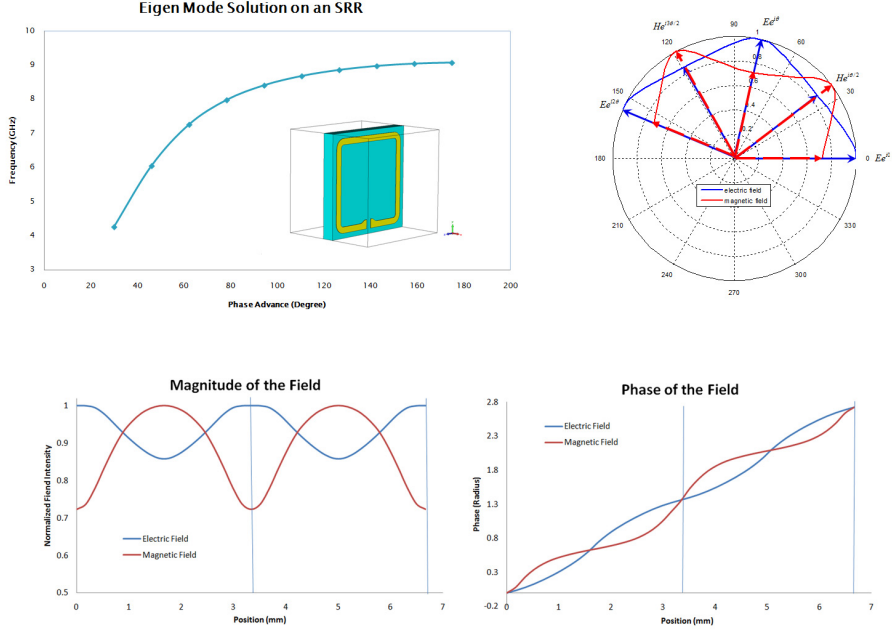


FIGURE 2.16: Numerical Eigen-mode solution of the SRR and the electric and magnetic field distribution

each other. Therefore, we can conclude that the thin slab model serves to restrict the dipole moment in a sheet; the field assumption distributes the dipole moment uniformly within the entire unit cell, while the 3D SRR structure is in-between these two extreme cases.

Now we will further justify the derivation and approximation in Section 2.2 by the thin slab model and numerical analysis. Referring to Eq.2.17, the spatial dispersion and impedance is dominated by the average parameters and the A and F factors. For the magnetic metamaterial, we made an assumption about A and F based on the uniform phase distribution assumption and thus showed that $A = 1/\cos(\theta/2)$ and $F = \cos(\theta/2)$. Using this assumption, we found that $\bar{\epsilon}_1 = \bar{\epsilon}$ and $\bar{\mu}_1 = \bar{\mu}$ because $AF = 1$, and $\eta = \sqrt{\bar{\mu}_1/\bar{\epsilon}_1}/\cos(\theta/2)$ because $\sqrt{A/F} = 1/\cos(\theta/2)$. Such an assumption is verified by the full wave simulation in Fig.2.13, in which the uniform phase distribution indicates the possible A and F values to be close to the assumption.

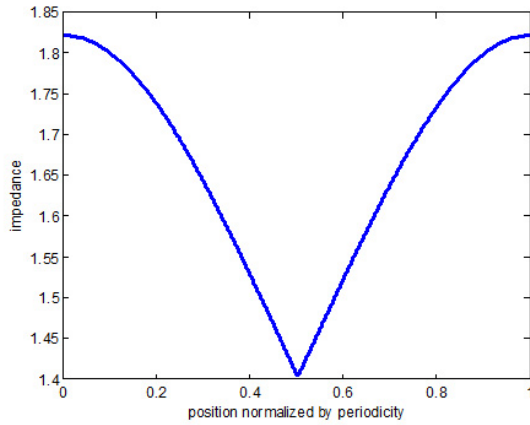


FIGURE 2.17: The wave impedance along the propagation direction calculated by the thin slab model

We then again used the thin slab model to illustrate the A and F values by taking the field integration. To justify the A and F values by the thin slab model and the assumption, we made a numerical comparison for the particular model in Fig.2.20, in which we can see that A and F values are close, with only a slight difference between the thin slab model and the $\cos(\theta/2)$ assumption. This difference explains the slight quantity discrepancy between the two approaches. .

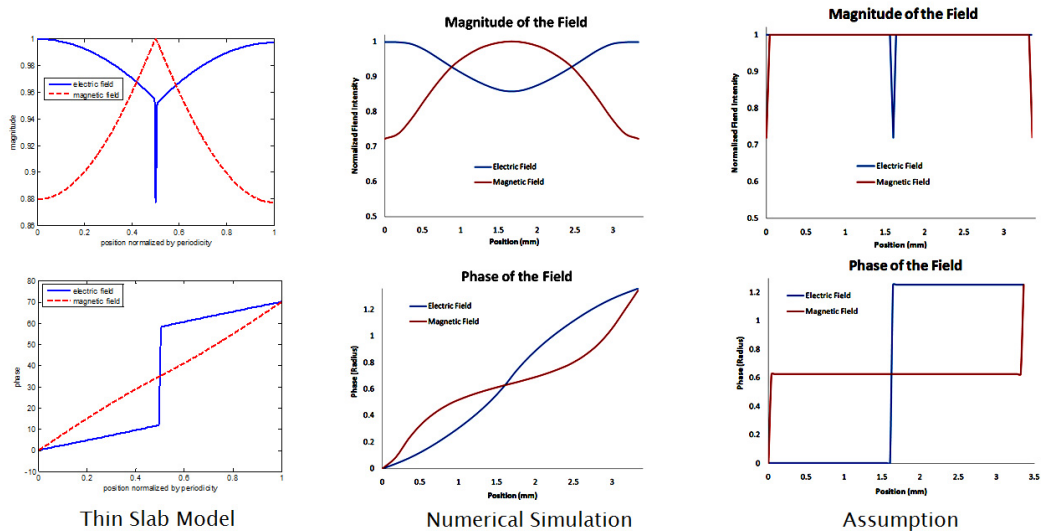


FIGURE 2.18: The field distribution within a unit cell by the thin slab model, the Eigenmode solution on 3D SRR, and the field assumption

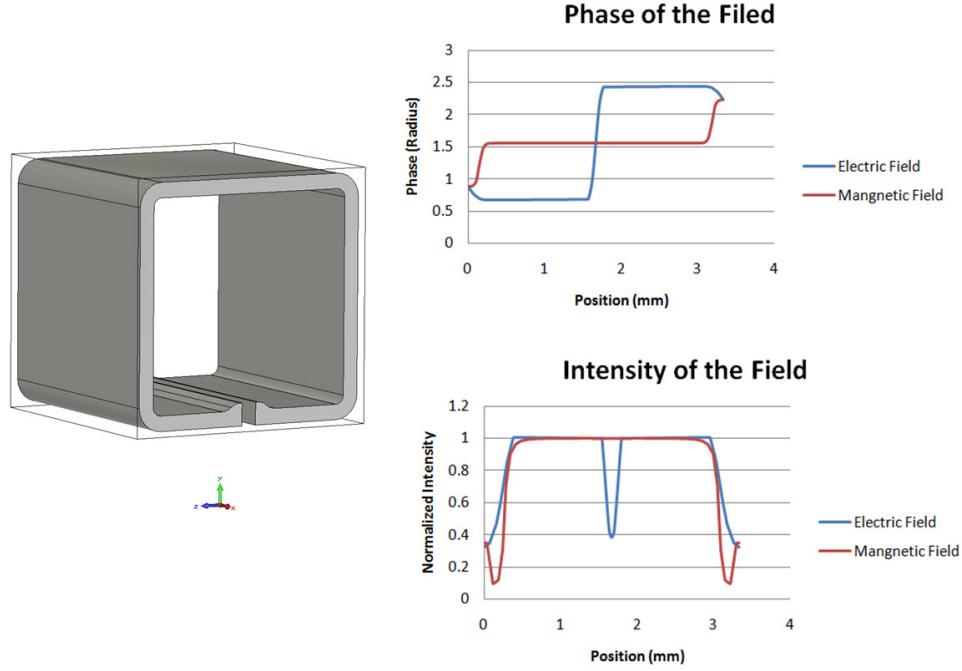


FIGURE 2.19: Eigen-mode solution on a nearly 2D SRR structure. Notice that the wave is propagating along the z-axis. To get a continuous field, we leave a tiny gap on the x-axis and observe the field distribution in that gap.

To further demonstrate the coherence and distinction of the field averaging approach and the thin slab model, we can calculate the impedance again by using the T matrix, the method in Eq.2.17, by applying the A and F values extracted in the field distribution calculation, and the method in the PRE paper, or by applying $A = 1/\cos(\theta/2)$ and $F = \cos(\theta/2)$. We can see from Fig. 2.20 that the three calculations are close to each other. The first two methods are more coherent because of

	Assumption	Thin Slab Model
A	1.2206+0.0011i	1.1382 + 0.0010i
F	0.8193 - 0.0008i	0.8729 - 0.0008i
AF	1.0000	0.9935
A/F	1.4898 + 0.0028i	1.3039 + 0.0023i

FIGURE 2.20: We compared the A and F values by using the thin slab model and the assumption in Section 2.2

T matrix method	1.8221 + 0.0051i
Eq.2.22 by using extracted A and F values in thin slab model	1.8530 + 0.0053i
PRE method	1.9808 + 0.0057i

FIGURE 2.21: We compare the impedance calculated by three different methods

the use of extracted A and F values from the field distributions. This agreement also supports the derivation of Eq.2.17. The overall agreement among the three methods indicates that the thin slab model vindicates the assumption from the field averaging approach.

We further studied the reason for the difference between the first two methods of calculation. The discrepancy can be attributed to the different definitions of the average parameters $\bar{\epsilon}$ and $\bar{\mu}$, which is not justified as well in the field averaging approach. The average parameters in the thin slab model are demonstrated in Eq. 2.21. However, in the propagating waves, the average parameters are defined from Maxwell's Equations in Eq. 2.4 and Eq. 2.6. The field averaging approach does not justify the equivalence of these two definitions but explains that the average permittivity and permeability should be dominated by the local medium properties at very subwavelength scale intuitively. To justify this aspect, we recall the average parameters from Eq. 2.21 are $\bar{\epsilon}_{thin\ slab}$ and $\bar{\mu}_{thin\ slab}$ and use the notation in Section 2.2 on the average parameters defined by field integration. We then compared numerically those average parameters by the different definitions, as shown in Fig. 2.22. From

Calculation of Local Average Parameters			
$\bar{\epsilon}_{thin\ slab}$	1	$\bar{\mu}_{thin\ slab}$	2.6333 + 0.0102i
$\bar{\epsilon}_1$	0.9767 - 0.0000i	$\bar{\mu}_1$	2.5190 + 0.0096i
$\bar{\epsilon}$	0.9766 - 0.0000i	$\bar{\mu}$	2.5027 + 0.0095i

FIGURE 2.22: We compared the average parameters

this calculation, the thin slab model justified the coherence of different definitions on the average parameters. The agreement between $\bar{\epsilon}_1$ and $\bar{\epsilon}$, $\bar{\mu}_1$ and $\bar{\mu}$ is due to the

result of $AF = 1$. The slight difference between $\bar{\epsilon}_1, \bar{\mu}_1$ and $\bar{\epsilon}_{thin\text{slab}}, \bar{\mu}_{thin\text{slab}}$ results in the tiny difference of the impedance calculation in Fig. 2.20 (the first two methods). Therefore, the thin slab model tells us that one can separate the metamaterial response into systematic behavior that is described by discrete Maxwell's Equations, and the local particle response that is calculated by the quasi-static field analysis. However, we should recall again that both of the models have simplified the practical metamaterial structure, and thus can only approximate the unit cell behavior to a certain extent.

Finally we made more full wave simulations to demonstrate the features of the wave propagation in the practical metamaterial structures. In Fig. 2.23, we simulated the same SRR structure with 6 unit cells along the propagation direction to form a finite SRR slab. The electric and magnetic field distribution is illustrated in Fig. 2.24. From this calculation, we can observe that the wave propagation is largely

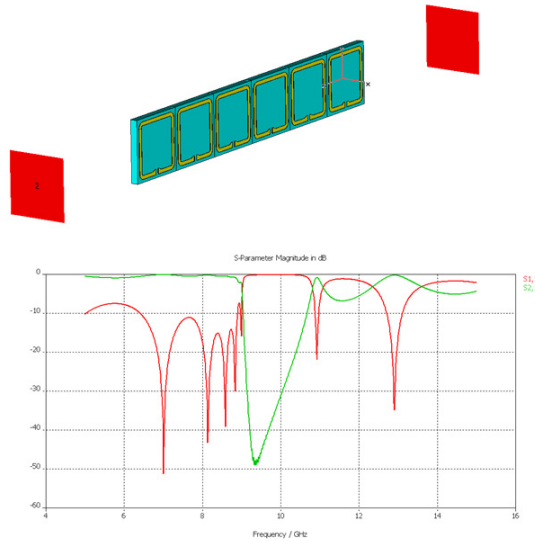


FIGURE 2.23: A full wave simulation on the six SRR slab

affected by the local resonant fields that jump per periodicity. We further extracted the field distribution and plotted the field in Fig. 2.25. The practical case is more

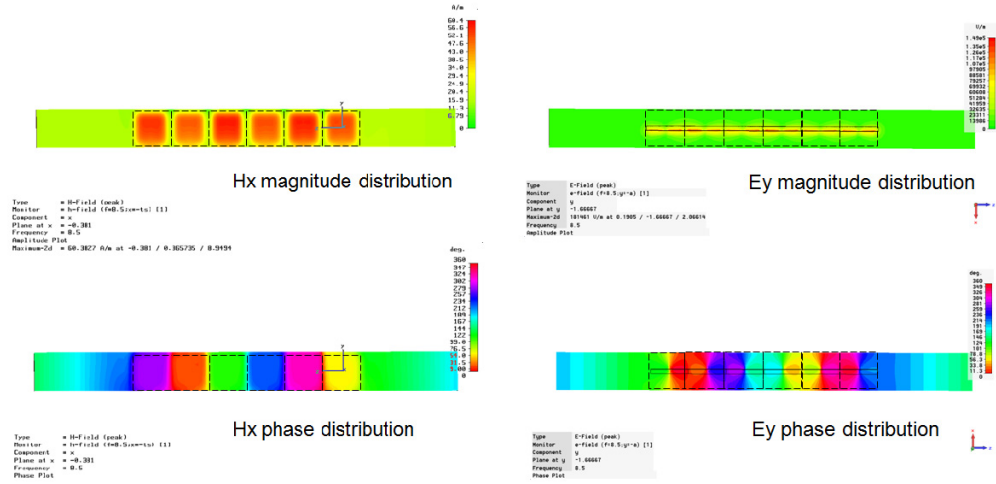


FIGURE 2.24: The electric and magnetic field distribution solved by full wave simulation software

complicated than the field average model and the thin slab model. Nevertheless, the basic feature of the jumping field is illustrated. We further simulated the electric metamaterial (ELC structure) in Fig. 2.26. The field distribution is demonstrated in Fig. 2.27. We can justify the assumption in the field averaging approach for the other case. The different observation point of the impedance resulted in the different

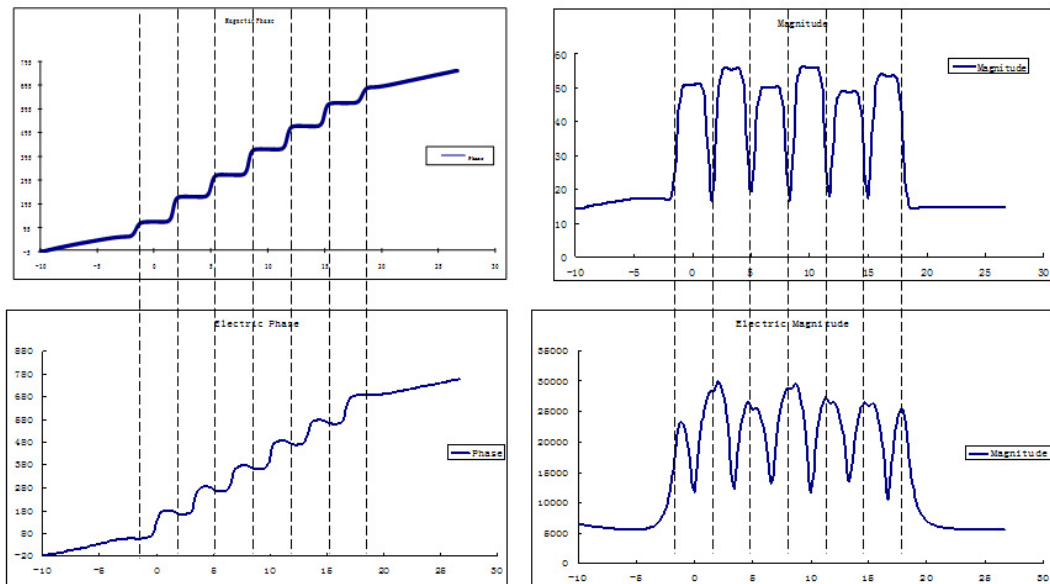


FIGURE 2.25: Field plot along the propagation direction

calculation of the field interpolation, compared to the the magnetic resonance case.

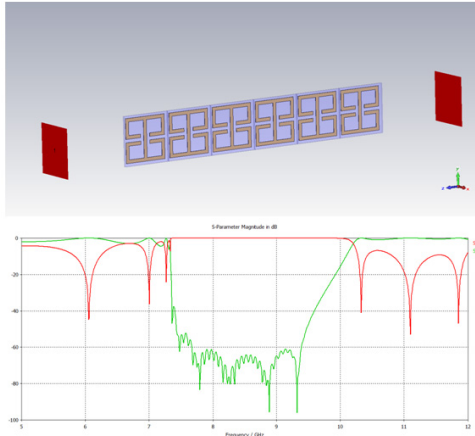


FIGURE 2.26: A full wave simulation on the six ELC slab

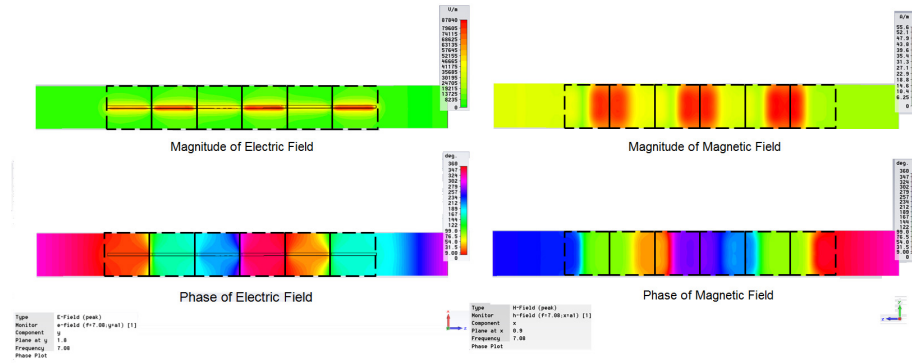


FIGURE 2.27: The electric and magnetic field distribution solved by full wave simulation software

To summarize the analysis in this section, we introduced the thin slab model in order to obtain more detailed field distribution information. With the physical model solution, we justified the assumption made in the field averaging approach and the derivation of the discrete Maxwell’s Equations. To evaluate both of the models, we conducted a full wave simulation on the practical metamaterial structures and found that both models can approximate the basic feature of the wave propagation inside metamaterials in general. However, the field distribution in a practical structure is much more complicated than any of the models we created. The thin slab model

and the field averaging approach (with the assumptions) can only approximate and explain some of the physics of the real structures. Thus, the study shows that the implementation of the metamaterial is only an approximation of the ideal dipole moment response from intuition, and is only a crude approximation in the characterization. All these approximations are made to permit people to simply design complex scattering systems. Therefore, the analysis of the metamaterials is more methodological than for facilitating the discovery of new natural materials.

2.4 Negative-index material composed of electric and magnetic resonators

In Section 2.2, we proposed a general fitting formula that can treat complex metamaterial unit cell design, including dual resonators combining SRR and ELC. Although the complex curve can be arbitrarily fitted, we notice that the physical origin can be even more complicated due to the magnetoelectric coupling.[8] However, if we can arrange these two types of resonators away from each other (for example, alternatively arranged), magnetoelectric coupling might be reduced, and such media can form negative index materials, at least in one dimension. Fig. 2.5 illustrates the unit cell response and the fitted curves by the proposed formulas. In this section we will provide an independent experimental measurement and study, to show that the complex SRR-ELC structure can be designed and might be useful to implement materials with a broadband negative index.(NIMs) We recall this experiment to further indicate the important use of our proposed fitting formulas.

In 2000, the first NIM was demonstrated at microwave frequencies [10, 11], as discussed earlier. Rather than being synthesized from natural materials, the implementation of NIMs were formed through an artificially structured metamaterial, constituted by an array of subwavelength resonant structures. Consistent with Veselago's recipe, two types of components were used to form the NIM metamaterial: split

ring resonators (SRRs), which provide a magnetic resonance predominantly and having a frequency band over which the permeability is negative [1]; and wire media, which provide a predominantly electric resonance that results in a negative permittivity at all frequencies below plasma frequency [42]. A surge of interest in both the properties of negative refraction and of artificial materials in general followed this demonstration.

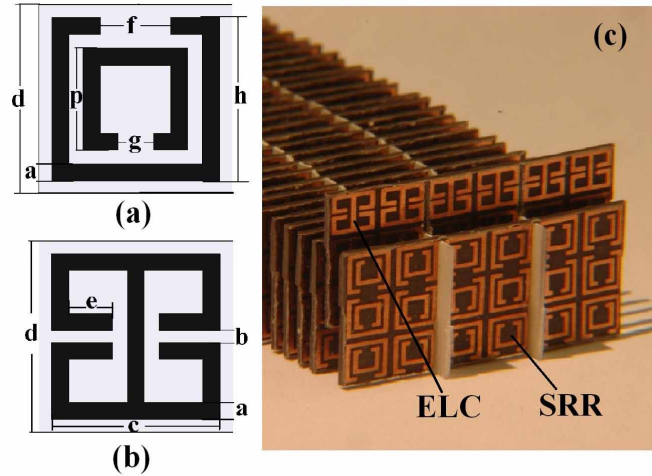


FIGURE 2.28: SRR and ELC composite structures [10]

The SRR-and-wire design or its variants has been typically adopted for the design of NIM metamaterials. The convenience of such a design comes from the relative ease of overlapping the narrow negative permeability band of the SRRs with the much broader negative permittivity band of the wires. In addition, the wires and SRRs typically do not couple with each other significantly, so that their respective responses mostly remain when combined together.

Even though the design of SRR-wire composite structures has already been typically used for the implementation of NIMs, achieving negative permittivity through a continuous wire medium also has unavoidable disadvantages. At first it is difficult to achieve very small unit cell size because of the limitation in spacing the wire medium. The plasma frequency of wire increases on the lattice spacing, making the

smaller unit cell size problematic [42]. In spite of the unit cell scale, the greater consequence is the strong spatial dispersion due to the unavoidable and significant coupling among wires [42]. Without careful design, SRR and wire NIMs can only be regarded as a medium along the principal axes.

A wire medium also can be used to generate negative permittivity even when the wires are not electrically continuous, that is, not infinite long. The introduced cut arranged periodically along the wire will provide capacitance, working together with the existing inductance in the wires to form circuit resonance. Rather than exhibiting negative permittivity at all frequencies below plasma frequency, such cut wire yields the Drude-Lorentz model, only providing negative permittivity between the resonant frequency and plasma frequency. The resonant frequency is, however, extremely sensitive to the characteristics of the gap between the wires, dramatically increasing the difficulty of design. To resolve such sensitivity, several varieties of cut wires have been introduced [13, 50, 51]. However, those different classes of wires remain, though a little bit better, very sensitive to the termination at the cut. Moreover, the plasma frequency is almost independent of the gaps, which consequently unchange the lattice constant with respect to the wavelength from continuous to cut wires. Finally, in terms of the concepts, continuous wire or cut wire cannot be regarded as a 3D particle, but at most a 2D array.

To resolve the difficulties inherent in using continuous wires, an alternative structure, an electric LC resonator (ELC), was developed in which the resonance was set by the internal inductance and capacitance within the unit cell, rather than the strong coupling cell-to-cell.[46, 52] The details of ELC's mechanism have been analyzed in the previous section, who has an electric resonance. As discussed earlier, these ELC structures can be thought of as two SRRs placed back-to-back to generate two de-coupled magnetic dipoles, eventually forming the electric response. Thus, the electric resonance can be easily controlled by varying the geometry parameters (e.g.

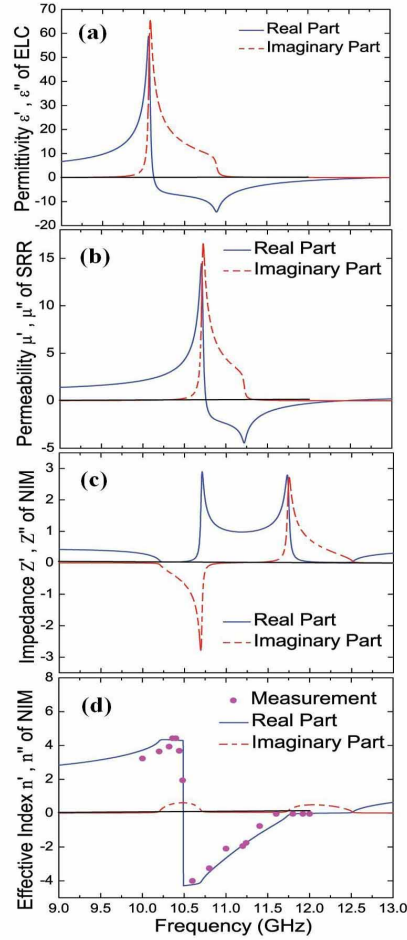


FIGURE 2.29: Retrieval of (a) SRR's permeability; (b) ELC's permittivity (c) SRR-ELC's index (d) SRR-ELC's impedance [10]

the gap and the length of the arms), while it remains insensitive to the cell-to-cell coupling. Such structures, compared to a wire medium, can be regarded as electric resonant particles in 3D.

In this work[49], the intuition is to present a NIM metamaterial, rather than placing the composite medium through wires and SRRs, constructed by a new composite particle composed of electric and magnetic resonators, i.e. SRRs and ELCs, as shown in Fig. 2.28a and Fig.2.28(b), respectively. Instead of using the ELC design in [46], we introduced two capacitive gaps to lower the electric resonant frequency

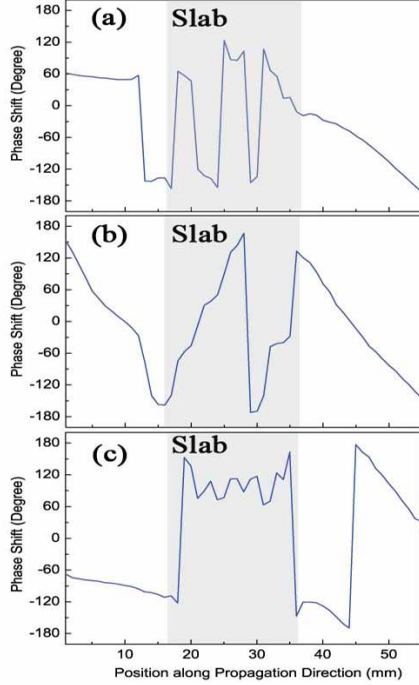


FIGURE 2.30: Phase variation in a (a) positive index regime; (b) negative index region (c) zero-index region [10]

[53], making it closer to the magnetic resonant frequency of the SRRs. The NIM is built by alternating the ELC and SRR planes transverse to the wave propagation direction, as shown in Fig. 2.28 (c).

To achieve the final NIM design in Fig. 2.28, transmission and reflection simulations were performed by using HFSS(Ansoft), a full-wave electromagnetic solver. The effective permittivity and permeability could be found through the standard retrieval process as discussed before. [3]. The responses of the SRR and ELC arrays were first investigated separately by adjusting the geometry parameters until the resonant frequencies of the two structures were nearly identical. Fig. 2.29 (a) and Fig. 2.29 (b) show the optimized permeability of SRR and the permittivity of ELC, respectively. The negative magnetic response occurs, through careful design, from 11.4 GHz to 12.5 GHz, while the negative electric response happens from 10.8 GHz to 13 GHz. According to the plot of the electric and magnetic responses by

SRR and ELC arrays, a regime of negative index can be expected in the SRR-ELC combination structure when the negative permeability range in Fig. 2.29 (a) overlaps with the negative permittivity band in Fig. 2.29 (b). Fig. 2.29 (d) indicates the achieved negative index regime extending from 10.5 GHz to 11.6 GHz, which is somewhat lower than the expectation from SRR and ELC design. Such difference can be explained by the cross-coupling of SRR and ELC resonators, which enhance the capacitance each other. Besides the negative index, the NIMs can also be designed with impedance match to free space through carefully keeping the dispersion of electric and magnetic resonance close to each other. The relatively broad range of impedance match is shown in Fig. 2.29 (c), which is more difficult for the SRR-wire design.[10]

To confirm the NIM design experimentally, we fabricated the SRR-ELC composite structure on a Duroid 5880 circuit board laminate (Hughes Circuits, San Diego; thickness 0.381mm, $\epsilon = 2.33 + i0.003$ and $\mu = 1$) in the lab. The dimensions of each SRR and ELC design are marked in Fig. 2.28(a) and Fig. 2.28(b). The sample has 6 unit cells depth along propagation direction with height of three unit cells (i.e. 1cm), as shown in Fig. 2.28(c). The phase dependent electric field distribution was measured in a planar waveguide apparatus (2D mapper) described elsewhere [51]. The phase variation along the propagation direction (after and inside the sample) is presented in Fig. 2.30 for three different frequencies, corresponding to three types of index-conditions.

Using plots of the phase variation over the NIM, we can evaluate whether the field plots are consistent with our simulated index. At 11.24 GHz the index of the NIM is negative, as shown in Fig. 2.29(d). Likewise, the phase variation within the NIM is opposite to the phase variation outside the NIM, as shown in Fig. 2.30(b). For comparison, the variation of the phase at 10.4 GHz, where the NIM has positive index, is shown in Fig. 2.30(a). The standing waves are the result of impedance

mismatch between the slab and free space regions. Finally, Fig. 2.30(c) reveals that the phase variation at 11.96 GHz is nearly constant, consistent with the index being near zero, as indicated in Fig. 2.29(d).

The propagation constant (real part of the index) can be directly measured through the phase variation over the NIM. The index of NIM at 11.24 GHz is negative shown in Fig. 2.29(d). The corresponding phase variation inside the NIM slab is opposite to that outside due to the backward wave propagation, as shown in Fig. 2.29(b). The positive index regime at 10.4 GHz is shown in Fig. 2.29(a) for comparison, in which the standing waves come [or wave comes] from the impedance-mismatch from NIM slab to free space. Fig. 2.30 (c) reveals that the phase variation at 11.96 GHz is nearly constant, consistent with the index near zero as indicated in Fig. 2.30(d). The phase cannot correlate to index exactly for a finite thickness sample, where the multiple reflection generally leads to a standing wave pattern. However, a fairly good direct measurement can be obtained by taking the standing wave pattern into account. The measurement of the propagation constant is shown in Fig. 2.29(d), which is quantitatively in excellent agreement with the expectation from simulation and design. The phase curves are of three different types, as indicated in Fig. 2.30: travelling waves, standing waves and index near zero, respectively, corresponding to Fig. 2.30 (a)-(c). For standing waves, Fig. 2.30 (a) gives an example of a periodic "square" phase pattern if unwrapping the phase plot. To obtain the effective propagation constant, we measure the ratio of the standing wave phase change periodicity along the propagation direction inside and outside the slab. For travelling waves such as that shown in Fig.2.30 (b), we can measure the slope of the phase variation inside and outside the NIM slab. The near zero index regime can be straightforwardly indicated in Fig. 2.30 (c).

Therefore, the SRR-ELC NIM can be designed and verified through experiment. Since the fundamental component excludes the wire medium, such structures also

can be regarded as NIM particles-the basic structure to implement a negative index, having the advantage of being extendable to 3D NIM design. Despite the NIM design, on the other hand, the SRR-ELC composite medium also has the function of electric and magnetic responses, which can be controlled by tuning each structure relatively independently. Thus, such composite media can give more flexibility in terms of implementing different sorts of metamaterials.

In conclusion, we demonstrate an experiment to show a designed complex metamaterial structure that contains both electric and magnetic resonances. The measured material parameters agreed with the full wave simulation and our proposed fitting formulas in the last section. However, in this experiment we restricted the polarization to TE mode and thus no polarization rotation can be motivated by the potential magnetoelectric coupling[8]. Such a complex structure will behave differently in a free space experiment.

Some of the work in this chapter has been published in Physical Review E [7], Physical Review B [44] and Applied Physics Letters [49].

Rapid design approach for metamaterials

3.1 Advanced rapid design of metamaterials

In the last chapter, we discussed the effective medium theory and a general fitting formula. In this chapter, we will take advantage of the spatial dispersion theorem and the general fitting formula to initiate a rapid design approach.

To make clear the thread of metamaterial design, we include a short review of the various metamaterial designs of the past. The negative index metamaterial (an electromagnetic media with simultaneous negative permittivity and permeability) that sparked the surge of the interest in designing novel metamaterials was constructed by a subwavelength resonant structure—split ring resonator and conducting wire.[1, 10, 11, 42, 43] Utilizing the same technology, the negative refraction phenomenon in a negative index metamaterial was also verified later by experiment.[10] Because the electromagnetic properties of metamaterials is largely dependent on the resonance of the unit cell structure, the operational frequency of a metamaterial can be engineered by careful design of the resonator, and thus a higher frequency such as terahertz and optical range metamaterial can be designed and fabricated by shrink-

ing the unit cell size. [22, 23, 24, 25] Recently, a broadband non-resonant element was also used to design low loss and broadband metamaterials.[26, 54] Although this type of metamaterial works below the resonant frequency, it is still constructed by different types of conducting scatter and the unit cell structure design also greatly affects its anisotropy and dispersion on both the refractive index and impedance.

More recently, parallel work developing metamaterials was conducted from the optical control point of view. A technology named transformation optics was proposed to control the wave propagation by using complex media.[24, 25, 26, 27, 28, 29, 30, 31, 32, 33, 34] The idea is to artificially create a coordinate transform and then implement such transformation to electromagnetic waves by mapping the transformed space with a new set of materials. Usually the required material from transformation optics is highly anisotropic and inhomogeneous. Because such complex media are difficult to find in the extant natural materials, the metamaterial element became a suitable and promising candidate to physically implement transformation optics design. One of the most compelling illustrations of this technology is to make an invisible cloak that can render invisible the waves around a target.[24, 25, 26] A series of experiments has been conducted to verify the transformation optics design and to illustrate sophisticated fabrication technology for metamaterials.[25, 26, 55, 56]

Therefore, the demand for designs of highly complex subwavelength unit cell structures is increasing dramatically as the field advances. To characterize and design the metamaterial unit cell structure, a standard electromagnetic retrieval process is widely used, in which a full wave simulation is required to obtain the S-parameter.[3] Utilizing this standard retrieval process, the equivalent permittivity and permeability of metamaterials can be numerically extracted and characterized. According to this algorithm, it is found that the simulated metamaterial unit cell is usually highly dispersive and contains complex resonances. Some earlier studies proposed that the metamaterials can be analyzed by a Drude-Lorentz resonance model under the as-

sumption of infinitesimal unit cell size.[1, 42, 43] However, in reality the unit cell size is usually a tenth of wavelength due to fabrication limitations. The dispersion behavior thus is quite different from the ideal Drude-Lorentz resonance. It is known that the finite size on unit cell results in a strong spatial dispersion effect (a dispersion relates to the lattice property of the metamaterial unit cell array) in metamaterials. This spatial dispersion effect makes the Drude-Lorentz model invalid for describing and making the regression on the metamaterial's response.[3, 5, 7, 8, 10, 46] A series of revised formulas was proposed to describe and predict the practical metamaterial response.[23] Because of the complexity in analyzing metamaterials, the entire metamaterial unit cell structure design relies solely on the standard retrieval process and the full wave simulation. For instance, to achieve a reduced cloak design in [25], ten different unit cell designs were required to achieve the inhomogeneous media property. For each individual unit cell design, a number of iterations were conducted to optimize the unit cell geometry for certain permittivity and permeability values at operational frequency. For each iteration, a numerical full wave simulation must be done to achieve the equivalent permittivity and permeability. A large amount of time was required in design such complex media. In addition, more complex structures such as electric and magnetic dual resonant structures were proposed to achieve various permittivity and permeability values, which contain more complicated spatial dispersion effects and requires extra time in full wave simulation[3] Therefore, the lack of a rapid metamaterial design system increasingly becomes a bottleneck for complex media design.

To make progress with a design method, a general fitting formula is proposed to calculate the regression on the unit cell's response. Although the parameter does not indicate the same physics origin as the description in effective medium theory and the field average, such variables can still appear in a clear resonance form. By using this mathematical formula, one can perform an accurate regression on

an arbitrary metamaterial unit cell. By doing so, we can use a series of fitting parameters to represent the complex dispersion behavior from a standard retrieval process. Meanwhile, the metamaterial property can be engineered by designing the physical unit cell structure. We can then establish a function from the structural geometry to the corresponding fitting parameters. Once we obtain such a function analytically, we no longer need to make massive full wave simulations of different unit cells in the design iteration. We call this function the design library.

The next challenge is the approach to extract such a design library through some preliminary simulations by varying certain geometric dimensions. To solve this problem, a Taylor expansion is adopted to establish a link between the particle response and the geometric dimensions. We use a matrix inverse technique to extract the coefficient in our design formulas, whose computational complexity is proportional to the order of the dimensions and their coupling terms. This approach is flexible because: (1) any complicated particle can be copied with a standard extraction procedure; (2) the system can be self-improved as long as increasing any data point in the design space and (3) it can be applied to extract the modulation formulas for active and tunable metamaterials.

To begin, we first back-up the complex medium theory proposed in [4].

$$\begin{aligned}\tan(\theta/2) &= S_d \omega p \sqrt{\bar{\mu}_m \bar{\varepsilon}_m} / 2 \\ \eta &= \sqrt{\frac{\bar{\mu}_m}{\bar{\varepsilon}_m}}\end{aligned}\tag{3.1}$$

in which

$$\begin{aligned}\bar{\varepsilon}_m &= \bar{\varepsilon}_1 F / \cos(\theta/2) \\ \bar{\mu}_m &= \bar{\mu}_1 A / \cos(\theta/2)\end{aligned}\tag{3.2}$$

The $\bar{\epsilon}_m$ and $\bar{\mu}_m$ are the average parameters for the metamaterial's transformation, while $\bar{\epsilon}_1$ and $\bar{\mu}_1$ are the particle's response defined by the field average. Generally, $\bar{\epsilon}_1$ and $\bar{\mu}_1$ experience the Lorentz resonance forms as a particle response. According to the transformation, $\bar{\epsilon}_m$ and $\bar{\mu}_m$ can exactly keep the same Lorentz form without determining A and F through specific particle classification, but with a quantity shift.

According to Eq.(3.1), we again set up the relationship between the particle response (m-parameters) and the system behavior (effective parameters). To calculate the particle response, we can back up $\bar{\epsilon}_m$ and $\bar{\mu}_m$ from S-parameter through a standard retrieval and complex medium theory, which can be used to analyze any resonant particles or combination particles.

The Lorentz multiple resonances form for $\bar{\epsilon}_m$ and $\bar{\mu}_m$ yields

$$\bar{\epsilon}_m = \epsilon_a \left(1 - \sum_n \frac{F_{en} f^2}{f^2 - f_{en}^2 + i\gamma_{en} f} \right) \quad (3.3)$$

$$\bar{\mu}_m = \mu_a \left(1 - \sum_n \frac{F_{un} f^2}{f^2 - f_{un}^2 + i\gamma_{un} f} \right) \quad (3.4)$$

All the parameters in Eq.(3.3)-(3.4) are the function of the particle's geometric dimensions. Although a full theoretical analysis on the specific structure is possible, using the Taylor expansion technique to fit all variables takes advantage of design generality and can avoid complicated but redundant analysis, given our goal of controlling and rapidly designing the complex particles. For example, if there are two geometric dimensions s and r , the F , f and γ can be expanded by s and r . Rigorously speaking, it has to take sufficient terms for convergency. However, when

restricting the range of the parameters s and r , and the frequency regime of interest, the extracted design formulas with a Taylor expansion with a small number of terms is enough for most of the cases. All the coefficients incorporated in the Taylor expansion can be extracted through randomly simulated data in s and r space and the inverse of the matrix. A flow chart of this rapid design approach can be seen in Fig. 3.1.

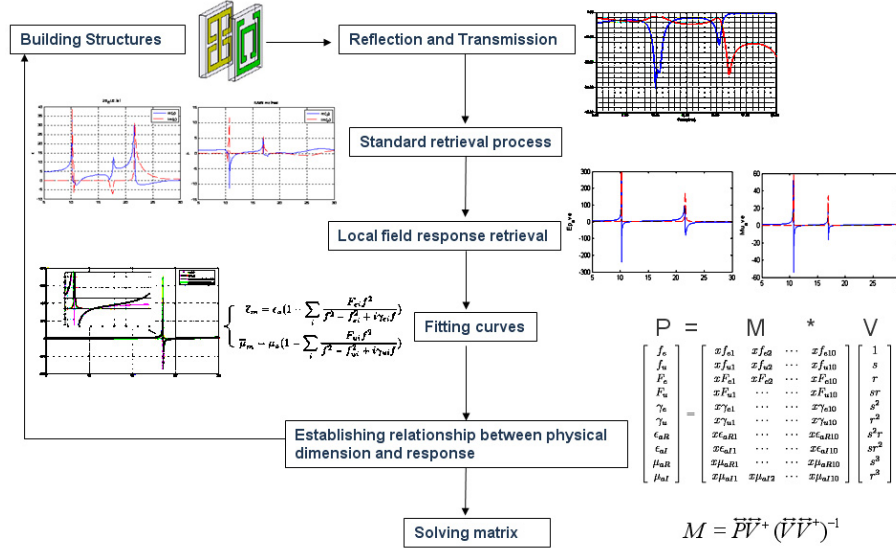


FIGURE 3.1: Flow chart of rapid design approach for metamaterials

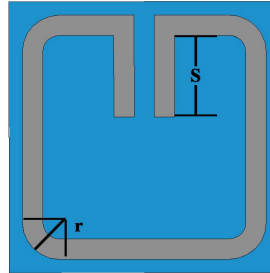


FIGURE 3.2: SRR unit cell structure

As an example of the proposed approach, we consider the SRRs particle, shown in Fig.3.2. We consider the response separately from s and r , and also their coupling term. SRRs has, in addition to the fundamental magnetic resonance, a higher order

electric resonance. To give the full design formulas for SRRs, we should take into account both the magnetic and electric resonances, shown in Fig.3.3. The effective parameter retrieval and particle response (m-parameters) retrieval clearly show these two resonances.

$$\bar{\epsilon}_m = \epsilon_a \left(1 - \frac{F_e f^2}{f^2 - f_e^2 + i\gamma_e f} \right) \quad (3.5)$$

$$\bar{\mu}_m = \mu_a \left(1 - \frac{F_u f^2}{f^2 - f_u^2 + i\gamma_u f} \right) \quad (3.6)$$

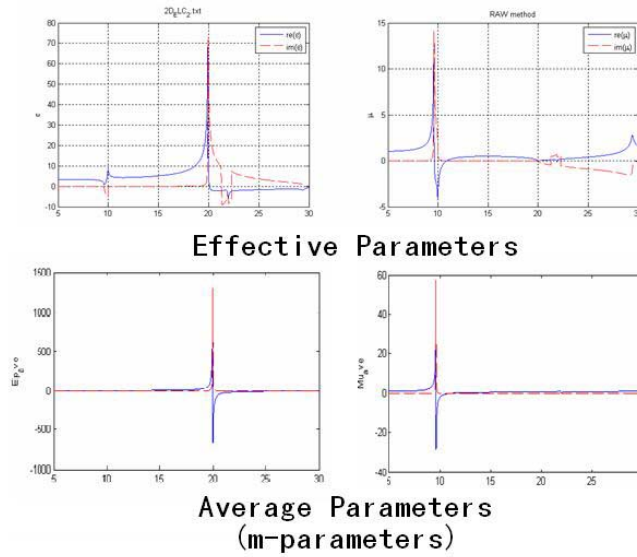


FIGURE 3.3: Particle retrieval of SRR unit cell structure

To establish the design library via a Taylor expansion, we can write down the expansion formulas as follows:

$$\begin{bmatrix} f_e \\ f_u \\ F_e \\ F_u \\ \gamma_e \\ \gamma_u \\ \epsilon_{aR} \\ \epsilon_{aI} \\ \mu_{aR} \\ \mu_{aI} \end{bmatrix} = \begin{bmatrix} x f_{e1} & x f_{e2} & \cdots & x f_{e10} \\ x f_{u1} & x f_{u2} & \cdots & x f_{u10} \\ x F_{e1} & x F_{e2} & \cdots & x F_{e10} \\ x F_{u1} & \cdots & \cdots & x F_{u10} \\ x \gamma_{e1} & \cdots & \cdots & x \gamma_{e10} \\ x \gamma_{u1} & \cdots & \cdots & x \gamma_{u10} \\ x \epsilon_{aR1} & \cdots & \cdots & x \epsilon_{aR10} \\ x \epsilon_{aI1} & \cdots & \cdots & x \epsilon_{aI10} \\ x \mu_{aR1} & \cdots & \cdots & x \mu_{aR10} \\ x \mu_{aI1} & x \mu_{aI2} & \cdots & x \mu_{aI10} \end{bmatrix} \begin{bmatrix} 1 \\ s \\ r \\ sr \\ s^2 \\ r^2 \\ s^2 r \\ sr^2 \\ s^3 \\ r^3 \end{bmatrix} \quad (3.7)$$

Eq.(3.7) expands all the parameters with respect to the dimensions s and r by a third order approximation. The coefficients in the main matrix (x-parameters) need to be extracted from massive simulations. For one simulation we can obtain the frequency dependence extracted parameters, from which we can at first extract all the parameters such as f_e, f_u, F_e, F_u for the specific dimension s and r , shown in Fig.3.4. The expansion works very well in a broad band regime below the electric resonance. (We prioritize the accuracy below the electric resonant frequency due to our interest in SRRs.) At higher frequencies above the electric resonance, the discrepancy might be due to higher order modes. If the reader is still interested in those regimes, one can definitely separate the frequency domain and interpret different extracted coefficients. Many details of extracting the appropriate Lorentz formula coefficients actually play a critical role in the systematic performance, although the technique is trivial.

The next issue is the appropriate method for rapidly extracting the 10 expanding coefficients for each parameter. Assuming N data points in s - r space have been taken, we can approximate the matrix form as

$$b = xA \quad (3.8)$$

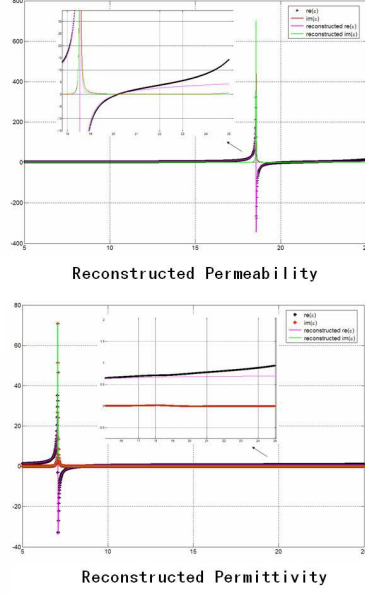


FIGURE 3.4: Reconstruction curve from particle retrieval

in which,

$$b = \begin{bmatrix} f_{e1} & f_{e2} & \cdots & f_{eN} \\ f_{u1} & f_{u2} & \cdots & f_{uN} \\ F_{e1} & F_{e2} & \cdots & F_{eN} \\ F_{u1} & F_{u2} & \cdots & F_{uN} \\ \gamma_{e1} & \gamma_{e2} & \cdots & \gamma_{eN} \\ \gamma_{u1} & \gamma_{u2} & \cdots & \gamma_{uN} \\ \epsilon_{aR1} & \epsilon_{aR2} & \cdots & \epsilon_{aRN} \\ \epsilon_{aI1} & \epsilon_{aI2} & \cdots & \epsilon_{aIN} \\ \mu_{aR1} & \mu_{aR2} & \cdots & \mu_{aRN} \\ \mu_{aI1} & \mu_{aI2} & \cdots & \mu_{aIN} \end{bmatrix} \quad (3.9)$$

$$x = \begin{bmatrix} x f_{e1} & x f_{e2} & \cdots & x f_{e10} \\ x f_{u1} & x f_{u2} & \cdots & x f_{u10} \\ x F_{e1} & x F_{e2} & \cdots & x F_{e10} \\ x F_{u1} & \cdots & \cdots & x F_{u10} \\ x \gamma_{e1} & \cdots & \cdots & x \gamma_{e10} \\ x \gamma_{u1} & \cdots & \cdots & x \gamma_{u10} \\ x \epsilon_{aR1} & \cdots & \cdots & x \epsilon_{aR10} \\ x \epsilon_{aI1} & \cdots & \cdots & x \epsilon_{aI10} \\ x \mu_{aR1} & \cdots & \cdots & x \mu_{aR10} \\ x \mu_{aI1} & x \mu_{aI2} & \cdots & x \mu_{aI10} \end{bmatrix} \quad (3.10)$$

and

$$A = \begin{bmatrix} 1 & 1 & \cdots & 1 \\ s_1 & s_2 & \cdots & s_N \\ r_1 & r_2 & \cdots & r_N \\ s_1 r_1 & s_2 r_2 & \cdots & s_N r_N \\ s_1^2 & s_2^2 & \cdots & s_N^2 \\ r_1^2 & r_2^2 & \cdots & r_N^2 \\ s_1^2 r_1 & s_2^2 r_2 & \cdots & s_N^2 r_N \\ s_1 r_1^2 & s_2 r_2^2 & \cdots & s_N r_N^2 \\ s_1^3 & s_2^3 & \cdots & s_N^3 \\ r_1^3 & r_2^3 & \cdots & r_N^3 \end{bmatrix} \quad (3.11)$$

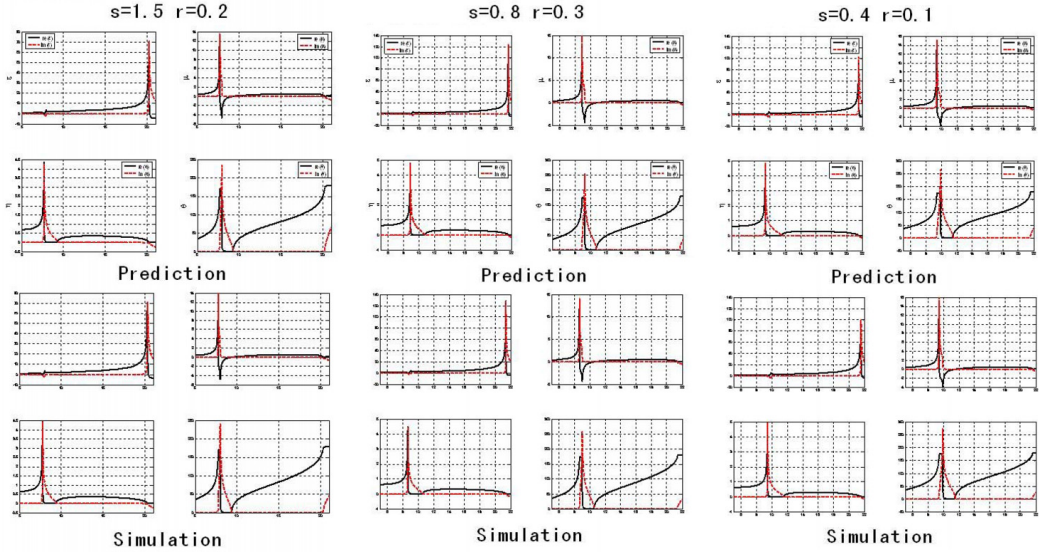


FIGURE 3.5: Calculation on SRR unit cell structure

To solve the coefficient matrix x , we can deduce Eq.(3.8) that

$$bA^\dagger = xAA^\dagger \quad (3.12)$$

in which, A^\dagger represents the Hermite matrix of A . Hence, we easily obtain the least-square solution of the retrieved parameters:

$$x = bA^\dagger(AA^\dagger)^{-1} \quad (3.13)$$

As an example of Roger 5880 Duroid substrate SRRs, we obtain the coefficient matrix and make a comparison in Fig. 3.5. It is obvious that this approach can extract much more accurate and general design formulas by a standard procedure. Such a method can be expanded to tunable and active metamaterials by adding the terms of modulations. The coefficient matrix can also be self-improved as long as new data points can be added in. Thus, we can improve the coefficients whenever we use the design formulas and make confirmation simulations for specific designs. This approach opens the window to a sophisticated metamaterials design system. Recall that the entire sophisticated design system is based on the most fundamental effective medium theory and spatial dispersion analysis.

3.2 Advanced Bayesian statistics approach to metamaterial design

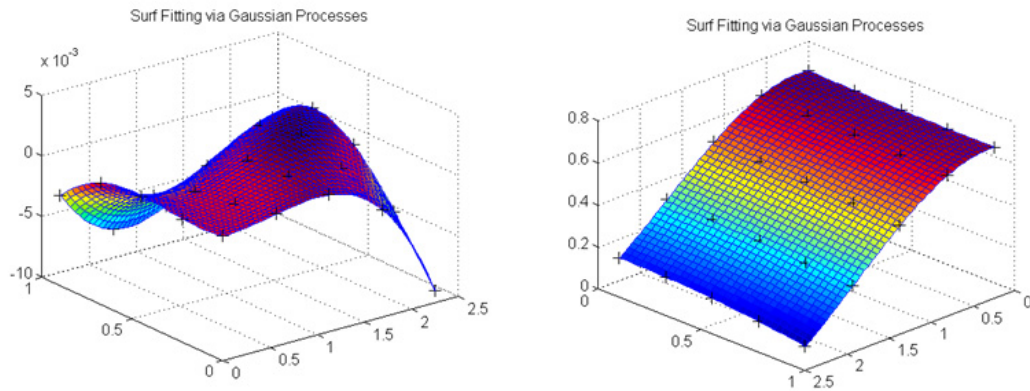


FIGURE 3.6: Nonlinear regression on the parameters' response in SRR design

In the last section, we proposed an advanced rapid metamaterial design system by integrating the spatial dispersion model and least square method to overcome the low design efficiency for metamaterials. However, the regression process and searching algorithm is still limited by the paucity of full wave simulation data that can be achieved in advance. Therefore, in this section we will use advanced statistical

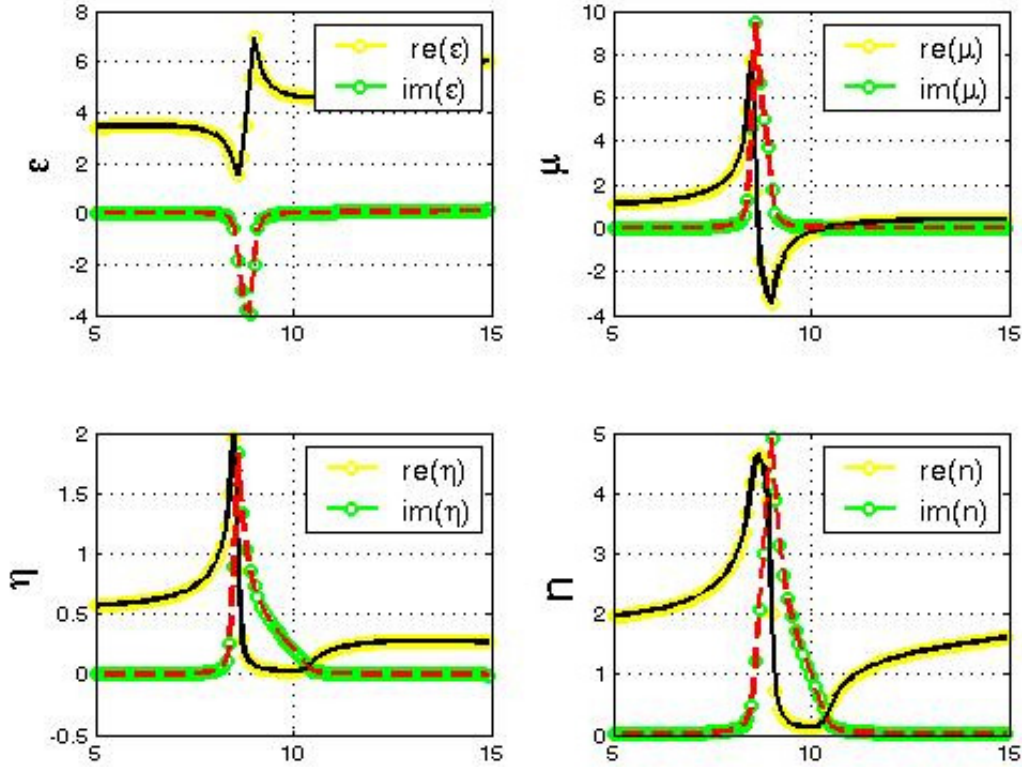


FIGURE 3.7: Prediction of the SRR’s response is indicated by the colored line, compared to the full wave simulation, indicated by the solid line.

approaches that can better make use of the restricted availability of preliminary full wave simulation data. The frame is still to make use of a revised spatial dispersion model to remove the complexity from the spatial dispersion and make a full regression on the unit cell’s response. Once the regression model is built, we can design complex media [or: design a complex medium (media is plural, medium is the singular form)] without running the full wave simulation. After this we will introduce an approach to remove the spatial dispersion effect and make [perform a] a regression to metamaterial unit cell structures, and then introduce a nonlinear regression approach—Gaussian processes to interpolate the response space with varying geometry. In the last section, we will introduce a sequential Monte Carlo computational approach to search for the required unit cell’s geometric structure for designing

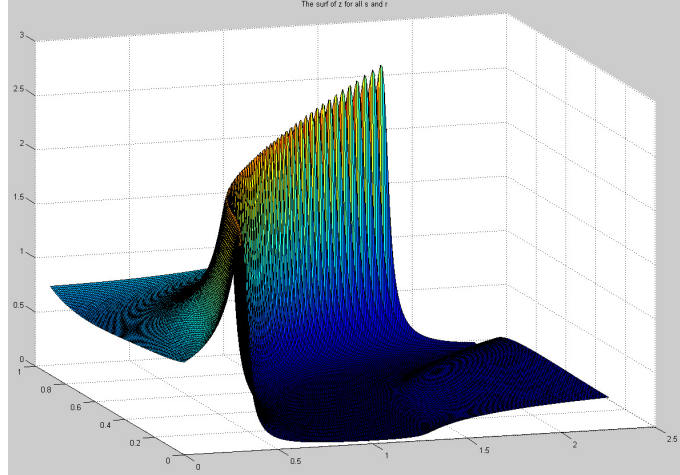


FIGURE 3.8: The impedance design at a particular point in the search process.

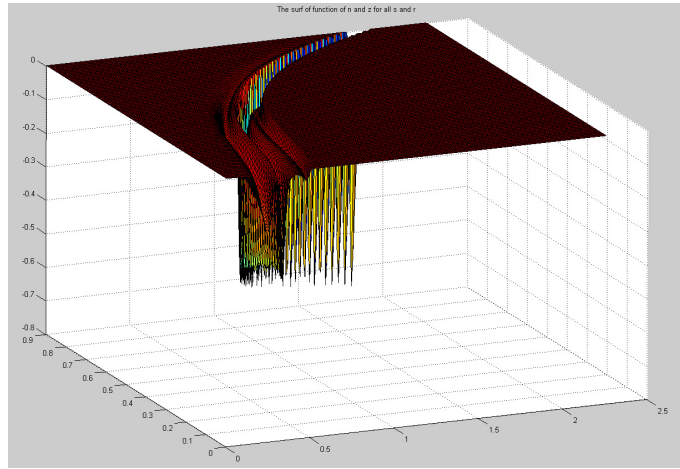


FIGURE 3.9: The index design at a particular point in the searching process. The lowest valley indicates the optimized location in the space

complex gradient index metamaterials. A design example is also provided.

In the introduction we have noted that the metamaterial's response is highly distorted by the spatial dispersion effect and cannot be described by the Drude-Lorentz model. This complexity makes it difficult to fit the dispersion curve by a simple analytical model, and requires full wave simulations in the current iterative design process. To address this challenge, we will use a simple analytical model that can describe the spatial dispersion effect and be used to fit the complex dispersion curve of metamaterials. In Ref.[7], a theoretical model of the practical metamaterial

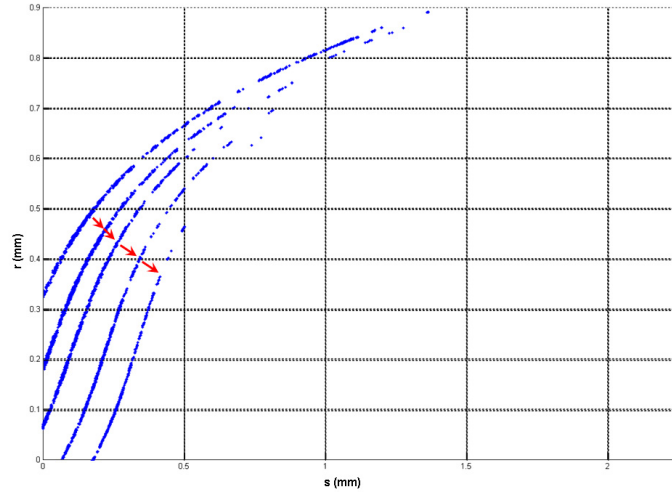


FIGURE 3.10: Demonstration of SMC approach to design a gradient index media

unit cell structure was proposed, in which a set of formulas that can be used to fit

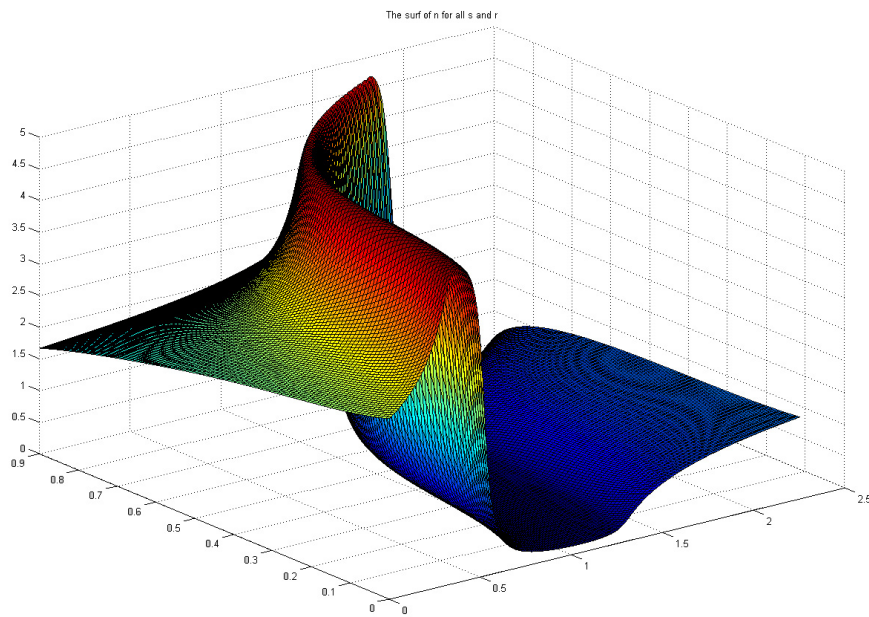


FIGURE 3.11: Refractive index value changing [changes with] with the dimension s and r .

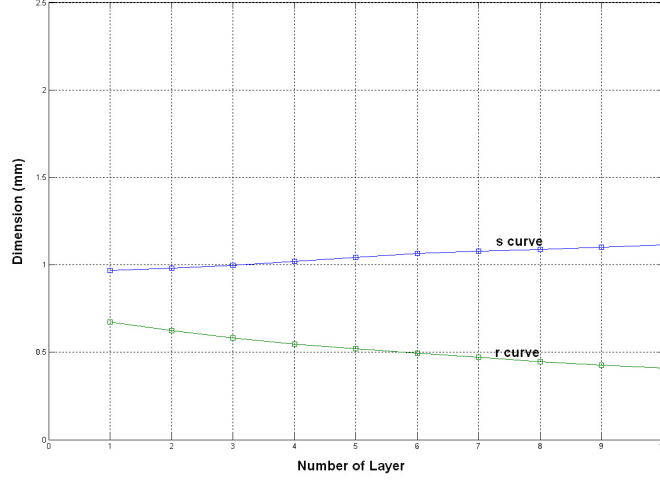


FIGURE 3.12: The optimization of the gradient index design from $n=2.3$ to $n=3.6$ by ten layers

the magnetic or electric resonator was expressed as

$$\begin{aligned}\varepsilon_{\text{eff}} &= \bar{\varepsilon} \cdot \frac{(\theta/2)}{\sin(\theta/2)} [\cos(\theta/2)]^{-S_b} \\ \mu_{\text{eff}} &= \bar{\mu} \cdot \frac{(\theta/2)}{\sin(\theta/2)} [\cos(\theta/2)]^{S_b}\end{aligned}\quad (3.14)$$

in which θ is the phase advance across one unit cell and yields $\sin(\theta/2) = S_d \omega p \sqrt{\bar{\varepsilon} \bar{\mu}}/2$ (p is the lattice periodicity of the metamaterial unit cell array and S_d is equal to 1 or -1 to guarantee the positive imaginary part on θ for the passive media condition). A difference S_b value is applied for different type of resonators. For a magnetic resonator, such as a split ring resonator (SRR), $S_b = -1$. For an electric resonator, such as an electric LC resonator (ELC), $S_b = 1$.

Although it has been shown that this analytical model can adequately describe the unit cell response containing a single resonance at a certain frequency range, this formula can only provide the fitting to a single electric or magnetic resonance. To overcome this limitation, we provide a modified formula that can be flexibly used to

fit more complex structures.

$$\begin{aligned}\epsilon_{eff} &= \frac{\theta/2}{\tan(\theta/2)} \bar{\epsilon}_m \\ \mu_{eff} &= \frac{\theta/2}{\tan(\theta/2)} \bar{\mu}_m\end{aligned}\tag{3.15}$$

in which

$$\begin{aligned}\bar{\epsilon}_m &= \epsilon_a \left(1 - \sum_i \frac{F_{ei} f^2}{f^2 - f_{ei}^2 + i\gamma_{ei} f} \right) \\ \bar{\mu}_m &= \mu_a \left(1 - \sum_i \frac{F_{ui} f^2}{f^2 - f_{ui}^2 + i\gamma_{ui} f} \right)\end{aligned}\tag{3.16}$$

We notice that this fitting formula is of no interest to physics and will be explained somewhere else. But the benefit of introducing such a formula is that we can use it as a general fitting model for some complex structures such as a combination of a split ring resonator(SRR) and an electric-LC resonator (ELC).[10, 11] Although such dual resonant structures might cause the magnetoelectric coupling effect[8], the coupling can be controlled and reduced by careful arrangement on the unit cell array. The emphasis here is on making use of this fitting formula to mathematically fit the complex electromagnetic parameter curve using a standard retrieval process. Recall that Fig.2.6 indicates an excellent match between the fitting model and the HFSS simulated results by setting $f_e = 10.205\text{GHz}$, $f_u = 10.703\text{GHz}$, $F_e = 0.2445$, and $F_u = 0.2688$, $\gamma_e = 0.02\text{GHz}$, $\gamma_u = 0.0245\text{GHz}$. The advantage of using the fitting model is that complex frequency-dispersive curves can be represented by a few fitting parameters. Therefore, we can use those fitting parameters to represent the response from a specific metamaterial structure. Once the structure is modified, the fitting parameters will also be changed. To initiate the rapid design approach, we will establish the function between the structure and these fitting parameters.

In this section, we will establish the relationship between the unit cells' geometry and their response presented by the fitting formulas. Because the fitting process is almost identical for different types of metamaterial structures, we will take the SRR structure here as our example. The SRR is usually regarded as a magnetic resonator. However, according to the standard retrieval, we can see that an electric resonance occurs after the fundamental magnetic resonance. Therefore, we will take into account both the electric and the magnetic resonance together in the fitting process and make use of Eq.3.15-3.16.

It is known that if we modify the geometry such as the length of the arm s or the radius at the corner r , the corresponding response will vary, resulting in different value for the fitting parameters[25]. To obtain the response of a specific structure, a full wave simulation is necessary to extract the effective permittivity and permeability based on the standard retrieval process. This full wave simulation is also the most time consuming step in the metamaterial design process. We therefore need to develop an approach that can avoid the full wave simulation and accurately predict the response of the metamaterial unit cell. The approach is to make some preliminary simulations for different unit cell structures (structures with different s and r). Then we make an interpolation on the structure geometry dimension and the response(those fitting parameters from the general fitting formula). The intuitive idea is to use the Taylor expansion to the fitting parameters with respect to s and r in the last section. However, we have no principle to justify how many terms we should retain. Therefore, we propose a method called a non-parameter regression to overcome this difficulty. Specifically, we will make a use of a Gaussian process, one kind of such non-parameter regression methods, to predict the unit cell response.

A Gaussian process can be regarded as defining a distribution over functions, and inference taking place directly in the space of functions [21]. Consider a stochastic process which defines a distribution $\mathcal{P}(\cdot)$ over functions f , where f maps some input

space \mathcal{X} to \mathcal{R} . f is infinite dimensional but the x values index the function $f(x)$ at a countable number of points; we use the data at these points to determine $\mathcal{P}(f)$ in the function space. If $\mathcal{P}(f)$ is a multivariate Gaussian for every finite subset of X , the process is a Gaussian process (GP) and it is determined by a mean function $\mu(x)$ and a covariance function $K(x)$. In the present context, $\mu(x)$ could be some physically attractive function, although we chose a commonly used setting $\mu(x) = 0$ for simplicity of computation. A typical choice of covariance function is $K(x_i, x_j) = \sigma_f^2 \exp(-\frac{(x_i - x_j)^2}{2l^2}) + \sigma_n^2 \delta_{ij}$, where the smoothing parameter l , the signal variance σ_f , and the noise variance σ_n can be learned from the training data, by a certain model selection approach. [21] Then we can use the trained GP to predict new values $f_* = f(x_*)$ for new inputs x_* using the fact that the combined distribution of all values is jointly Gaussian with

$$\begin{bmatrix} y \\ f_* \end{bmatrix} \sim N \left(0, \begin{bmatrix} K(X, X) + \sigma_n^2 & K(X, X_*) \\ K(X_*, X) & K(X_*, X_*) \end{bmatrix} \right) \quad (3.17)$$

, which leads to the predictive equations

$$f_* | X, y, X_* \sim N(\bar{f}_*, cov(f_*)) \quad (3.18)$$

where $\bar{f}_* = E(f_* | X, y, X_*) = K(X_*, X) [K(X, X) + \sigma_n^2 I]^{-1} y$ and $cov(f_*) = K(X_*, X_*) - K(X_*, X) [K(X, X) + \sigma_n^2 I]^{-1} K(X, X_*)$. Regarding our context, we first selected a small number of points X in the unit cell geometry space by some conventional experimental design methods, such as orthogonal experimental design [23]. Then we perform the full wave simulation for the selected unit cells' structure and retrieve their responses y . For any new data points X_* in the unit cell geometry space, the mean prediction f_* and covariance $cov(f_*)$ can be evaluated by a Gaussian process regression. The mean prediction f_* can be regarded as a nonlinear MMSE (minimum mean squared error) estimation for the nonlinear mapping from the geometric

structure to its response. One concern with the GP regression is the prediction uncertainty reflected by the covariance. However, if the variance can be kept within a certain range, the mean prediction can indicate if the design is close enough to the true value, and will result in successful experiments. To control the prediction variance of the GP regression, some adaptive experimental design techniques are employed which proceed as follows: (1) select the x_* which has the greatest standard deviation in predicted output, (2) run a full wave simulation for the point and add it to the training data set (X, y) . By repeating the process a certain number of times, we can force the prediction variance to shrink to a small range, and then the regression will be accurate enough to guarantee success in the experiments.

In the design of a gradient index media system, we need to search for those unit cell geometry structures which have the required responses. More specifically, we define a function $u(x)$ to measure the required response of a unit cell, i.e. the refractive index and impedance, and their tolerated uncertainty. To design a metamaterial media system, we first derive the required responses for all unit cells $U = \{u_n\}$, where n is the index for each unit cell. Then the design process involves a large amount of searching (or optimization) for all unit cells structures that meet the requirements of U . In a gradient index media system, the required response changes gradually. Therefore, by generally assuming that similar unit cell structures have similar responses, we propose an effective searching algorithm based on sequential Monte Carlo methods. We start from an initial index design and sample a number of points which meet the requirement of u_1 (Generally it will be like a curve in space.) When moving to the next gradient index design, we assume that the feasible solutions of u_{n+1} should be near the feasible solutions of u_n for the previous index design point. So we can use a dynamic model to propose a new set of points which are near the feasible solution for u_n and thus have a high probability of being a feasible solution for u_{n+1} . By evaluating the fitness of these new points and resampling according to the fitness, we

can obtain a set of feasible solutions for u_{n+1} . Such a process will enable us to track the motion of the optimized solutions for $u_{1:N}$ sequentially. This process falls into the framework of a sequential Monte Carlo method. Here we give a brief introduction to the SMC sampler and present the algorithm for our searching/optimization problem.

Sequential Monte Carlo (SMC) methods represent a class of important sampling and resampling techniques designed to simulate from a sequence of probability distributions; these have become very popular during the last decade for solving sequential Bayesian inference problems in various disciplines. To apply SMC methods in our searching/optimization problem, we need to transform the function $u_n(\cdot)$ into a probability function $\pi_n(\cdot)$ which has the property that the optimum solutions for $u_n(\cdot)$ have significant probability. Given some sequence of target distributions $\pi_n(\cdot)$, SMC propagates samples forward from one distribution to the next according to a sequence of Markov kernels, K_n , which could be one step propagation in a Random Walk Metropolis-Hastings algorithm with respect to the target distribution $\pi_n(\cdot)$, and then corrects for the discrepancy between the proposal and the target distribution by importance sampling. Moreover, to ensure that a significant fraction of the particle set have non-negligible weights, the particle representation is resampled using some resampling scheme, whenever the effective sample size (*ESS*) is below a prespecified threshold. A sequential Monte Carlo sampler is presented as follows,

Algorithm 1: Sequential Monte Carlo Sampler

- At $n=1$. Sample $X_1^{(i)} \sim \mu_1(\cdot)$ and set $w_1^{(i)} \propto \pi_1(X_1^{(i)}) / \mu_1(X_1^{(i)})$. If needed, resample $\{w_1^{(i)}, X_1^{(i)}\}$ to obtain N new particles $\{N^{-1}, X_1^{(i)}\}$

- At time $n > 1$. For $i = 1, \dots, M$, sample $X_n^{(i)} \sim K_n(X_{n-1}^{(i)}, \cdot)$

$$w_n^{(i)} \propto w_{n-1}^{(i)} \frac{\pi_n(X_{n-1}^{(i)})}{\pi_{n-1}(X_{n-1}^{(i)})}$$

If needed, resample $\{w_1^{(i)}, X_1^{(i)}\}$ to obtain N new particles $\{N^{-1}, X_n^{(i)}\}$.

At each iteration n , we obtain a batch of particles $\{X_n^{(i)}\}_{i=1}^M$, most of which could be feasible solutions to satisfy u_n or to achieve the require responses. Then we can select one point in each iteration to format the final design.

To illustrate this advanced Bayesian statistics metamaterial design methodology, we took the split ring resonator (SRR) as our example, shown in Fig.3.2. By setting the dimension variables s and r , we took a few sampling points to make a regression on the parameter's response to the SRR structure, shown in Fig.3.6. The fitting parameter space can be determined by a Gauss Process approach. The corresponding prediction on SRR's response is illustrated in Fig.3.7, in which the permittivity and permeability are calculated through Eq.3.15-3.16.

Now we can further make use of the SMC algorithm to implement our gradient index metamaterial design. Recall that although a full search can guarantee the global optimization, the time required for setting the searching step makes the approach unsuitable for generalization to different occasions. Fig.3.8 shows the impedance at 10GHz for the SRR structure with respect to its physical dimensions, s and r . We can see that the material response space of the structure dimension is extremely complicated-a very rough surface, resulting in many local optimization points. Therefore, we applied the SMC algorithm and tracking algorithm to resolve this complexity. To achieve a robust gradient index design, we also need to avoid any jump in the structural dimension for the sake of stability in the experiment.

Based on the SMC scheme, we started from an initial index design and sampled as many as possible within a certain time gate to find all the acceptable local optimization points in space. (Generally it will be like a curve in space.) When moving to the next gradient index design, we assume that the local optimization should be near the optimized curve in the previous index design point. So we can use a tracking algorithm to track the motion of the optimized solutions and find the optimized curve for next solution.

Fig. 3.9 demonstrates the cost function for a particular design point. The lowest cost value indicates the optimized location for SRR structures in their geometry space. We can see that it is an irregular valley, within which the structures will all be suitable for the particular index design. Fig.3.10 illustrates the corresponding impedance value. We can see that at the corresponding valley, the impedance is approximately identical to unity by the design. Fig.3.11 demonstrates the dynamic SMC design approach and indicates the motion of the solution valley with the gradient index change. Fig.3.12 shows the final design optimization of a gradient index at 7.0 Ghz. The index is changing linearly from $n=2.3$ to $n=3.5$ with unity impedance.

In conclusion, the above advanced rapid metamaterial design is generally applicable to all kinds of current metamaterial design. A few preliminary sample points are needed to interpolate the metamaterial response space. The use of non-parameter regression techniques can successfully avoid the selection of variables and thus can learn the features of the data to generate the interpolation. We also developed a SMC scheme for the search process, in which multiple solutions have been considered. The sampling and tracking algorithm made it suitable for rapidly designing large scale gradient index metamaterials. To enhance the robustness of the design, we selected further in the multiple solutions to keep the gradient dimension as smooth as possible. The framework also can be used in other complex metamaterial design problems, such as that of designing an invisible cloak. We anticipate it will have

wide-spread application to future metamaterial design problems.

In this chapter, some of the work was done in collaboration with Dr. Chunlin Ji from the Department of Statistics, Duke University. In this collaboration, I was in charge of incorporating the spatial dispersion theorem into the rapid design system and chose the potential algorithm. Dr. Chunlin Ji provided many Bayesian algorithms and implemented the SMC scheme in Matlab.

Waveguided metamaterials and electromagnetic tunnelling experiment

4.1 Concept of waveguided metamaterials

In the last two chapters, we have discussed the effective medium theory for metamaterials and the approach to model and design metamaterials. Whereas another aspect of metamaterials is the structure configuration as one has to use artificial structure to implement the unit cell. Considering the practical RF application, many devices are in the form of waveguide system. Thus we need to develop the effective way to integrate metamaterials into a waveguide. Although one option is to insert the bulk metamaterial structure, the complexity of building and constructing three dimensional structures in the waveguide limit the convenience and cost. In addition, the limited space in the waveguide also increase the difficulty in designing a small metamaterial structure. To address this issue, we propose a configuration of waveguided metamaterials by 2D complementary structure array, for example, using the complementary split-ring resonators (CSRRs) [56, 57] or the complementary electric-LC resonators (CLECs)[58]. According to the Babinet principle, the complementary

structures will have reciprocal responses to its bulk structure. For instance, a split ring resonator (SRR) structure has a fundamental magnetic resonance. The corresponding complementary case, CSRR, has a fundamental electric resonance and can be regarded as an electric unit cell in the waveguide.[56] The configuration of waveguided metamaterials is shown in Fig.4.1, in which, an array of complementary structure is milled out at top or bottom plate in the parallel waveguide.

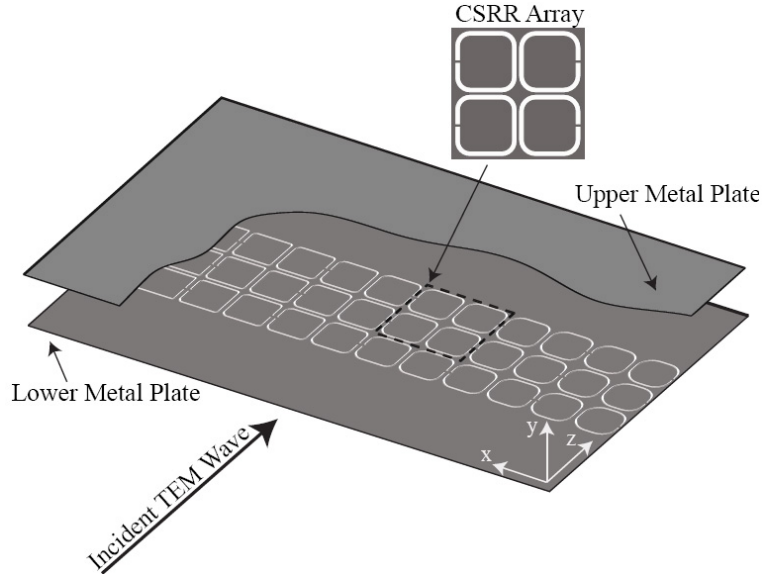


FIGURE 4.1: Configuration of waveguided metamaterials[58]

To characterize the waveguided metamaterials, the scattering (S-) parameters are simulated using Ansoft HFSS, a commercial full-wave electromagnetic solver whose accuracy has been previously verified [3, 47, 48]. The simulation configuration for the complimentary planar structure, however, differs from typical metamaterial unit cells. Fig.4.2(b) shows the simulation setup used to retrieve the effective constitutive parameters of a particular complementary waveguided metamaterial structure, for example, a CSRR here. The polarization of the incident TEM wave is constrained by the use of perfect magnetic conducting (PMC) boundaries on the sides of the computational domain. As example, the waveguide separation $h = 1mm$, while the vacuum region has a height of $d = 11mm$ with a perfect electric conducting (PEC)

boundary on the lower surface. Radiation boundaries are assigned below the ports, as shown in the Fig.4.2. The two ports are positioned far away from CSRR structure to avoid near field effect coupling between the ports and the CSRR. The phase shift accumulation along the regions just outside the CSRR unit cell is subtracted from the scattering parameters in the usual manner (i.e., de-embedding is performed). The retrieval result for the CSRR unit cell inside the planar waveguide is presented in Fig. 4.2(a).

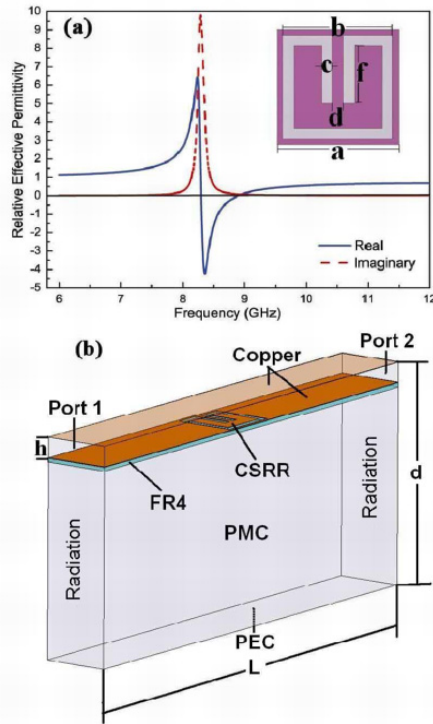


FIGURE 4.2: Retrieval results, dimensions of CSRRs and simulation setup. (a) Extracted permittivity and CSRRs' dimensions, in which, $a=3.333$ mm, $b=3$ mm, $c=d=0.3$ mm and $f=1.667$ mm. (b) Simulation configuration for CSRR unit cell. $d=11$ mm, $h=1$ mm and $L=23.333$ mm [63]

Once we achieve the effective constitutive parameters of the waveguided metamaterial structure, one can model the complementary structure as a volumetric media filled in the parallel waveguide, and thus can easily integrate metamaterials into the waveguide system. The design of each complementary structure provides the oppor-

tunity of controlling the local material's parameters. We will give several examples later to show the advantage of waveguided metamaterials.

4.2 Integrating metamaterials into waveguide

In the last section, we have discussed the concept, configuration and characterization method of waveguided metamaterials. We will further discuss the integration of metamaterials to waveguide environment and demonstrate several experiments that use different complementary structures and design in this section. As discussed, CSRR is an electrical resonator, while a CELC forms a magnetic resonator. We will make use of both structures in gradient index waveguided metamaterial and indefinite waveguided metamaterial design and experiment.

To discuss the CSRR structure, the approach to characterize the complementary structure has been described in details in the last section, where the retrieval process can be applied in the planar waveguide to extract the electromagnetic parameters. Typically CSRR behaves as an electric resonator, responding to the electric field penetrating across the milling-out complementary structure. Fig.4.3 shows the CSRR structure and retrieval permittivity and permeability in the planar waveguide using the commercial software Ansoft HFSS 10.0. The permittivity and permeability response in Fig.4.3 indicate that such type of waveguided metamaterials provide identical behavior as volumetric metamaterials including the frequency dispersion and spatial dispersion.[57]

The wave propagation yields only TE modes in the planar waveguide if the height of waveguide is less than half wavelength, resulting in the penetration of electric field through the complementary structures. Therefore, in the planar system, the effective permittivity can be flexibly achieved through the careful design of CSRRs. As an example, the effective wave impedance and refraction index of CSRR in terms of the radius of CSRR's corner, rr , are illustrated in Fig.4.4. Although one can manipulate

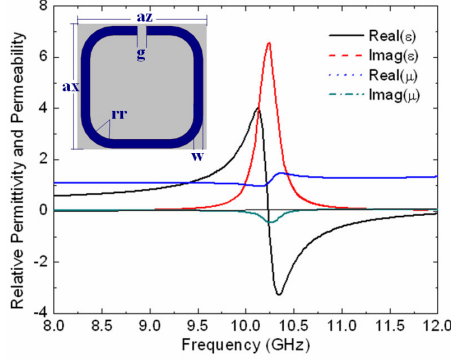


FIGURE 4.3: The CSRR structure and retrieval results, in which $rr=0.6$ mm, $w=0.25$ mm, $g=0.25$ mm, $l=3.2$ mm, $a_x=3.45$ mm, and $a_z=3.5$ mm. [58]

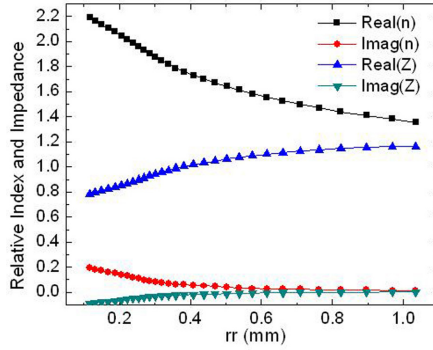


FIGURE 4.4: Relationship between the dimension rr in CSRR and its effective index and impedance. [58]

other geometrical dimension of the unit cell structure, we found it in simulation that the change of rr and usage of the frequency region right before the resonance can simultaneously achieve large index variation and good impedance matching condition ($Z = 1$).

To align all CSRRs together in the waveguide, we propose the configuration in Fig.4.1, in which the waveguide height is $h = 1$ mm. CSRRs are patterned on the lower metal plate, which is attached to a FR4 substrate with the thickness of 0.2026 mm. (Note that the substrate was cut by 0.1mm due to the milling-machine fabrication.) The relative permittivity and dielectric loss tangent of FR4 are 4.4 and 0.02, respectively. Similar to bulk metamaterials, the milling out CSRR structure

can form equivalent electromagnetic medium by providing the response inside the planar waveguide. Therefore, by use of 2D planar waveguided metamaterials, various designs based on the electromagnetic theory or gradient index optics can be implemented conveniently in planar circuits or waveguide systems.

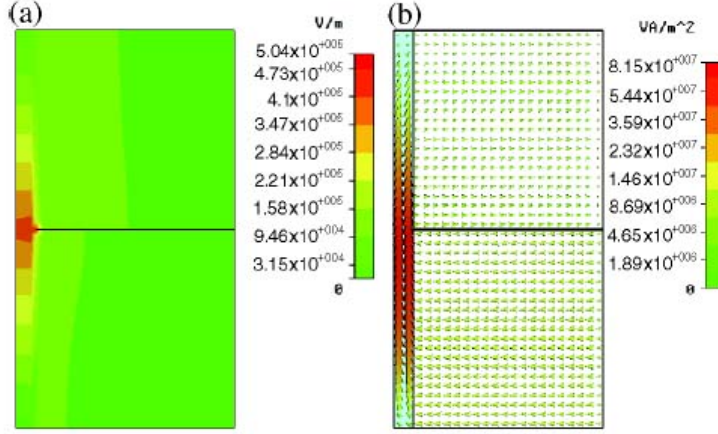


FIGURE 4.5: Experimental configuration[58]

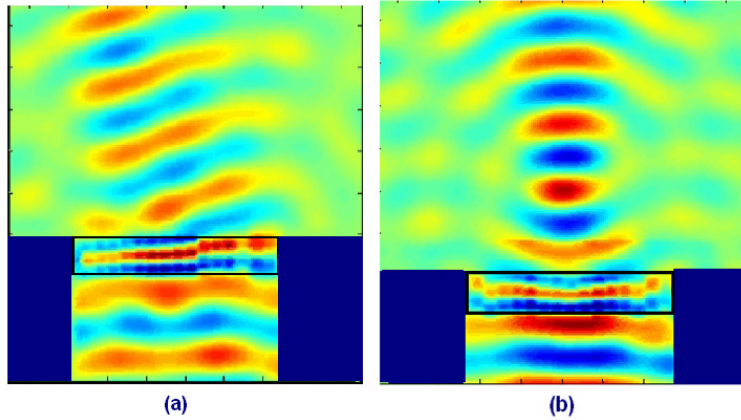


FIGURE 4.6: 2D field mapping for beam steering gradient index lens and focusing gradient index lens[58]

Hereby, we propose two distinct designs of gradient index media [20] – beam-steering and focusing slabs, respectively. To design the beam-steering slab, we use the procedure in Ref. [20] directly, giving the formula

$$\sin(\theta) = N_z a_z \Delta n / a_x \quad (4.1)$$

in which θ represents the beam steering angle, N_z gives the number of unit cells along the propagation direction, a_z and a_x are unit-cell separations along z and x axes, and Δn is the linear difference of relative refraction index between each two neighboring unit cells along the x axis. In our design, $N_z = 6$ and other parameters keep the same as the earlier description.

Given the wave deflection angle (10 degrees here) and the refraction index of the first CSRR, all refraction indexes along the x direction can be determined using Eq.4.1. Note that all CSRRs are the same along the z direction but linearly distributed in the x direction at the designed frequency of 9.5 GHz. We remark that the dependence of refraction index on the corner radius rr is extracted through parameter retrieval (with some discrete values of rr) and the subsequent data-fitting process. In the beam-steering design, the index range is from 1.3537 to 2.1929 with $\Delta n = 0.029$. That is to say, totally 30 CSRRs are used in the x direction.

To design the focusing slab, we apply gradient index optics to the distribution of refractive index along the x axis, which is expressed as

$$\Delta n_i = \frac{\sqrt{(i \cdot a_x)^2 + f^2} - f}{N_z \cdot a_z} \quad (4.2)$$

in which i is the sequence number of unit cell starting from the middle of the slab along the x axis, f gives the focal distance, and Δn_i represents the index difference between the i th unit cell and the middle unit cell. Once all unit-cell indexes are determined according to Eq.4.2, the implementation (unit-cell dimensions) can be then extracted from Fig.4.4. In our design, a six-layer ($N_z = 6$) focusing slab with 29 unit cells along the x direction is constructed. The refraction index varied from 1.7589 in the middle to 1.3537 on two ends, resulting in a 42 mm focal distance in simulation at 9.5 GHz. (Note that the direct calculation gives the focal distance of 90mm. However, due to the aberration and boundary effect of gradient index lens,

the simulated focal distant is 42mm. We did not show the simulated result to avoid redundancy.)

We demonstrate our designs by fabricating the samples and scanning the near-field distributions experimentally. To measure the waveguided metamaterials, we use a 2D near-field microwave scanning apparatus (2D mapper), which has been described in details in Ref. [12]. Fig.4.5 depicts the configuration of waveguided metamaterials measurement, in which, the upper metal plate of 2D mapper was not closed. To achieve a strong signal from source while not be reflected by the sample, we additionally place two metal ramps before and after the sample. The height between the sample and upper metal plate of 2D mapper was controlled to be 1 mm.

Fig.4.6(a) shows the mapping result of beam-steering sample at 9.5 GHz, in which the beam steering is clearly observed around 12 degrees, matching the theoretical design very well. Due to the careful control on impedance, the return loss is relatively lower than that of the traditional lenses. The difference in frequencies and deflection angles are due to the inaccuracy of fabrication, the height-control error, and the PCB substrate variation. Fig.4.6(b) illustrates the near-field mapping result of the focusing lens. The focal distance is 40 mm, which is very close to our design.

To produce another opportunity, one can employ the waveguided metamaterials to implement anisotropic media with magnetic resonances. For example, the dispersion relation for the TE wave in the indefinite medium can be written as [3]

$$\frac{k_x^2}{\mu_y} + \frac{k_y^2}{\mu_x} = \left(\frac{\omega}{c}\right)^2 \epsilon_z. \quad (4.3)$$

When $\mu_y < 0$, $\mu_z > 0$, and $\epsilon_x > 0$, it is obvious that the dispersion curve for Eq.4.3 is a hyperbola. In such a case, it can be easily shown that the phase velocity of the incident waves will undergo a positive refraction, while the group (or energy) velocity will undergo a negative refraction at the boundary of air and the indefinite medium,

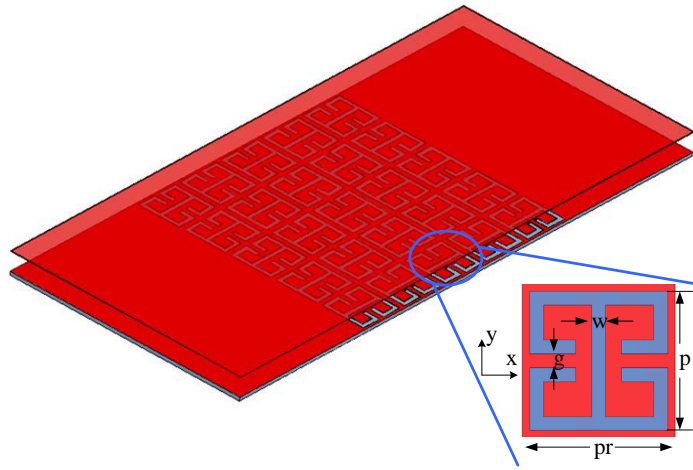


FIGURE 4.7: The CELC structure is chosen as the unit cell to realize the indefinite metamaterial.[59]

which will help to refocus the incident waves inside or outside the slab [18,19]. In Ref. [18,19], the authors have given the ray-tracing diagram for the waves emitted from a source in front of the indefinite slab, showing the occurrence of negative refraction at the interface between air and the indefinite medium, and also the existence of partial focusing for incident waves.

To integrate such anisotropic media into the waveguide, the CELC structure can be an option of the basic unit of the artificial indefinite medium, as illustrated in

Fig.4.7. The CELC structure refers to the planar-waveguide unit with the ELC patten etched on the bottom metallic plate. When the working frequency is selected to be lower than the cutoff frequency for the second-order mode (TE mode), only the dominant TEM mode could be supported in the waveguide. Then the corresponding electric field is just parallel to the axis of the CELC unit. From the Babinet's principle, the magnetic response may be produced under the excitation of the external electric field along the y direction.

We remark that the components of the permeability tensor in the x and y directions are different since the shape of the CELC unit is not identical in these two directions. Hence the effective medium composed of CELC particles are indefinite, which is suitable for realization of the partial focusing as mentioned earlier. As discussed, the CELC can form the equivalent indefinite slab. In order to get the effective permittivity and permeability of the CELC unit, we take the characterization approach and advanced retrieval algorithm described in Ref. [60].

To measure the indefinite waveguided metamaterial, we used the 2D near-field microwave scanning apparatus (2D mapper) for observation of the field distributions in the planar waveguide and within the CELC region. In Fig.4.8, we have shown the partial focusing sample, where the CELC patterns are formed from copper-clad FR4 circuit board with the thickness of 0.2 mm. The dimensions for the CELC unit shown in Fig.4.8 are selected as $pr = 3.333$ mm, $p = 3$ mm, and $w = g = 0.3$ mm, and the thickness of the copper layer is 0.018 mm.

In our design, the gap between the patterned circuit board and the top PEC plate of the waveguide is kept as 1 mm, and the sample is placed upon a cubic styrofoam. The CELC units are fabricated using the standard photolithography, and there are altogether 12 units in the longitudinal direction and 60 units in the transverse direction. There is a hole below the CELC patterns, as shown in Fig.4.8(b), where the excitation antenna could protrude into the waveguide after penetrating

the styrofoam.

Since the height of the 2D mapper is much larger than the gap in the CELC region, two metallic ramps are placed on each side of the sample in order to avoid the severe impedance mismatch due to the change of geometry. There are two copper regions beside the CELC patterns on the circuit board, which forms a planar waveguide together with the top PEC plate. A ring of microwave absorber with saw-toothed patten has been placed near the boundary of the 2D mapper so as to reduce the reflection of electromagnetic waves at the edge of plates.

We have to emphasize that we cannot obtain the right effective medium parameters when we directly make simulations for a single CELC unit, following the standard retrieval procedure. Actually the CELC structure shown in Fig.4.8 has very strong coupling among the adjacent units. Therefore, if we do not consider the coupling effect in our simulations, the final effective permittivity and permeability will significantly deviate from the correct values.

In our design, we have adapted the advanced parameter retrieval method, which is quite efficient for the resonant structures with strong coupling among the neighbors[52]. We need to make two different simulations to get the components of the permittivity and permeability tensors when the magnetic field of the TEM mode is along x and y directions, respectively, as shown in Fig.4.9. After the standard retrieval procedure, we obtain the effective permittivity and permeability curves for the two kinds of simulation setups shown in Figs.4.9(a) and (b). The effective ϵ_z and μ_x from Fig. 4.9(a) are plotted in Fig.4.10, while the effective ϵ_z and μ_y from Fig. 4.9(b) are demonstrated in Fig.4.11.

By comparing Fig.4.12 with Fig.4.13, we observe that the effective ϵ_z varies a lot in most of the frequency band in the two cases due to the particle response and the coupling between adjacent units. However, at our desired frequency, $f = 10.5$ GHz, both ϵ_z are quite close. In Fig.4.12(a), we have $\epsilon_z = 1.085 - i0.1123$; and in Fig.

4.13(a), we have $\epsilon_z = 1.047 - i0.1338$. Hence we can assume that at 11.5 GHz the effective permittivity in the z direction does not change for waves incident from x and y directions. Also we obtain from Figs.4.10 and 4.11 that $\mu_x = 2.489 + i0.193$ and $\mu_y = -0.970 + i0.122$ at 11.5 GHz.

We have made numerical simulations for the indefinite medium by using the software package HFSS at $f = 11.5$ GHz based on the extracted permittivity and permeability mentioned above. The distribution of electric field at a section of the planar waveguide is illustrated in Fig. 4.12. It is obvious that there exist several foci inside and outside the indefinite slab. The waves continue to propagate radially behind the focus on the right of the slab, just like the cylindrical waves radiated from a 2D point source. The corresponding experimental result for the electric field distribution at 11.5 GHz is shown in Fig.4.13, where the sign ‘X’ stands for the location of the excitation antenna, and the region between the two dashed lines are covered with the CELC structures. We can see that the experimental result has excellent agreement with the numerical simulation, and the partial focusing phenomenon is quite obvious.

In conclusion, we demonstrate both electrical and magnetic waveguided metamaterial structures, and both inhomogeneous and anisotropic medium designs in this section. The development on waveguided metamaterials prove the convenience of integrating gradient index metamaterial or novel anisotropic metamaterial into the waveguide system. We expect a potential application of such type of metamaterials in the RF waveguide environment in the future.

4.3 Electromagnetic tunneling experiment by waveguided metamaterials

In the last section, we have discussed the approach to integrate different type of waveguided metamaterials into the actual parallel waveguide system. Continuing on

the topic, we will further take the advantage of easy integration benefit of waveguided metamaterials and apply it to a novel electromagnetic tunnelling experiment, in which, a zero index metamaterial needs to be filled into an extremely narrow channel. As the channel is extremely subwavelength scale (1/100 wavelength), it is almost impossible to design a bulk metamaterial structure with zero refractive index at such dimension in reality. Therefore, the waveguided metamaterial configuration is of the advantage in this application. In this section, we will discuss the concept of electromagnetic tunnelling effect by zero index metamaterials, and then demonstrate the effect in experiment.

Recently another attention has focused on structures for which the real part of one or both of the constitutive parameters approaches zero. These structures have been developed to form interesting devices such as highly directive antennas [61] and compact resonators [62]. Most recently, Silveirinha and Engheta [63] have proposed that a material whose electric permittivity is near zero—or an epsilon near zero (ENZ) medium—can form the basis for a perfect coupler, coupling guided electromagnetic waves through a channel with arbitrary cross section.

Fig.4.14 indicates the configuration of electromagnetic tunneling through narrow channel by ENZ. Calculating the reflection coefficient through Maxwell's Equations, it can be expressed as [63]

$$R = \frac{a_1 - a_2 + ik_0\mu_{r,p}A_p}{a_1 + a_2 - ik_0\mu_{r,p}A_p} \quad (4.4)$$

Therefore, the one of tunnelling conditions is the identical cross-section $a_1 = a_2$. However, it is insufficient because the term of A_p can also cause significant reflection. To resolve this term, one solution is letting μ also tends to zero, reaching nihility medium, or making the channel A_p negligible small, that is, an extremely narrow channel. The later one is of much more interesting because only ENZ medium is

needed to tunnel the electromagnetic power through the extremely narrow channel. Fig.4.15 gives an example of EM waves tunneling through a U-turn narrow channel in simulation. Wire medium is used to perform an ENZ inside the channel at plasma frequency. Such tunneling effect in theory predicts the unfamiliar propagation properties. In the next section, the experimental demonstration will be described in the following section.

As discussed, instead of using bulk medium as usual, we made use of planar complementary split ring resonators (CSRRs) patterned in one of the ground planes of a planar waveguide to form the electromagnetic equivalent of an ENZ. The CSRR structure was proposed by Falcone *et al.* [57], who showed by use of the Babinet principle that the CSRR has an electric resonance that couples to an external electric field directed along the normal of the CSRR surface, as discussed before in last section. While, different from the 1D metamaterials by CSRR depicted by Falcone, we integrated CSRR into planar waveguide as a 2D problem, forming equivalent inserted medium environment inside waveguide. It was further shown explicitly that a volume bounded by a CSRR surface behaves identically to a volume containing a resonantly dispersive dielectric. The advantages of developing the new configuration are due to the ease of accurate design and fabrication in experiment and form narrow channel while avoiding the unnecessary height restriction by unit cell in bulk medium structure design. Although variants of the wire medium could also potentially be used to form the ENZ medium [42], the spatial dispersion and effects due to the finite wire length can cause significant complication [64]. To create the condition of electromagnetic tunneling, the geometry considered here to demonstrate the tunneling effect is chosen to be compatible with our planar waveguide experimental apparatus (Fig.4.16) previously described [63]. Three distinct waveguide sections are formed, distinguished by the differing gap heights between the upper and lower metal planes. There is a gap of 11 mm between the upper and lower conducting

plates that serve as the input and output waveguides. (For comparison, standard X-band waveguide, which covers the frequency region from 8-12 GHz, has a standard height of 10.16 mm.) The narrowed tunneling channel with patterned CSRRs in the lower surface has a gap of 1 mm between the plates. The planar waveguide is bounded on either side by layers of absorbing material, which approximate magnetic boundary conditions and also reduce reflection at the periphery. The waveguide and channel thus support waves that are nearly transverse electromagnetic (TEM) in character. Assuming the CSRR region can be treated as a homogenized medium, the entire configuration is well approximated as two-dimensional, with the average field distribution having little variation along the width.[60]

The characteristic wave impedances corresponding to TEM waves in the three waveguide regions are equivalent, equal to Z_1 . There is generally, however, a severe impedance mismatch at the two interfaces between the planar waveguides and the narrow channel, resulting in a large input impedance mismatch that inhibits the transmission of waves from the left waveguide region to the right. An effective impedance model for the specific geometry considered here has been described in detail in [65], where a transmission line model is derived showing that the narrow waveguide region can be replaced by a region having an impedance $Z_2 = (d/b)Z_1$. d/b is the ratio of the planar waveguide and channel heights. In addition, there is a shunt admittance $Y = jB$ at the interface between the mismatched waveguides, which becomes quite large (and therefore unimportant) when the waveguides differ significantly in height. Because $Z_2 \ll Z_1$, there is no coupling between the input and output waveguides, except possibly when a resonance condition is met and a Fabry-Perot oscillation occurs. If the channel is now loaded with an ENZ material, the effective wave impedance of the channel region is raised to the point where the three waveguide regions are matched and perfect transmission once again should occur. [60]

The experimental configuration studied here corresponds to one of the two cases considered by Silveirinha and Engheta [63]. In the first case ϵ and μ tend to zero simultaneously, while in the second ϵ is near zero and the area of channel is assumed electrically small. Our experimental setup belongs to the latter case, whose mechanism is illustrated by calculating the reflectance based on the simplified model described in [66]. We find

$$R = \frac{R_{12}(1 - e^{i2k_{2z}d})}{1 - R_{12}^2 e^{i2k_{2z}d}} \quad (4.5)$$

in which $R_{12} = (Z_2/(-iB) - Z_1)/(Z_2/(-iB) + Z_1)$ and $Z_2/(-iB) = (-iBZ_2)/(-iB + Z_2)$. R_{12} is the reflection coefficient between the planar waveguide and the channel, d is the effective length of the channel, and k_{2z} is the wave vector inside the channel. Z_1 and Z_2 are the effective input wave impedances outside and inside the narrow channel, respectively, whose ratio Z_1/Z_2 corresponds to the height ratio 11/1 in the absence of the patterned CSRRs. When ϵ and μ are simultaneously near zero, the characteristic impedance of the zero index material may take on the finite value $\lim_{\epsilon, \mu \rightarrow 0} \sqrt{\mu/\epsilon}$, which may differ from the impedance of adjacent regions. However, since $k \rightarrow 0$, the reflection coefficient vanishes, indicating the tunneling of the wave across the channel [63]. In the present configuration, since Z_2/Z_1 approaches zero, the reflection coefficient no longer vanishes in a simple manner. Instead, when the ENZ medium possesses a small but finite value of permittivity, Z_2/Z_1 may approach unity, and the tunneling effect is restored. [60]

The equivalence between an ENZ metamaterial and the CSRR structure shown in Fig.4.2 can be established by performing a numerical retrieval of the effective constitutive parameters for the channel. The simulated reflection and transmission coefficients as a function of frequency for the channel with and without the ENZ metamaterial are shown in Fig.4.17. These results are compared with the simplified

model presented in Eq.4.5, where $Z_2 = Z_1/(11\sqrt{\epsilon_{eff,r}})$ with the effective length d chosen as $13mm$. An approximate analytical expression for B obtained by a conformal mapping procedure is presented in [66]. The influence of the junction susceptance B is minimal for the geometry considered here, though we have retained it for completeness. The transmission and reflection coefficients predicted by the analytical model are plotted in Fig.4, where they can be seen to be in very good agreement with those simulated, supporting the interpretation of the transmission peak as an indication of tunneling. In addition, Fig.4.18(a) shows the Poynting vector distribution at 8.8 GHz, revealing the squeezing of the waves through the narrow channel.[60]

To validate experimentally the ENZ properties of the CSRR region, a channel patterned with CSRRs was fabricated and its scattering compared to an unpatterned control channel. Both the CSRR and control channels were formed from copper-clad FR4 circuit board (0.2 mm thick), fabricated with dimensions $18.6 \times 200(mm^2)$ (shown in Fig. 4.16). The array of CSRR elements (shown in Fig. 4.2) was patterned on the circuit board using standard photolithography. A total of 200 CSRRs (5 in the propagation direction, 40 in the transverse direction) were used to form the effective ENZ metamaterial. The CSRR/control substrates were then placed on a styrofoam support, with dimensions $18.6 \times 10 \times 200(mm^3)$. Copper tape was used to cover the sides of the Styrofoam and carefully placed to ensure that the copper-clad substrates would make good electrical contact with the bottom plate of the waveguide. X-band waveguide-to-coaxial adapters were used to connect the waveguide to a vector network analyzer (VNA, Agilent) using standard SMA cables.[60]

To obtain a base level of transmission, the control sample was positioned inside the planar waveguide halfway between the two ports and a transmission measurement taken. The results are shown in Fig.4.19 and compared with both the analytical model and the HFSS simulation. The pass band of the control slab, due to the res-

onance condition, was found to occur at 7 GHz—shifted from the pass band found in simulation. The consistent shift between measurement and simulation likely reflects the differences between the experimental environment and the simulation model (e.g., finite slab width and fluctuation of channel height). The measurement and simulation, however, are in excellent qualitative agreement. By uniformly shifting the frequency scale, the measured and simulated curves are almost identical (**note the two scales indicated on the top and bottom axes**).[60]

With the control slab replaced by the CSRR channel, the measured transmitted power (shown in Fig.4.19) reveals a pass band near 7.9 GHz (8.8 GHz from the simulation), which is identical with retrieval prediction. This pass band is absent when the control slab is present, demonstrating that electromagnetic tunneling takes place at approximately the frequency where the effective permittivity of the ENZ region approaches zero.[60]

To add further support that the observed pass band is due to the predicted tunneling phenomenon where $\epsilon \approx 0$, phase sensitive maps of the spatial electric field distribution throughout the channel region were constructed[51]. The electric field magnitude was mapped inside a 180×180 (mm^2) square region for both the copper control and CSRR channels. Fig.4.20. shows the mapped fields for both configurations taken at 8.04 GHz (where the effective permittivity of the CSRR structure is approximately zero). The field is normalized by the average field strength, which makes the color scale different. Yet it is clear that the CSRR channel allows transmission of energy to the second port, measured to be $-5dB$, whereas only $-14dB$ of field energy propagates to port 2 when the control slab is presented. Note the uniform phase variation across the channel at the tunneling frequency, $f = 8.04$ GHz.[60]

A linear plot of phase versus position (shown in Fig.4.21) further illustrates the tunneling of energy through the ENZ channel versus the Fabry-Perot like resonant

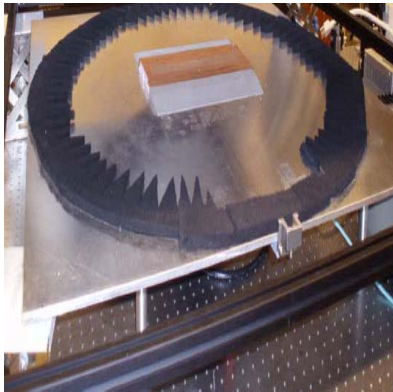
scattering. The latter mechanism of transmission has been studied in detail by Hibbins et al.[66]. As can be seen in Fig.4.21, a strong phase variation exists across the control channel at $f = 7$ GHz, corresponding to the pass band that is seen in Fig.4.19. The clearly distinguished phase advance within the channel implies that the propagation constant is non-zero. The large transmittance results from a resonance condition related to the length of the channel. By contrast, the spatial phase variation for the CSRR channel is shown in Fig.4.21 for $f = 8.04$ GHz (the pass band of the CSRR loaded channel), where we see that the phase advance across the channel at this frequency is negligible. The nearly zero phase variation is consistent with the conclusion that ε_{eff} for the CSRR slab is very close to zero.[60]

While the CSRR waveguide used in these experiments does not form a volumetric metamaterial, we have nevertheless shown that the planar waveguide channel can be treated equivalently as having a well-defined resonant permittivity, with zero value at a frequency of 8.04 GHz. Furthermore, the set of transmission and mapping measurements we have presented demonstrates that the tunneling observed through the channel is consistent with the behavior of an ϵ -near-zero medium. The measurements confirm that “squeezed waves” will tunnel without phase shift through extremely narrow ENZ channels. ENZ materials may thus be used as highly efficient couplers with broad application in microwave and THz devices.[60]

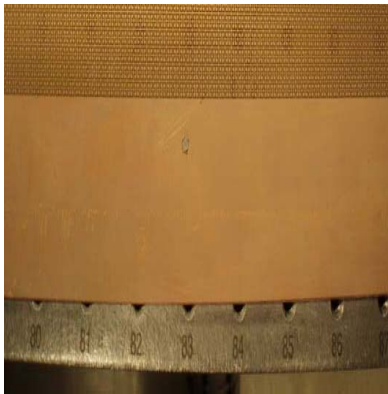
As we have successfully demonstrated the electromagnetic tunnelling effect via waveguided metamaterials in the parallel waveguide system, we can move forward to integrate the tunnelling technology and waveguided metamaterials into a RF circuit.[67] The construction of this tunnelling circuit has shown in Fig.4.22. A multi-layer PCB fabrication is used and an array of via hole performs the junction of the tunnelling experiment. An array of designed CSRR was milled out at the ground layer. Thus, we can integrate all the components of the tunnelling experiment into a complete RF circuit. The similar analysis and measurement can be done, shown

in Fig.4.23, in which, a clear tunnelling transmission peak can be observed. To take the advantage of this effect in a sharp bending environment, we designed and fabricated another circuit shown in Fig.4.24, in which, a 180 degree sharp bend connects two transmission line. At the sharp bending region, we employ the tunnelling construction with via hole and CSRR structure. By measuring the circuit, we showed the reflection and transmission on both control and tunnelling circuit in Fig.4.25. The measurement indicates that the transmission is about $-20dB$ without CSRR structures, but can be improved to $-4dB$ by placing CSRR on the ground. The improvement on the coupling efficiency and the application of waveguided metamaterials in the RF circuit have been developed and verified, although there is still a certain loss in the transmission. The imperfection might be caused by the fabrication error in multi-layer PCB and the loss in the substrate. Whereas the configuration of the related technology has been demonstrated and we expect to see the wide potential applications on such 2D waveguided metamaterials in the near future.

Some of the work here have been published in Physical Review Letters[60], Applied Physics Letters[58, 67] and Physical Review B[59].



(a)



(b)

FIGURE 4.8: (a) The experimental setup for the partial focusing. (b) Details of the fabricated CELC[59]

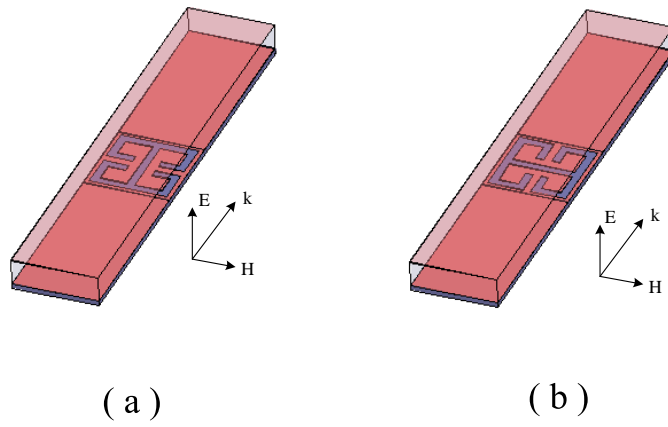


FIGURE 4.9: Simulation setups for the the anisotropic CELC unit when the plane waves are incident from two directions.[59]

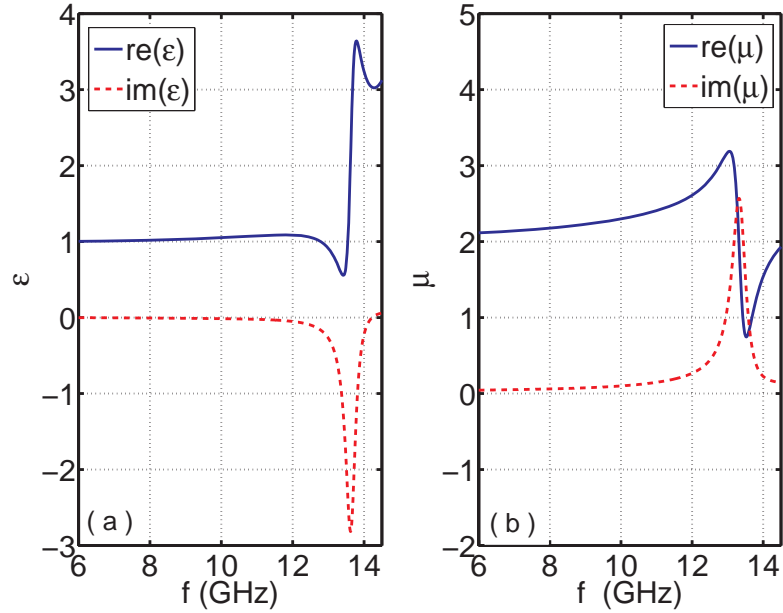


FIGURE 4.10: The effective permittivity and permeability curves for the simulation setup in Fig. 4(a). (a) ϵ_z . (b) μ_x . [59]

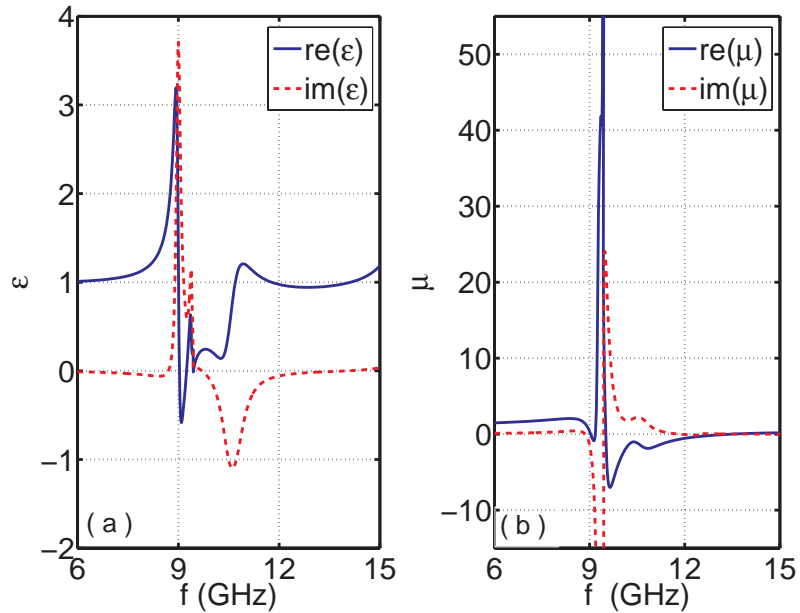


FIGURE 4.11: The effective permittivity and permeability curves for the simulation setup in Fig. 4(b). (a) ϵ_z . (b) μ_y . [59]

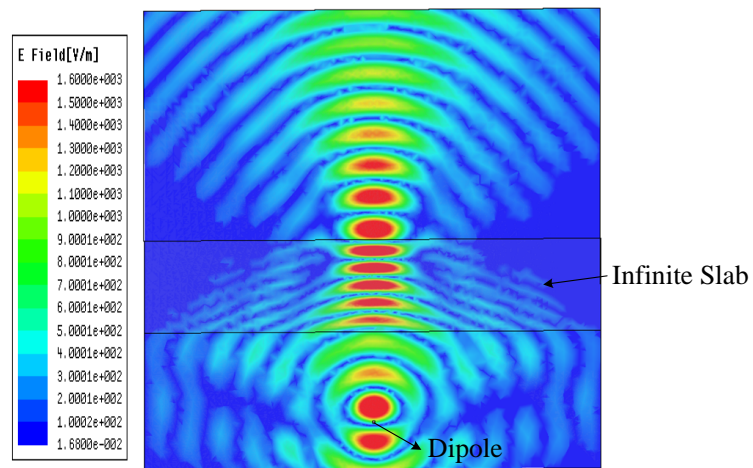


FIGURE 4.12: The distribution of simulated electric fields in a section of the planar waveguide at 11.5 GHz.[59]

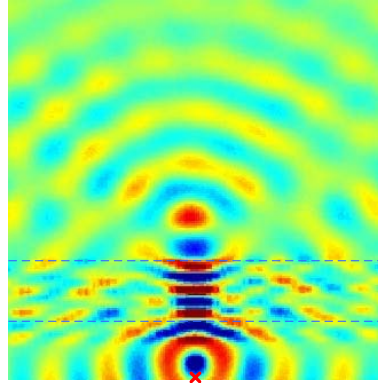


FIGURE 4.13: The experimental result for the electric-field distributions inside the 2D mapper at 11.5 GHz.[59]

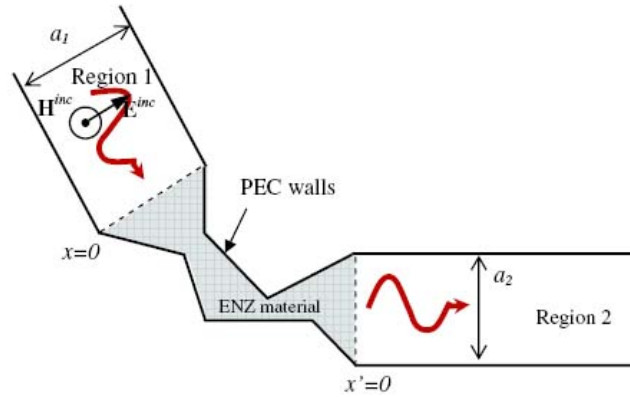


FIGURE 4.14: Figure from Ref.[63], the configuration of electromagnetic waves' tunnelling through narrow channel

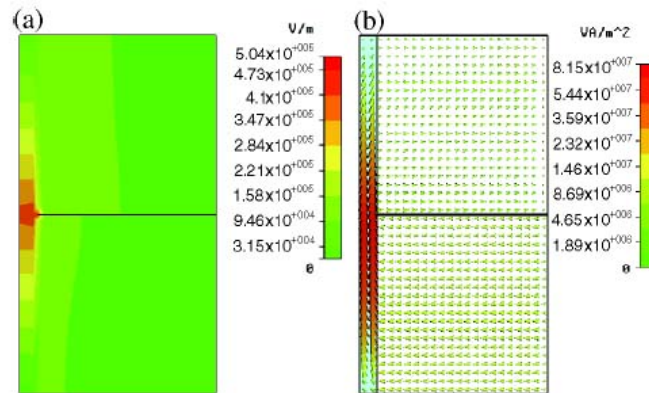


FIGURE 4.15: Figure from Ref.[63], electromagnetic wave tunnel through a narrow channel as U-turn

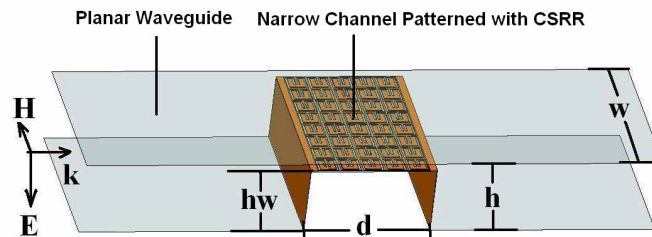


FIGURE 4.16: Experimental setup, in which $h=11$ mm, $hw=10$ mm, $d=18.6$ mm (16.6 mm for CSRR Regime), $w=200$ mm. Lower figure is the sample inside chamber. [60]

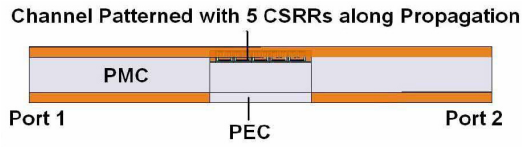


FIGURE 4.17: Configuration of tunneling effect simulation[60]

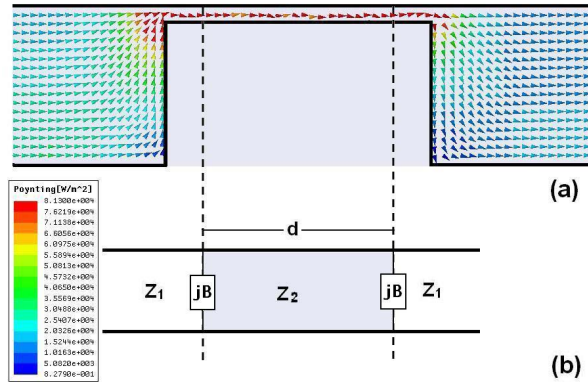


FIGURE 4.18: Poynting vector and medium model (a) Poynting vector (b) Simplified Model[60]

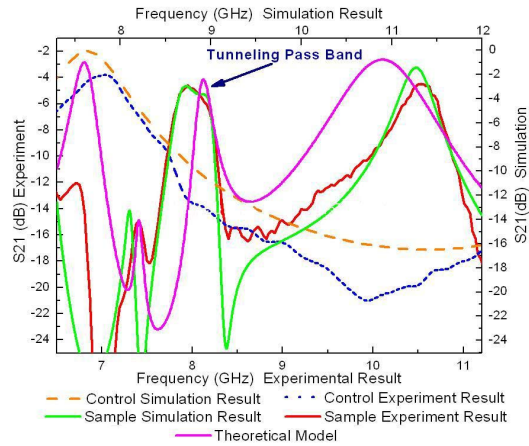


FIGURE 4.19: Experimental, theoretical and simulated transmissions for the tunneling and control samples. [60]

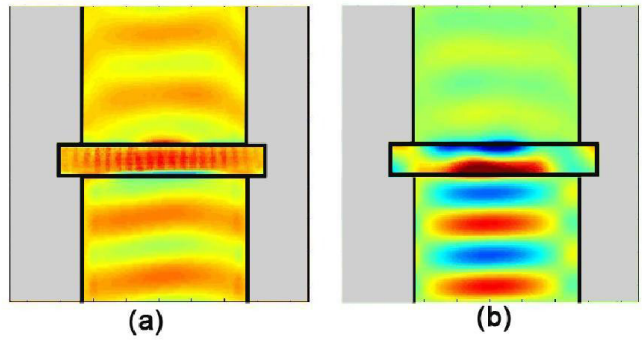


FIGURE 4.20: 2-D Mapper results at 8.04 GHz. (a) Field distribution of tunneling sample (b) Field distribution of control[60]

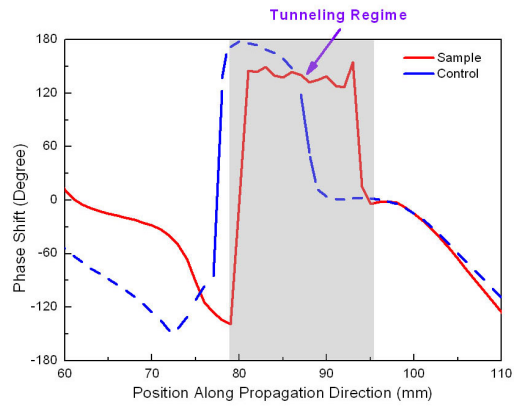


FIGURE 4.21: Phase Shift for 5 unit-cell tunneling sample at 8.04 GHz and control at 7 GHz.[60]

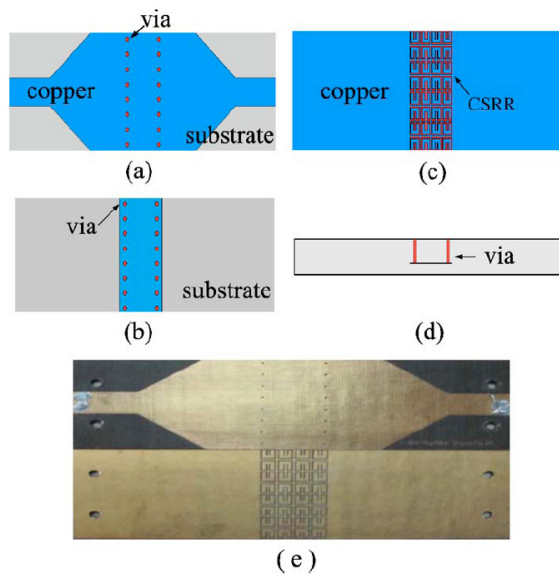


FIGURE 4.22: The circuit tunneling structure. (a) Top layer. (b) Middle layer. (c) Bottom layer. (d) Side view. (e) Top and bottom views of the fabricated circuit.[67]

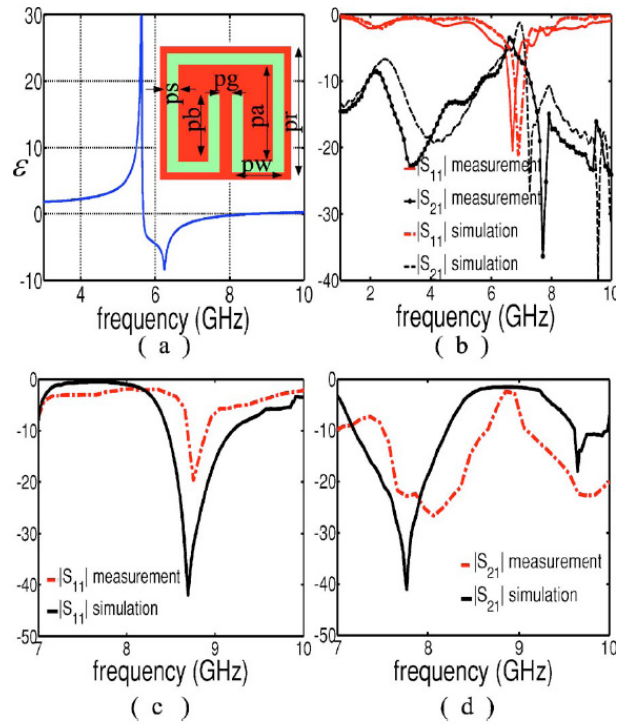


FIGURE 4.23: (a) The effective permittivity for CSRR (inset: the CSRR structure). (b) The measured and simulated S parameters for the tunneling structure shown in Fig.4.22 without any patterns on the bottom metallic layer. (c) The measured and simulated reflection coefficients S_{11} for the tunneling structure shown in Fig.4.22. (d) The measured and simulated transmission coefficients S_{21} for the tunneling structure shown in Fig.4.22.[67]

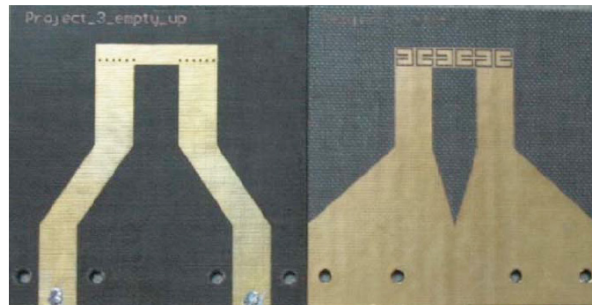


FIGURE 4.24: A circuit bend using the tunneling structure. Left: top view. Right: bottom view[67]

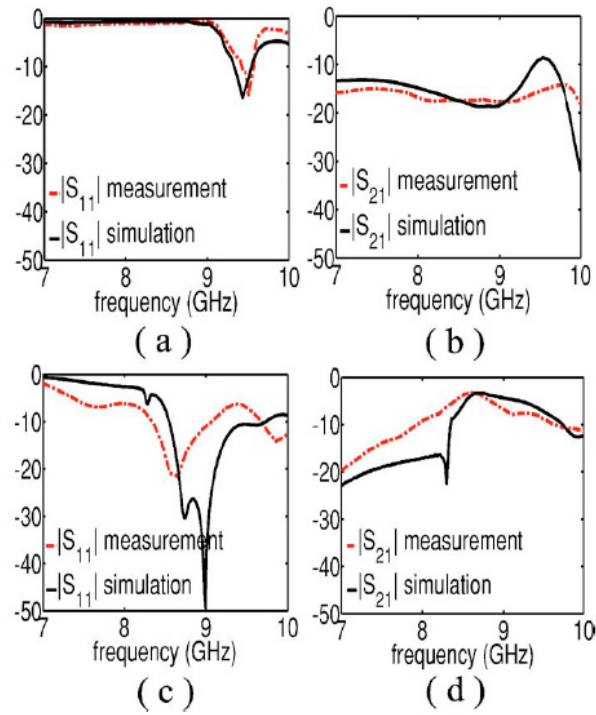


FIGURE 4.25: The measured and simulated S parameters for the circuit bend shown in Fig.4.24 with/without CSRR patterns on the bottom. (a) S_{11} without CSRR patterns. (b) S_{21} without CSRR patterns. (c) S_{11} with CSRR patterns. (d) S_{21} with CSRR patterns.[67]

Experiment on gradient index metamaterials

5.1 Concept of gradient index metamaterials

We have discussed the waveguided metamaterials in the last chapter and demonstrated several experiments using such type of metamaterials including the experiment on gradient index metamaterials. In this chapter, we will in details discuss the general gradient index metamaterials and show more demonstrations on different type of bulk gradient index metamaterials that contain different functionalities.

As discussed, the properties of a metamaterial can be manipulated by altering the characteristics of the circuit, such as its physical shape, dimension or local dielectric environment. Thus, the design of particular metamaterial structure can define the local material properties and the medium formed is unnecessary to be homogeneous. By relaxing the periodicity restriction on the complex media construction from metamaterials, a gradient index metamaterial can be constructed in a general sense. Such media is formed from non-identical unit cells rather than identical unit cells, enabling exotic microwave or optical behaviors.

A consequent problem is how a local material's parameter can be determined

by the standard retrieval process, where the periodic boundary condition has been used and only a single layer of unit cells along the propagation direction has been considered. According to the effective medium properties of metamaterials described in chapter two, we have the knowledge that finite metamaterial structure has strong spatial dispersion effect and can be coupled by its neighbor scatter. The spatial dispersion effect has been considered in the standard retrieval process and the same property can be remained in the gradient index metamaterials. However, the coupling between neighbor unit cells are unavoidably varied from standard retrieval process to the gradient index environment. This approximation might lead to the discrepancy between the design and actual performance on this type of complex scatter system. Whereas in most gradient index metamaterial design, the refractive index varies smoothly and slowly with spatial coordinate. This suggests that the neighbor unit cell structures are resembled to each other and are of a slight change in geometry dimension. The coupling between the unit cells in such gradient index environment can thus be closed enough to the standard retrieval process. In addition the function of metamaterial unit cell is to provide the local dipole moment response to the applied field and can be insensitive to the macroscopic environment in general. This justification of the design on gradient index metamaterials indicates both the challenge and opportunity of metamaterials. The approximation might lead to inaccurate design and is difficult to control because the errors varies with the practical design environment, resulting in the tricky design process. To the other hand, this approximation can decouple the designs between system level and particle level. The computation burden of such complex scatter system is effectively reduced by predicting material's local parameters by simulating the individual unit cell structure. The possibility of designing a large scale scatter system enables the novel approach to manipulate electromagnetic waves.

The early gradient index (GRIN) metamaterial was proposed and demonstrated

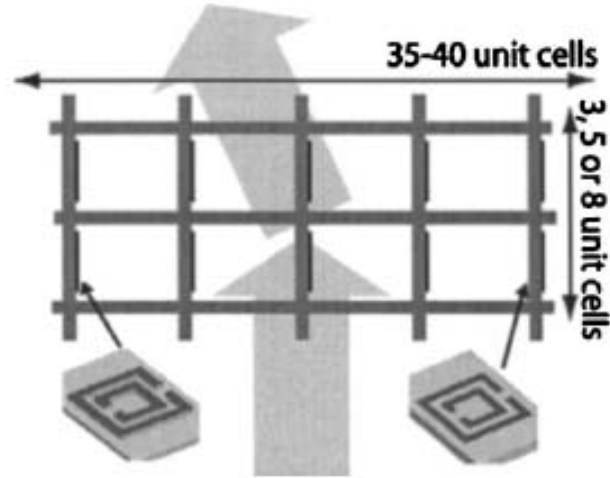


FIGURE 5.1: From Ref.[18]. The design of gradient index metamaterials by placing inhomogeneous SRRs transverse to propagation direction

in [20, 58], in which split ring resonators (SRRs) were chosen as the resonant circuits, forming a bulk inhomogeneous medium. Though this structure was demonstrated in a planar waveguide apparatus, metamaterials formed from SRRs are the conceptual equivalent of analog of naturally occurring materials, shown in Fig.5.1. The system level design of gradient index metamaterials, thus, differs from case by case. We have already discussed the examples of the beam steering gradient index design and beam focusing gradient index design in waveguided metamaterial experiment in chapter four. We will continue to discuss different gradient index design with different type of metamaterial structure in the later sections.

5.2 Gradient index lens by ELC structures

In the last section, we discussed the basic concept of gradient index metamaterials and justified the design process and approximation on such type of metamaterials. Several related experiments have also discussed in chapter four within the waveguide environment. In this chapter, we will discuss a bulk gradient index metamaterial because different potential applications might be targeted by manipulating the waves

in free space. As we also understand the design process in general on a gradient index metamaterial, we will start from the metamaterial structure level to discuss the opportunities of building bulk gradient index metamaterial lens.

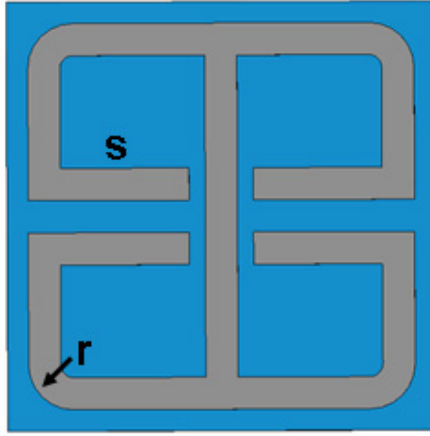


FIGURE 5.2: An ELC structure that has electric resonance. The change of geometry parameter s and r can lead to varies on the quantity of the response.

According to the gradient index metamaterial design, an inhomogeneous media can be formed by various metamaterial structures. We can thus control the local material's permittivity and permeability across the spatial coordinate. To achieve a gradient refractive index, one can either manipulate the magnetic response or electric response within the media. However, the impedance of the media might vary differently by magnetic medium and electric medium. Meanwhile the spatial dispersion will in general distort the Drude-Lorentz resonance and cause the anti-resonance to the other parameters regardless the type of metamaterial structure. It complicates the accurate design of gradient index metamaterial lens as one has to investigate permittivity and permeability at the same time. To the other hand, if we think more about the gradient index metamaterial lens design in material's level, a control of impedance is actually request to match that in the free space. Therefore, to appropriately design a gradient index metamaterial device, we need to control the refractive index to manipulate the waves propagating through the media and

control the impedance to minimize the reflection at the surface of the gradient index materials.

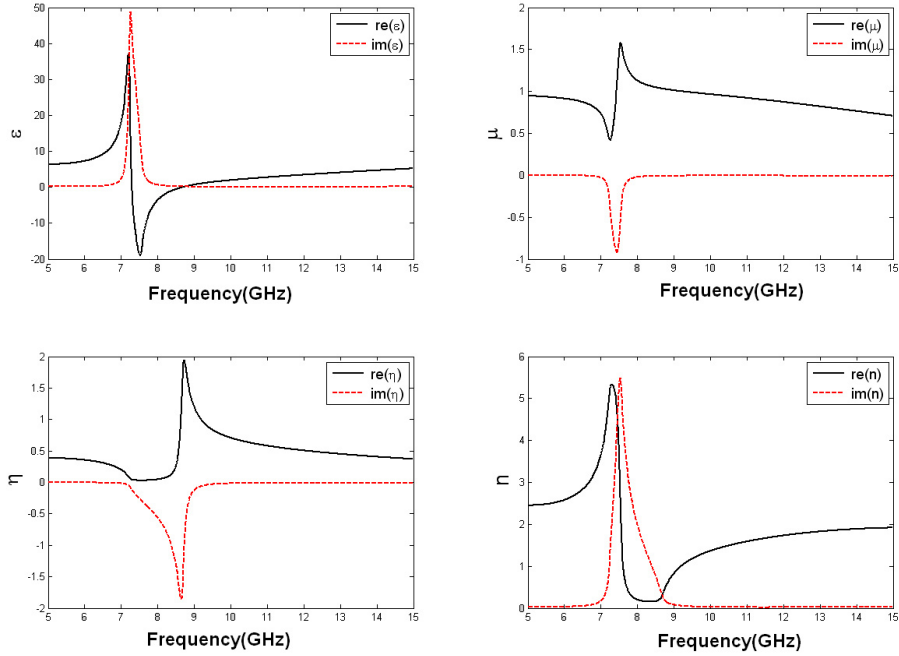


FIGURE 5.3: The effective electromagnetic parameters of an ELC structure with the periodicity 3.333mm and $s=0.835\text{mm}$ and $r=0.28\text{mm}$

To address the multi-restrictions on the gradient index metamaterial design, we investigated an electric-LC (ELC) structure [46] and modified it into a present form shown in Fig.5.2. The reason of introducing to arms is to increase the capacitance and lower down the resonant frequency. According to Fig.5.2, the equivalent capacitances can be largely affected by the geometry parameter s and the equivalent inductance and coupling between neighbor unit cell structure can be affected by the geometry parameter r . Fig.5.3 displays the effective electromagnetic parameters extracted from the standard retrieval process to such ELC structure. We observe both electric resonance and anti-resonance on magnetic response. If the geometry parameters s and r is changed, the response of the structure dramatically varies, as shown in Fig.5.4, though it is still an electric resonance with magnetic anti-resonance.

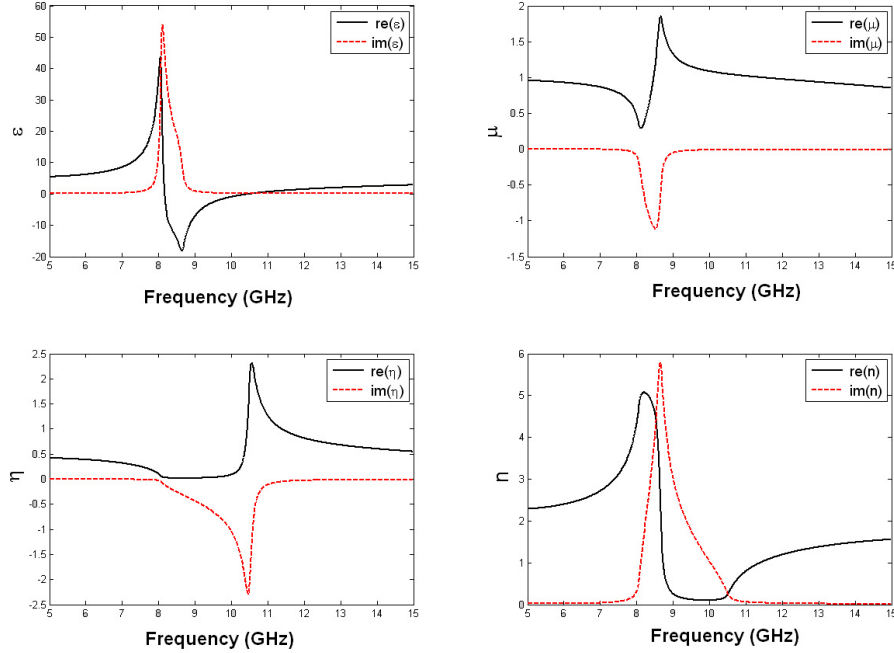


FIGURE 5.4: The effective electromagnetic parameters of an ELC structure with the periodicity 3.333mm and $s=0.32\text{mm}$ and $r=0.43\text{mm}$

Therefore, the design of s and r can both affect refractive index and impedance and be crucial in the gradient index metamaterial design.

The complexity of choosing appropriate s and r dimensions for different structures in the gradient index media and the spatial dispersion effect on all the designing structures make the gradient index design obscure and difficult. Therefore, to maximize the advantage of such flexibility on the particle response, we employ the rapid design technology discussed in chapter three and establish the optimization on the particular ELC gradient index metamaterial design. To design a beam steering modulation device, we need a linear gradient refractive index and an impedance matching to the air as much as possible. By setting these two criterions to the optimization scheme, we can achieve the Table 5.1, indicating the best solutions found in the given structure topology.

According to the Table 5.1, we can take use of 31 unique ELC structures to

num	s	r	Refractive index design	Refractive index achieved		Impedance achieved	
1	0.46	0.185	0.4500	0.45265609+i*	0.15351869	2.04346304+i*	-0.71437558
2	0.47	0.25	0.4833	0.48573530+i*	0.14076321	1.95711340+i*	-0.58681994
3	0.47	0.165	0.5167	0.51980225+i*	0.13077278	1.86225163+i*	-0.48684706
4	0.48	0.22	0.5500	0.55283611+i*	0.12073979	1.77494054+i*	-0.40467315
5	0.49	0.27	0.5833	0.58593270+i*	0.11198497	1.69050702+i*	-0.33898102
6	0.495	0.24	0.6167	0.61981563+i*	0.10447469	1.60825389+i*	-0.28598112
7	0.505	0.28	0.6500	0.65221218+i*	0.09752461	1.53507282+i*	-0.24353666
8	0.52	0.38	0.6833	0.68565493+i*	0.09095663	1.46462033+i*	-0.20747269
9	0.525	0.33	0.7167	0.71979149+i*	0.08512595	1.39746876+i*	-0.17766973
10	0.535	0.345	0.7500	0.75321226+i*	0.07977319	1.33654135+i*	-0.15326100
11	0.545	0.355	0.7833	0.78593545+i*	0.07493314	1.28103460+i*	-0.13321778
12	0.56	0.42	0.8167	0.81985085+i*	0.07019523	1.22756056+i*	-0.11559967
13	0.575	0.475	0.8500	0.85332619+i*	0.06591324	1.17838339+i*	-0.10099451
14	0.595	0.575	0.8833	0.88663736+i*	0.06203490	1.13273891+i*	-0.08880241
15	0.6	0.495	0.9167	0.91993405+i*	0.05815487	1.08994984+i*	-0.07787068
16	0.605	0.4	0.9500	0.95259741+i*	0.05480806	1.05056430+i*	-0.06890910
17	0.625	0.48	0.9833	0.98631255+i*	0.05131998	1.01257086+i*	-0.06073553
18	0.635	0.46	1.0167	1.01341518+i*	0.04877895	0.98363020+i*	-0.05504006
19	0.655	0.515	1.0500	1.04717738+i*	0.04566940	0.94957232+i*	-0.04872399
20	0.67	0.505	1.0833	1.08000200+i*	0.04287145	0.91828992+i*	-0.04337158
21	0.69	0.535	1.1167	1.11349827+i*	0.04011057	0.88815361+i*	-0.03854875
22	0.705	0.5	1.1500	1.14674823+i*	0.03760279	0.85979910+i*	-0.03436735
23	0.725	0.505	1.1833	1.18017576+i*	0.03514621	0.83280952+i*	-0.03062118
24	0.75	0.545	1.2167	1.21372937+i*	0.03272695	0.80711970+i*	-0.02724684
25	0.775	0.57	1.2500	1.24674155+i*	0.03048831	0.78307618+i*	-0.02430191
26	0.805	0.615	1.2833	1.28029151+i*	0.02829200	0.75981661+i*	-0.02161508
27	0.83	0.605	1.3167	1.31345893+i*	0.02631927	0.73785898+i*	-0.01926231
28	0.875	0.705	1.3500	1.34670355+i*	0.02429084	0.71688509+i*	-0.01708684
29	0.91	0.715	1.3833	1.38005691+i*	0.02252371	0.69671321+i*	-0.01515837
30	0.93	0.635	1.4167	1.41334258+i*	0.02097637	0.67741027+i*	-0.01346132
31	0.98	0.68	1.4500	1.44672796+i*	0.01946269	0.65886231+i*	-0.01186258

Table 5.1: An optimized solution on the beam steering gradient index design from rapid design system

generate a linear gradient index from 0.45 to 1.45. Assuming the illumination is a gaussian collimated beam, the beam will penetrate through the central part of the lens, where impedance is well controlled to be closed to 1. By applying the optimized solution in Table 5.1, we fabricated an ELC gradient index metamaterial lens with 6 layers and measured the sample in the 2D near field scanning apparatus. Fig.5.5 displays the field mapping at 10Ghz in the experiment on the ELC gradient index lens. An expected beam steering effect was observed from the field mapping and verified the design of a gradient index metamaterial.

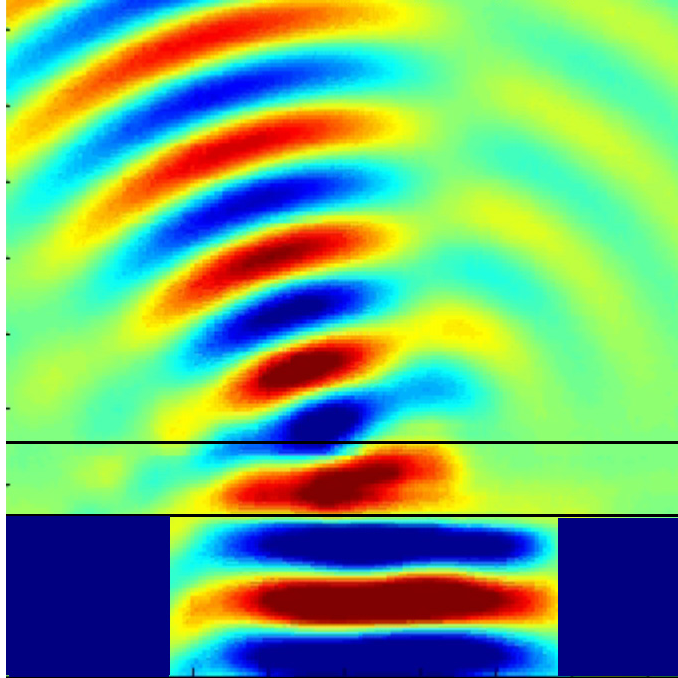


FIGURE 5.5: A field mapping in experiment on the ELC gradient index lens

5.3 Broadband gradient index metamaterials and complex lens design

In the last section, we discussed in detail the design of a bulk gradient index metamaterials by ELC structures. However, the loss and bandwidth of such design still remain the challenges. In this section, we will continue working on the gradient index metamaterials but focusing on the bandwidth and loss of metamaterial design. To address this challenges, we recall the development of artificial dielectric materials that can be constructed by conducting scatter systems and have been existed for a long time[68, 69, 70, 71, 72, 73, 74, 75, 76]. However, the design methodology of artificial dielectric materials was limited by the computational ability at early time, and thus prohibiting the further development of such complex scattering systems. Recently the electromagnetic response of metamaterial elements can be precisely controlled so that they can be viewed as the fundamental building blocks for a wide range of complex, electromagnetic media[24, 77, 78]. To date, metamaterials have commonly

been formed from resonant conducting circuits, whose dimensions and spacing are much less than the wavelength of operation. As discussed, an inhomogeneous media, in which the material properties vary in a controlled manner throughout space, also can be used to develop optical components, and are an extremely good match for implementation by metamaterials. The waveguided metamaterials and bulk gradient index metamaterials have already demonstrated the unprecedented freedom to control the constitutive tensor elements independently, point-by-point throughout a region of space. Whereas although metamaterials have proven successful in the realization of unusual electromagnetic response, the structures demonstrated are often of only marginal utility in practical applications due to the large losses that are inherent to the resonant elements most typically used. The situation can be illustrated using the curves presented in Fig.5.6, in which the effective constitutive parameters are shown in Fig.5.6 (a) and (b) for the metamaterial unit cell in the inset. According to the effective medium theory described in Ref.[19], the retrieved curves are significantly affected by spatial dispersion effect. To remove the spatial dispersion factor, we can apply the formulas in the theorem [7] and achieve that

$$\bar{\epsilon} = \epsilon \sin(\theta) / \theta \quad (5.1)$$

$$\bar{\mu} = \mu \sin(\theta) / \theta \quad (5.2)$$

in which, $\theta = \omega p \sqrt{\epsilon \mu}$ and p is the periodicity of the unit cell.

Note that the unit cell possesses a resonance in the permittivity at a frequency near 42 GHz. In addition to the resonance in the permittivity, there is also structure in the magnetic permeability. These artifacts are phenomena related to spatial dispersion-an effect due to the finite size of the unit cell with respect to the wavelengths. As previously pointed out, the effects of spatial dispersion are simply described analytically, and can thus be removed to reveal a relatively uncomplicated

Drude-Lorentz type oscillator characterized by only a few parameters. The observed resonance takes the form

$$\epsilon(\omega) = 1 - \frac{\omega_p^2}{\omega^2 - \omega_0^2 + i\Gamma\omega} = \frac{\omega^2 - \omega_0^2 - \omega_p^2 - i\Gamma\omega}{\omega^2 - \omega_0^2 + i\Gamma\omega} \quad (5.3)$$

where ω_p is the plasma frequency, ω_0 is the resonance frequency and Γ is a damping factor. The frequency where $\epsilon(\omega) = 0$ occurs at $\omega_L^2 = \omega_0^2 + \omega_p^2$.

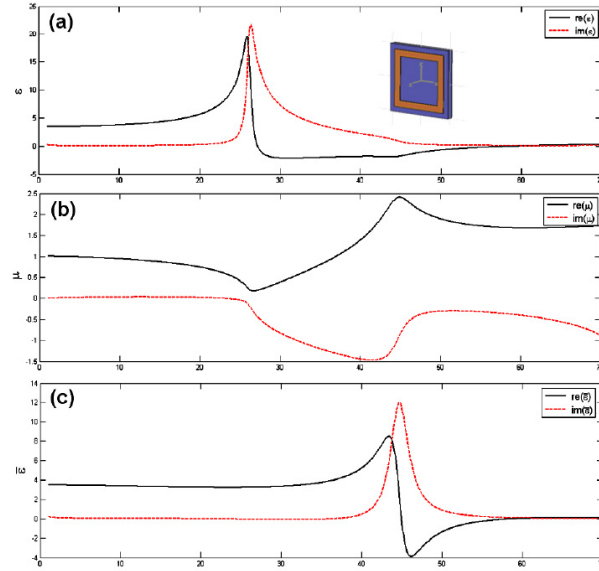


FIGURE 5.6: (a) Retrieved permittivity for a metamaterial composed of the repeated unit cell shown in the inset; (b) retrieved permeability for a metamaterial composed of the repeated unit cell shown in the inset. (c) The distortions and artifacts in the retrieved parameters are due to spatial dispersion, which can be removed to find the Drude-Lorentz like resonance shown in the lower figure.[54]

Table of resonant and plasma frequency

a	f_0	f_L	$\epsilon_{\text{predicted}}$	ϵ_{actual}
1.70	44.0	59.0	3.416	3.425
1.55	54.0	64.0	2.670	2.720
1.40	64.0	71.0	2.338	2.315
1.20	77.4	79.2	1.989	1.885

Table 5.2: The predicted and actual zero-frequency permittivity values as a function of the unit cell dimension, a .

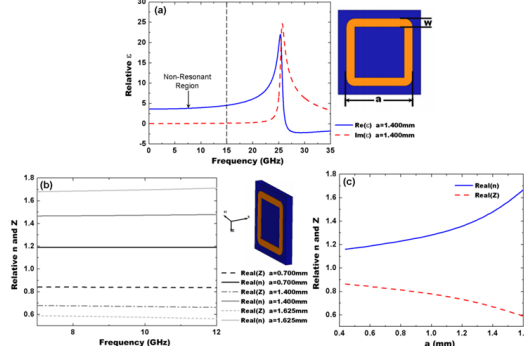


FIGURE 5.7: Retrieval results for the closed ring medium. In all cases the radius of curvature of the corners is 0.6 mm, and $w=0.2$ mm. (a) The extracted permittivity with $a=1.4$ mm. (b) The extracted index and impedance for several values of a . The low frequency region is shown. (c) The relationship between the dimension a and the extracted refractive index and wave impedance. [54]

As can be seen from either Eq.5.3 or Fig.5.6, the effective permittivity can achieve very large values, either positive or negative, near the resonance. Yet, these values are inherently accompanied by both dispersion and relatively large losses, especially for frequencies very close to the resonance frequency. Thus, although a very wide and interesting range of constitutive parameters can be accessed by working with metamaterial elements near the resonance, the advantage of these values is somewhat tempered by the inherent loss and dispersion. The strategy in utilizing metamaterials in this regime is to reduce the losses of the unit cell as much as possible. If we examine the response of the electric metamaterial shown in Fig.5.6 at very low frequencies, we find, in the zero frequency limit,

$$\epsilon(\omega \rightarrow 0) = 1 + \frac{\omega_p^2}{\omega_0^2} = \frac{\omega_L^2}{\omega_0^2} \quad (5.4)$$

The equation is reminiscent of the Lyddane-Sachs-Teller relation that describes the contribution of the polariton resonance to the dielectric constant at zero frequency [20]. At frequencies far away from the resonance, we see that the permittivity approaches a constant that differs from unity by the square of the ratio of the plasma to the resonance frequencies. Although the values of the permittivity are necessarily

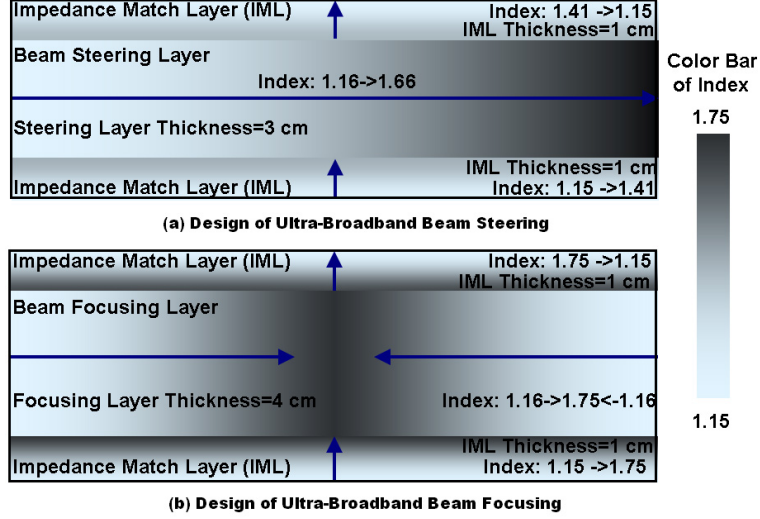


FIGURE 5.8: Refractive index distributions for the designed gradient index structures. (a) A beam-steering element based on a linear index gradient. (b) A beam focusing lens, based on a higher order polynomial index gradient. Note the presence in both designs of an impedance matching layer (IML), provided to improve the insertion loss of the structures.

positive and greater than unity, the permittivity is both dispersionless and lossless—a considerable advantage. Note that this property does not extend to magnetic metamaterial media, such as split ring resonators, which are generally characterized by effective permeability of the form

$$\mu(\omega) = 1 - \frac{F\omega^2}{\omega^2 - \omega_0^2 + i\Gamma\omega} \quad (5.5)$$

which approaches unity in the low frequency limit. Because artificial magnetic effects are based on induction rather than polarization, artificial magnetic response must vanish at zero frequency. The effective constitutive parameters of metamaterials are not only complicated by spatial dispersion but also possess an infinite number of higher order resonances that should properly be represented as a sum over oscillators. It is thus expected that the simple analytical formulas presented above are only approximate. Still, we can investigate the general trend of the low frequency permittivity as a function of the high-frequency resonance properties of the unit

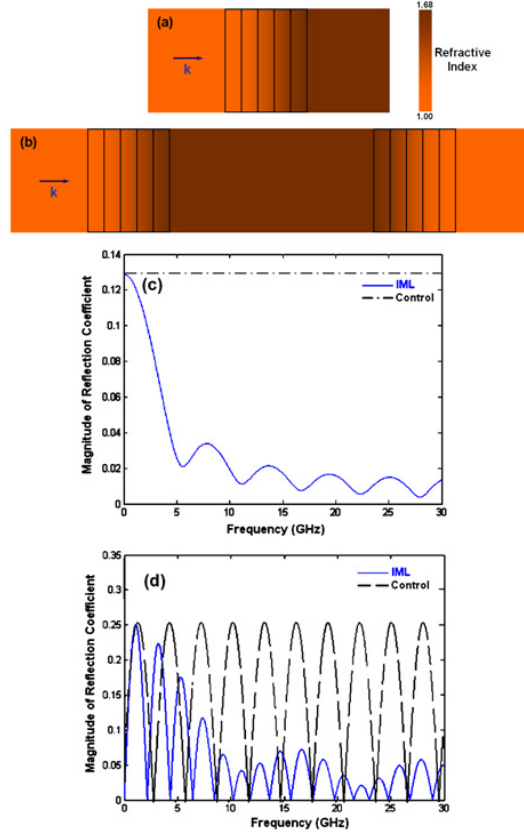


FIGURE 5.9: Refractive index distributions for the designed gradient index structures. (a) A beam-steering element based on a linear index gradient. (b) A beam focusing lens, based on a higher order polynomial index gradient. Note the presence in both designs of an impedance matching layer (IML), provided to improve the insertion loss of the structures.[54]

cell. By adjusting the dimension of the square closed ring in the unit cell, we can compare the retrieved zero-frequency permittivity with that predicted by Eq. 5.3. The simulations are carried out using HFSS (Ansoft), a commercial electromagnetic, finite-element, solver that can determine the exact field distributions and scattering (S-) parameters for an arbitrary metamaterial structure. The permittivity and permeability can be retrieved from the S-parameters by a well-established algorithm. Table 1 demonstrates the comparison between such simulated extraction and theoretical prediction. We should notice that as the unit cell is combined with a dielectric substrate, Eq.5.2 has been modified into $\epsilon(\omega \rightarrow 0) = \epsilon_a(1 + \frac{\omega_p^2}{\omega_0^2}) = \epsilon_a \frac{\omega_f^2}{\omega_0^2}$, in which

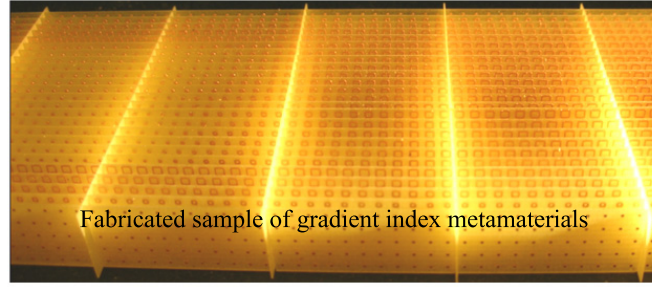


FIGURE 5.10: Fabricated sample, in which, the metamaterial structures vary with space coordinate.[54]

$\epsilon_a = 1.9$. The additional fitting parameter can represent the practical situation of the affect from substrate dielectric constant and the contribution to DC permittivity from high order resonances. Though there is significant disagreement between the predicted and retrieved values of permittivity, the values are of similar order and show clearly a similar trend: the high frequency resonance properties are strongly correlated to the zero frequency polarizability. By modifying the high-frequency resonance properties of the element, the zero- and low-frequency permittivity can be adjusted to arbitrary values.

Because the closed ring design shown in Fig.5.7 can easily be tuned to provide a range of dielectric values, we utilize it as the base element to illustrate more complex gradient-index structures. Though its primary response is electric, the closed ring also possesses a weak, diamagnetic response that is induced when the incident magnetic field lies along the ring axis. The closed ring medium therefore is characterized by a magnetic permeability that differs from unity, and which must be taken into account for a full description of the material properties. The presence of both electric and magnetic dipolar responses is generally useful in designing complex media, having been demonstrated in the metamaterial cloak. By changing the dimensions

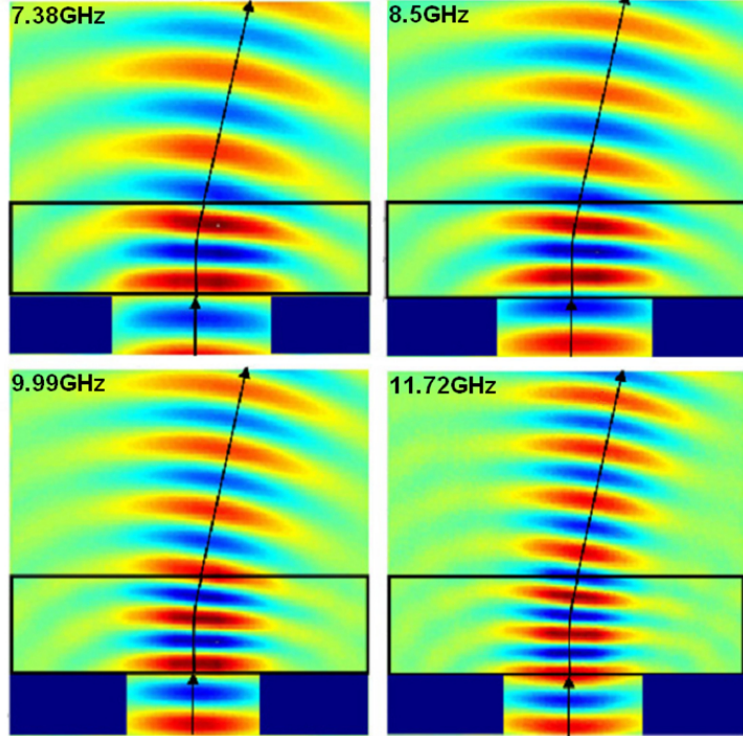


FIGURE 5.11: Field mapping measurements of the beam steering lens. The lens has a linear gradient that causes the incoming beam to be deflected by an angle of 16.2 degrees. The effect is broadband, as can be seen from the identical maps taken at four different frequencies that span the X-band range of the experimental apparatus.[54]

of the ring, it is possible to control the contribution of the magnetic response.

The permittivity can be accurately controlled by changing the geometry of the closed ring. The electric response of the closed ring structure is identical to the "cut-wire" structure previously studied, where it has been shown that the plasma and resonance frequencies are simply related to circuit parameters according to $\omega_p^2 \approx 1/L$ and $\omega_0^2 \approx 1/(LC)$. Here, L is the inductance associated with the arms of the closed ring and C is the capacitance associated with the gap between adjacent closed rings. For a fixed unit cell size, the inductance can be tuned either by changing the thickness, w , of the conducting rings or their length, a . The capacitance can be controlled primarily by changing the overall size of the ring.

Changing the resonance properties in turn changes the low frequency permittivity

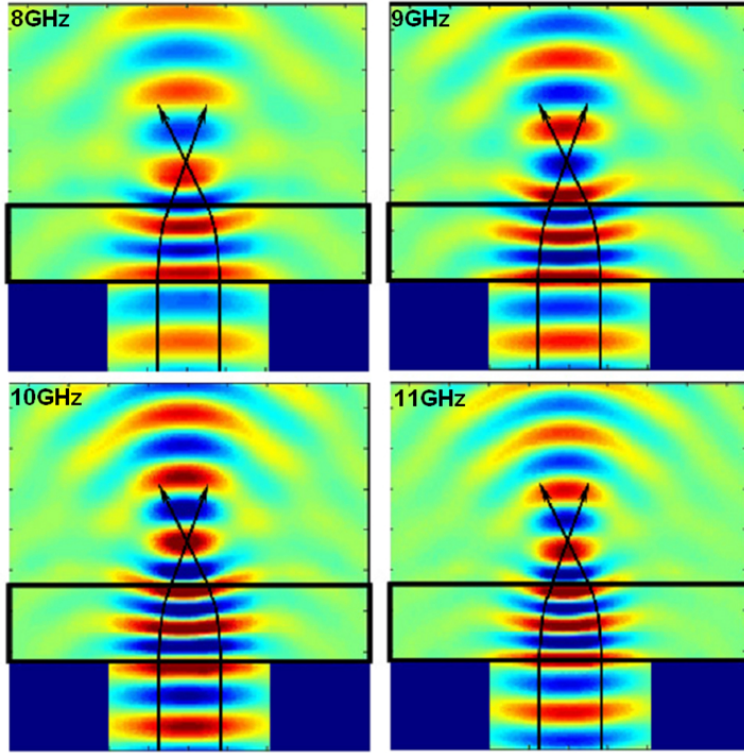


FIGURE 5.12: Field mapping measurements of the beam focusing lens. The lens has a symmetric profile about the center (given in the text) that causes the incoming beam to be focused to a point. Once again, the function is broadband, as can be seen from the identical maps taken at four different frequencies that span the X-band range of the experimental apparatus.[54]

value, as illustrated by the simulation results presented in Fig.5.7. The closed ring structure shown in Fig.5.7(a) is assumed to be deposited on FR4 substrate, whose permittivity is $3.85+i0.02$ and thickness is 0.2026 mm. The unit cell dimension is 2mm, and the thickness of the deposited metal layer (assumed to be copper) is 0.018 mm. For this structure, a resonance occurs near 25 GHz with the permittivity nearly constant over a large frequency region (roughly zero to 15 GHz). Simulations of three different unit cell with ring dimensions of $a = 0.7$ mm, 1.4 mm and 1.625 mm were also simulated to illustrate the effect on the material parameters. In Fig.5.7b, it is observed that the index value becomes larger as the ring dimension is increased, reflecting the larger polarizability of the larger rings.

The refractive index remains, for the most part, relatively flat as a function of frequency for frequencies well below the resonance. The index does exhibit a slight monotonic increase as a function of frequency, however, which is due to the higher frequency resonance. The impedance changes also exhibits some amount of frequency dispersion, due to the effects of spatial dispersion on the permittivity and permeability. The losses in this structure are found to be negligible, as a result of being far away from the resonance frequency. This result is especially striking, because the substrate is not one optimized for RF circuits-in fact, the FR4 circuit board substrate assumed here is generally considered quite lossy.

As can be seen from the simulation results in Fig.5.7, metamaterial structures based on the closed ring element should be nearly non-dispersive and low-loss, provided the resonances of the elements are sufficiently above the desired range of operating frequencies. To illustrate the point, we make use of the closed ring element to realize two gradient index devices: a gradient index lens and a beam steering lens. The use of resonant metamaterials to implement positive and negative gradient index structures was introduced in [20] and subsequently applied in various contexts. The design approach is first to determine the desired continuous index profile to accomplish the desired function (e.g., focusing or steering) and then to stepwise approximate the index profile using a discrete number of metamaterial elements. The elements can be designed by performing numerical simulations for a large number of variations of the geometrical parameters of the unit cell; once enough simulations have been run so that a reasonable interpolation can be formed of the permittivity as a function of the geometrical parameters, the metamaterial gradient index structure can be laid out and fabricated. This basic approach has been followed in [20].

Two gradient index samples were designed to test the bandwidth of the non-resonant metamaterials. The color maps in Fig.5.8 show the index distribution corresponding to the beam steering layer (Fig. 5.8a) and the beam focusing lens

(Fig.5.8b). Although the gradient index distributions provide the desired function of either focusing or steering a beam, there remains a substantial mismatch between the predominantly high index structure and free-space. This mismatch was managed in prior demonstrations by adjusting the properties of each metamaterial element such that the permittivity and permeability were essentially equal. This flexibility in design is an inherent advantage of resonant metamaterials, where the permeability response can be engineered on a nearly equal footing with the electric response. By contrast, that flexibility is not available for designs involving non-resonant elements, so we have instead made use of a gradient index impedance matching layer (IML) to provide a match from free-space to the lens, as well as a match from the exit of the lens back to free space.

The beam steering layer is a slab with a linear index gradient in the direction transverse to the direction of wave propagation. The index values range from $n = 1.16$ to $n = 1.66$, consistent with the range available from our designed set of closed ring metamaterial elements. To improve the insertion loss and to minimize reflection, the IML is placed on both sides of the sample (input and output). The index values of the IML gradually change from unity (air) to $n = 1.41$, the index value at the center of the beam steering slab. This index value was chosen because most of the energy of the collimated beam passes through the center of the sample. To implement the actual beam steering sample, we made use of the closed ring unit cell shown in Fig.5.7 and designed an array of unit cells having the distribution shown in Fig. 5.8a.

The beam focusing lens is a planar slab with the index distribution as represented in Fig. 5.8b. The index distribution has the functional form of

$$Re(n) \approx 4 \times 10^{-6}|x|^3 - 5 \times 10^{-4}|x|^2 - 6 \times 10^{-4}|x| + 1.75 \quad (5.6)$$

in which x is the distance away from the center of the lens. Once again, an IML was used to match the sample to free space. In this case, the index profile in the IML

was ramped linearly from $n = 1.15$ to $n = 1.75$, the latter value selected to match the index at the center of the lens. The same unit cell design was utilized for the beam focusing lens as for the beam steering lens.

To analyze the reflection minimization by metamaterial IML, we create a simple analysis model to illustrate the function of IML, shown in Fig.5.9. We study the reflection coefficient between the air and a dielectric with refractive index $n=1.68$. Fig.5.9 (a) shows a scenario that an IML metamaterial, composed of five linear gradient index step layer, is presented at the interface between the air and dielectric. Each step layer's thickness is 2mm. Fig.5.9 (b) shows the usage of IML on a dielectric slab. The impedance mismatch is expected to be minimized by IML at the interface. Fig.5.9 (c) and (d) demonstrate the reflection coefficient with and without IML for the case in Fig.5.9 (a) and (b) respectively. As can be seen in Fig.5.9 (c), the reflection coefficient at DC frequency is identical between the IML case and its control because the wavelength is so long that the IML is invisible to the wave. However, the reflection coefficient drops down quickly as frequency raising. At 5GHz, the reflection coefficient has been reduced from 0.13 to below 0.04. Fig.5.9 (d) illustrates the improvement in reflection coefficient by adding the IML at both interfaces of a dielectric slab. The reflection coefficient can be minimized to half of the one by control above 7GHz. Therefore, we can take the advantage of the flexibility on non-resonant metamaterials to implement the IML in various designs to minimize the reflection.

To confirm the properties of the gradient index structures, we fabricated the two designed samples using copper clad FR4 printed circuit board substrate, shown in Fig.5.10. Following a procedure previously described, sheets of the samples were fabricated by standard optical lithography, then cut into 1 cm tall strips that could be assembled together to form the gradient index slabs. To measure the sample, we placed them into a 2D mapping apparatus, which has been described in details⁵ and

mapped the near field distribution[51].

Fig.5.11 shows the beam steering of the ultra-broadband metamaterial design, in which, a large broadband is covered. The actual bandwidth starts from DC and goes up to approximately 14GHz. From Fig.5.11, it is obvious that beam steering occurs at all the four different frequencies from 7.38GHz to 11.72GHz with an identical steering angle of 16.2 degree. The energy loss through propagation is extremely low and can barely be observed. Fig.5.12 shows the mapping result of the beam focusing sample. Broadband property is demonstrated again at four different frequencies with an exact same focal distance of 35mm and low loss. In summary, we proposed ultra-broadband metamaterials, based on which complex inhomogeneous material can be realized and accurately controlled. The configuration of ultra-broadband metamaterials and the design approach are validated by experiments. Due to its low loss, designable properties and easy access to inhomogeneous material parameters, the ultra-broadband metamaterials will find wide applications in the future.

5.4 Random gradient index metamaterials

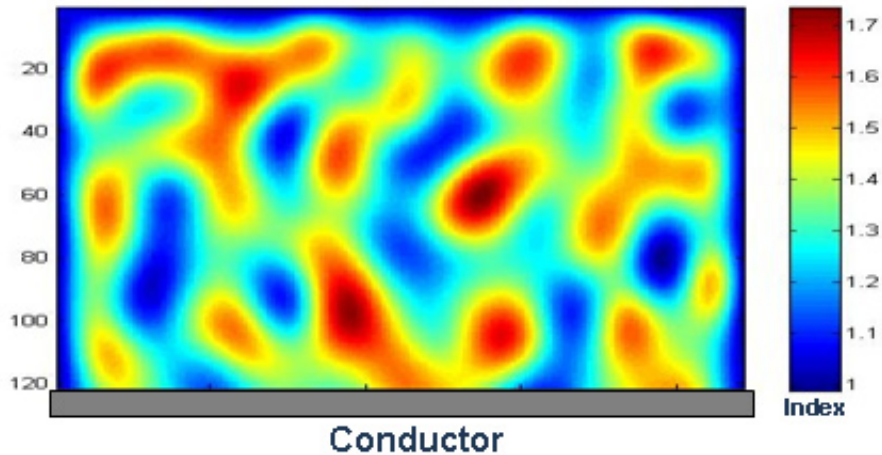


FIGURE 5.13: Index distribution of gradient random medium

As we have the technology of building a complex inhomogeneous media by non-

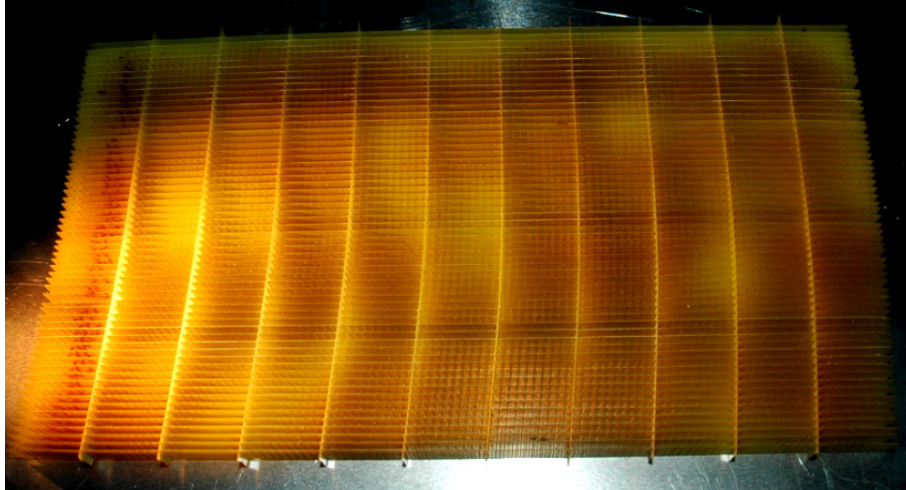


FIGURE 5.14: The fabricated sample on the designed random gradient index metamaterials

resonant metamaterials and the approach of rapid design, we will demonstrate the opportunity to manipulate waves in a further step. In this section, we introduce a complex random material whose randomness is precisely controlled and generated. The function of such random media is to maximally diffuse the electromagnetic waves by covering it on a top of flat conducting surface. Shown in Fig.5.13, the distribution of refractive index indicates a random and complex media presented here. To describe the basic feature of this type of metamaterials, it matches the impedance of air, makes no reflection at its smooth surface, and gradually changing its refraction index randomly. The complex local material parameter creates a puzzle for wave propagation in front of a metal conductor. Thus, such type of coating is expected to diffuse the reflection waves by covering on top of a conductor metal. As the material's local properties are precisely designed arbitrarily, the randomness of gradient index material can be extremely well controlled.

The random behavior of trajectories of electromagnetic waves can be obtained via the random behavior of the electric permittivity and magnetic permeability values in the metamaterial. Since the magnetic permeability values do not vary significantly,

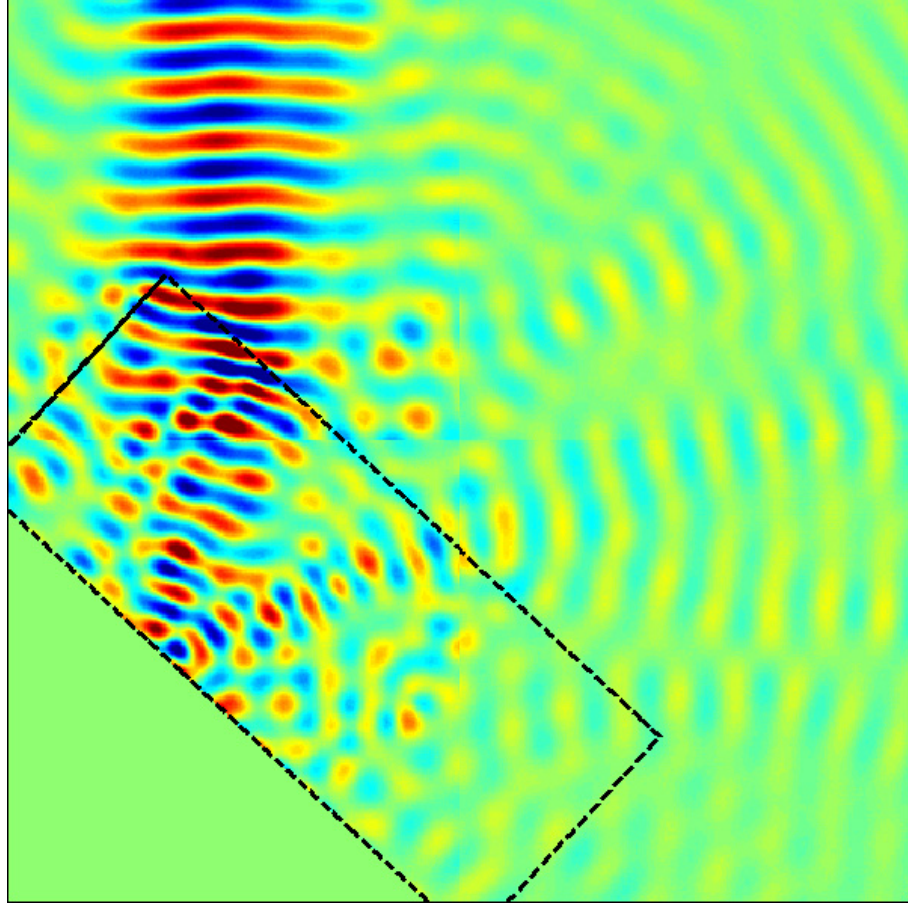


FIGURE 5.15: 2D mapping result for gradient random medium

the vary of permittivity and permeability can be also characterized by the refractive index. Therefore, the random algorithms which enable the random change of the trajectories of electromagnetic waves can be achieved by the corresponding spatial index distribution. The design of index distribution is achieved by using certain nonlinear regression approach under the boundary condition for impedance matching. We take the advantage of the random behavior of Gaussian processes, a recent emerged nonlinear regression technique. By setting several achievable index values at several random selected spatial points and giving the boundary condition for impedance matching, $n = 1$ on the boundary, we obtain a smooth spatial distribution of index by Gaussian processes regression. The index distribution is shown in Fig.5.12. Note

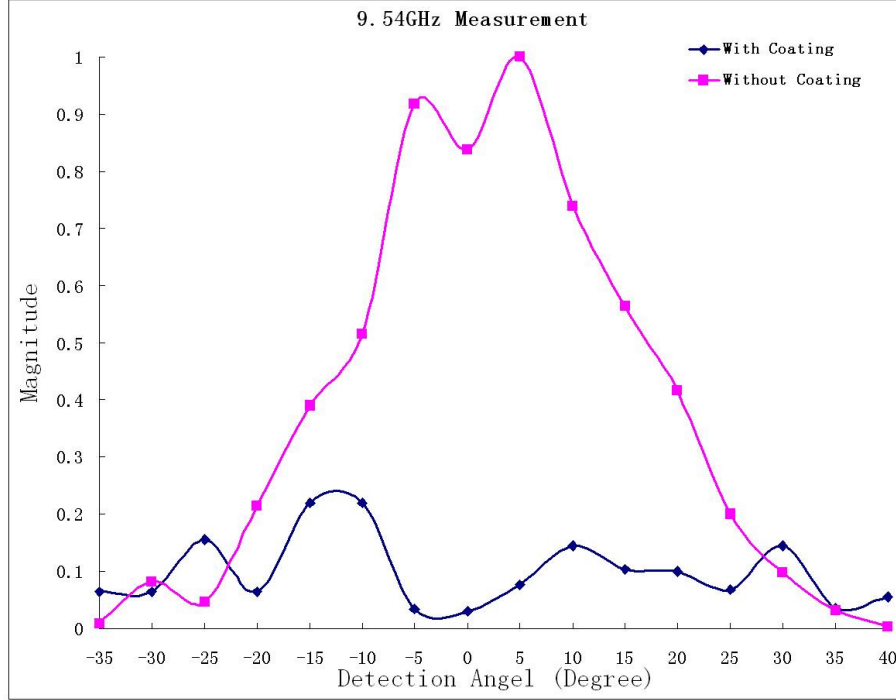


FIGURE 5.16: Angular resolution detection of gradient random medium

that such design prescription can be used to a much larger layered random gradient index design and can be useful in practical case.[79]

The implementation of the particular design here requests more than 30000 different unit cells. Such large scale design and mask generation have been out of the scope of manual production. Therefore, we employ the rapid design system for the present case and enable the implementation on such complex media, shown in Fig. 5.14. To measure the diffusing effect, we coated the random gradient index metamaterial in front of a long conductor reflector in the 2D near field scanning apparatus. Fig.5.15 demonstrates the wave propagation in such set-up. The incoming beam incidents from top to bottom and encounters the random gradient index metamaterials. At the boundary of the media, as the impedance is designed to match that of the air, no significant reflected waves is observed. Whereas, the scattering waves has highly diffused by penetrating across the media. To further characterize the diffusing

function, an angular measurement with and without the coating has been taken. A strong directional scatter can be observed in this experiment if the conductor is not coated by the random media. Whereas, with the coated random media, the wave energy was "flattened out" in all angles to the far field.

In conclusion, we can design a media with the arbitrary local properties. By employing the nonlinear regression approach, we can generate a complex media that the well controlled random local properties can diffuse the wave propagation while matching the impedance from the air. By utilizing the rapid design system, such complex media can be implemented by gradient index metamaterials. The experiment demonstrates the advantage and opportunity of controlling electromagnetic waves by large scale scatters.

Some of the work here has been published in Optical Express[54] and conference paper[79].

Cloaking Devices Design and Experiment

6.1 Introduction to transformation optics

Transformation optics is a novel approach for the design of complex electromagnetic media that offers new opportunities for the manipulation of electromagnetic waves [24]. By taking use of the transformation optical approach, a wide variety of devices can be conceptually designed in theory with unique properties, including beam shifters; beam bends; beam splitters; focusing and collimating lenses; and structures that concentrate electromagnetic waves. One of the most compelling examples of the transformation optical technique has been the prescription for an invisibility cloak—a material by rendering which other objects can be hidden from detection. The prospect of cloaking has proven a tantalizing prospect to the community, with numerous cloaking concepts currently being investigated.

The transformation optical approach is conceptually simple. One imagines warping space so as to control the trajectories of light in a desired manner. Light that flows in a straight line in the unwarped space instead follows a route in the warped space dictated by the details of the coordinate transformation that connects the two

spaces. As what is now an iconic example of the transformation optical approach, an invisibility cloak can be conceptually constructed by poking a hole in space and compressing the space within the original region to within a shell excluding the object volume.

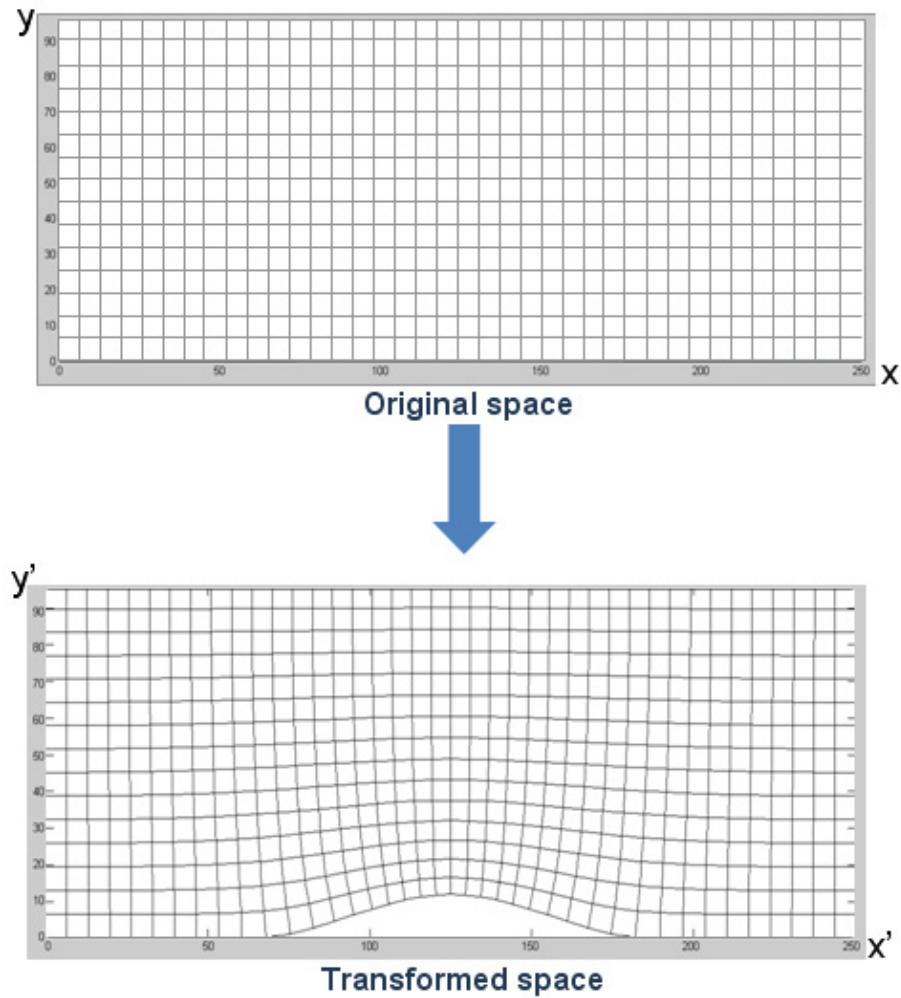


FIGURE 6.1: An example of a coordinate transform

We start the discussion on transformation optics from a coordinate transform, for example, shown in Fig.6.1. Such coordinate transformation can be arbitrarily made and applied to Maxwells' equations. The coordinate transform can be represented by $\vec{r}' = R(\vec{r})$ and calculated by Jacobian matrix $\overline{\overline{\Lambda}}$. We can, thus, achieve the

electric field and magnetic field in the transformed space that [1] $\overline{E}'(\overline{r}') = (\overline{\Lambda}^T)^{-1}\overline{E}(\overline{r})$ and $\overline{H}'(\overline{r}') = (\overline{\Lambda}^T)^{-1}\overline{H}(\overline{r})$. We know that the electromagnetic wave propagation is governed by Maxwell's equations regardless of the coordinate selection. We can write down the Maxwell's equations in both original space and transformed space and achieve that

$$\begin{aligned}\nabla \times \overline{E} + i\omega\overline{\mu}\overline{H} &= 0 \\ \nabla \times \overline{H} - i\omega\overline{\epsilon}\overline{E} &= 0\end{aligned}\tag{6.1}$$

in the original space and that

$$\begin{aligned}\nabla \times \overline{E}' + i\omega\overline{\mu}'\overline{H}' &= 0 \\ \nabla \times \overline{H}' - i\omega\overline{\epsilon}'\overline{E}' &= 0\end{aligned}\tag{6.2}$$

in the transformed space. Because Maxwell's equations contain terms that define the properties of a material, the transformation can alternatively yield a specification for a medium in the form of spatially varying electric permittivity and magnetic permeability values. To remain the Maxwell's equation from original space and transformed space. we can solve the materials' properties in the transformed space and achieve that

$$\begin{aligned}\overline{\mu}'(\overline{r}') &= \overline{\Lambda}\overline{\mu}(\overline{r})\overline{\Lambda}^T / \det\overline{\Lambda} \\ \overline{\epsilon}'(\overline{r}') &= \overline{\Lambda}\overline{\epsilon}(\overline{r})\overline{\Lambda}^T / \det\overline{\Lambda}\end{aligned}\tag{6.3}$$

According to Eq.6.3, we can make a use of new materials' property to map the space to electromagnetic wave propagation and distort the original coordinate to the transformed space. To intuitively understand the physics behind, based on Eq.6.3, we need a higher index material if the space is compressed; a lower index material if the space is expanded; an anisotropic material if the space is twisted. Thus

the resulting medium is in general highly complex, being anisotropic with spatial gradients in the tensor elements of the constitutive parameters. The prospect of realizing transformation optical structures, then, comes down to being able to find or construct the specified materials.

Though the specifications for transformation optical structures would generally be difficult to achieve using conventional materials, the prospects are much better for achieving them using artificially structured metamaterials. Over the past several years, metamaterials have been shown to possess a wide range of electromagnetic properties that would be difficult or even impossible to achieve with conventional materials. Moreover, the properties of metamaterials can be engineered with great precision over a broad range of frequencies and are well suited to implement the complex gradients required by transformation optical structures. In 2006, a cloak design was realized in a metamaterial sample, which demonstrated the cloaking mechanism over a narrow band of microwave frequencies shown in Fig.6.2.[25]

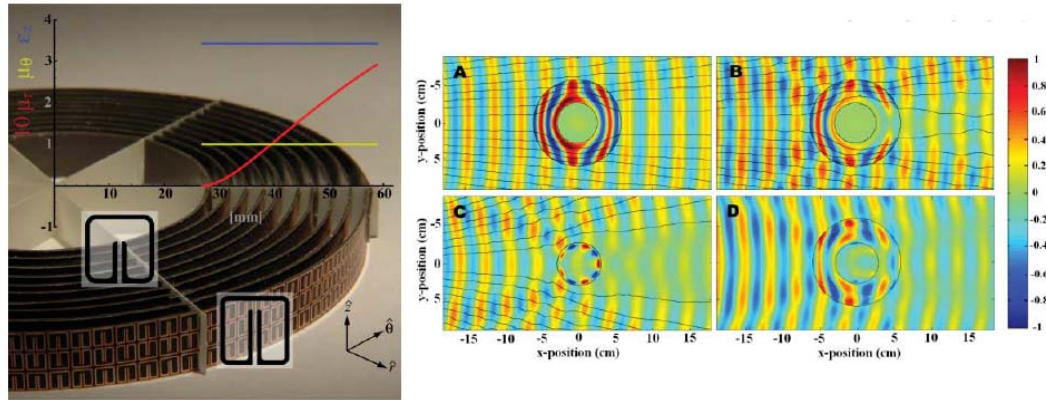


FIGURE 6.2: From Ref.[25]. The design of reduced parameter invisible cloak and the simulations and measurements of cloak and metal cylinder, in which, A. ideal simulation B. simulation on reduced cloak, C. control experiment D. experiment on the reduced cloak

6.2 Invisibility cloak design in free space

In the last section, we discuss the transformation optics approach that enables a conceptually design on the invisibility cloak and also give an example of a cloaking experiment in 2006[25]. In this section, we will further discuss the details of such cloaking design and experiment and also illustrate a new set of cloaking design and experiment by applying the rapid design approach that has been discussed in chapter three.

The design on this particular cylindrical cloaking device employs the coordinate transform from a cylindrical volume to a shell excluding the object in the center as shown in Fig.6.2. Assuming the inner radius is a and outer radius is b , one can achieve the materials' parameters by Eq.6.3 and achieve that [25]

$$\begin{aligned}\mu_r &= \frac{r-a}{r} \\ \mu_\theta &= \frac{r}{r-a} \\ \epsilon_z &= \left(\frac{b}{b-a}\right)^2 \frac{r}{r-a}\end{aligned}\tag{6.4}$$

for a TE polarization. However, such parameters are highly anisotropic and inhomogeneous and of singularity at the inner boundary $r = a$. Although the conceptual design provides the opportunity of a perfect invisibility, the practical implementation is limited by the finite response of metamaterials and complexity of 3D structure fabrication. To address this practical difficulty, Schurig et. al. proposed a reduced design to the cylindrical cloaking device by relaxing the impedance requirement but remaining the refractive index to the materials. One can imagine a ray-tracing process to such reduced cloak. The remaining refractive index can allow the trajectory of wave propagation still rendering the object. Whereas the imperfect reflection and field distortion on transmission will unavoidably occur in reality, shown in Fig.6.2.

The reduced parameters design can be then achieved from Eq.6.4 and be expressed by

$$\begin{aligned}\mu_r &= \left(\frac{r-a}{r}\right)^2 \\ \mu_\theta &= 1 \\ \epsilon_z &= \left(\frac{b}{b-a}\right)^2\end{aligned}\tag{6.5}$$

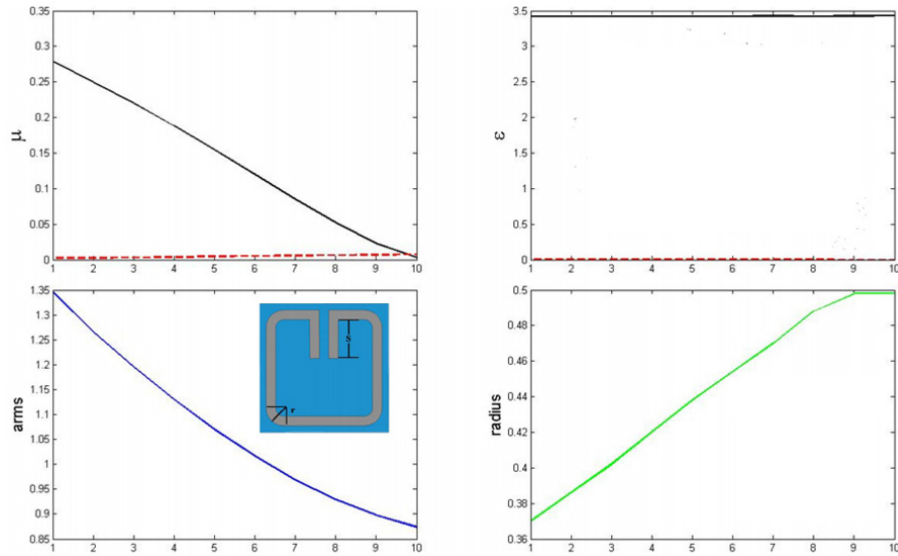


FIGURE 6.3: Rapid design for a reduced cloak, working at 10GHz

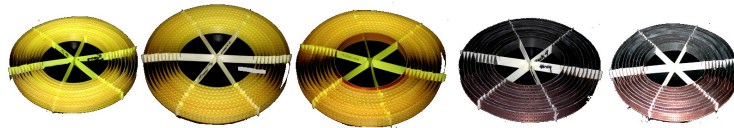


FIGURE 6.4: Fabricated invisible cloak by rapid design system

Although the first demonstration of cloaking experiment was far from perfect, the breakthrough on the concept and methodology has led this work to one of the most impact development on metamaterials. To further study this experiment, we can find that such anisotropic and inhomogeneous media is implemented by a set of split ring resonators (SRRs). The change of geometry of SRR will allow the implementation of

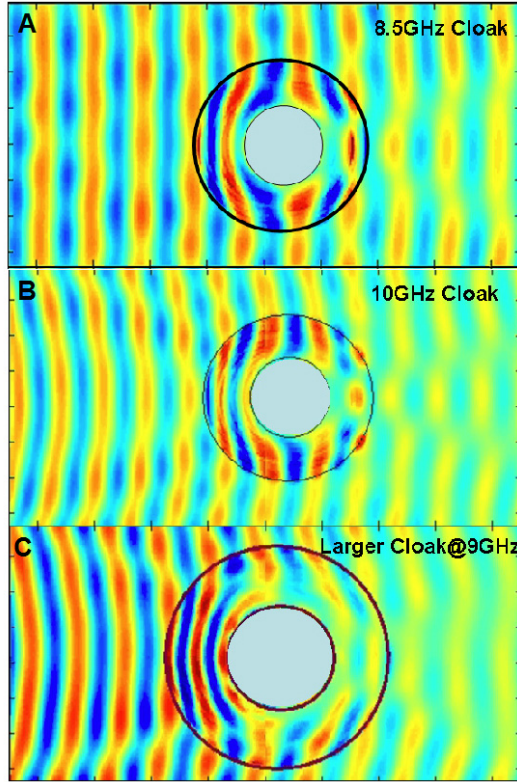


FIGURE 6.5: Invisible cloak measurement

different local material property. In the experiment in Fig.6.2, ten unique SRRs have been designed from inner layer to outer layer and to achieve $\mu_r = 0$ to $\mu_r = 0.278$. The traditional design process follows a loop that many full wave simulations have to be taken on various SRR until the effective permittivity and permeability meet the requirement from transformation optics calculation at certain spatial point and certain frequency. Therefore, in this cylindrical cloaking design, there are ten unique structures. Approximate ten iterations is needed to design a particular structure. One iteration will consume five minutes on the step of full wave simulations. Ideally a thousand minutes is requested to design a particular cloak at a particular frequency. This efficiency also challenges the metamaterial technology. To address this difficulty, we incorporate the rapid design approach described in chapter three. By employing the rapid design algorithm on metamaterial structure calculation, metamaterial re-

sponse can be easily predicted and expressed in terms of analytical form based on the library built by pre-simulated data. Once the library of certain type of unit cell structure is built, it can be integrated together with the system level design, experimental configuration and fabrication requirement. The system level design indicates the electromagnetic parameters requirement calculation. For example, transformation optics is a type of system level design, from which, required permittivity and permeability distributions for certain function can be calculated. The experimental configuration means the type of metamaterials, such as 1D transmission line metamaterials, 2D waveguided metamaterials, or 3D structural metamaterials. Different types of metamaterials have their special features for various applications, and thus appear different in the design system.

Applying the rapid design system, we can design the reduced cloak automatically and, achieve the material's parameters and metamaterial structure geometry, for example, shown in Fig.6.4. Based on the same design library, we designed and fabricated various different cloaks with different dimensions and operational frequencies. Figure 6.4 shows the fabricated cloaks by our sophisticated design system. The yellow cloaks are made on FR4 substrate while the black ones are on Duroid5880 substrate with lower loss. Excluding the design library extraction (as we only did that once), all these different cloaking devices were designed in ten seconds, comparing with a thousand minutes for a particular one in the past. Figure 6.5 shows the series of invisible cloak measurements. All the experiments are designed by the same structure library(Rogers Duroid5880 SRR unit cell) and measured within 0.1GHz error around designed frequency from rapid design system, showing the accuracy of this rapid metamaterial design approach.

6.3 Broadband ground-plane cloak

We discussed the invisibility cloak design and experimental demonstration on the reduced cloaks in the last section. From the cloak prototype experiment, we see both the opportunity and challenge for metamaterials. The rapid design system has dramatically improved the efficiency of the previous cloaking experiment. In this section, we will continue on the trajectory of the development on cloaking devices and demonstrate a much more complex media and structures that lead to a function of broadband ground-plane cloak. As discussed, the metamaterial cloak represented an approximation to the ideal cloak specification, arrived at by the transformation optical approach. In fact, the required constitutive parameters for the ideal cloaking structures are highly demanding even for metamaterials, generally requiring separate control over at least three of the constitutive parameters for TE or TM polarization. In the reduced cloak design, the material's property request the elements of the relative permittivity and permeability tensors must be between zero and unity, most cloak designs will need to be based on resonant elements. The use of these elements sets an inherent limit on the bandwidth over which the cloaking effect exists and leads to a greater dissipation of the waves as they propagate through the structure.

There are an endless number of coordinate transforms that will arrive at a structures that will provide varying degrees of cloaking. In a recent theoretical study, Li and Pendry describe the design of a structure that can cloak objects placed on a conducting sheet. Though a more limited form of cloaking, the required constitutive parameters for this ground-plane cloak are much easier to achieve with the metamaterial techniques currently available.

To design the ground plane cloak, Li and Pendry first restrict the problem to a two-dimensional plane of uniform dielectric value ϵ_b with the electric field assumed polarized out of the plane (transverse electric polarization). In general, the trans-

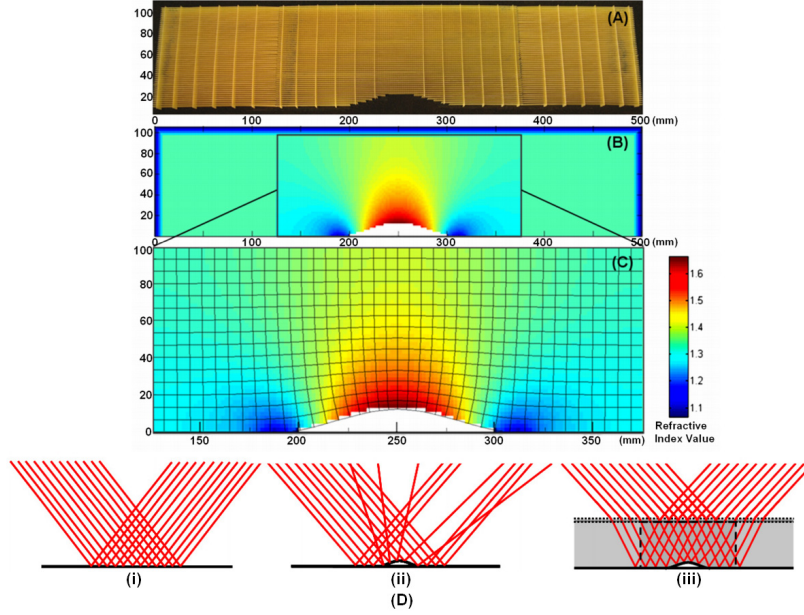


FIGURE 6.6: The transformation optics design for carpet cloak embedded with background materials and impedance matching layers. The white part is the object supposed to be hid and meshing line indicates the quasi-conformal mapping. The color map shows the designed refractive index distribution.[26]

formation would lead to an anisotropic medium with values of ϵ_z , μ_x and μ_y that vary as a function of the spatial coordinate. Because there are an infinite number of coordinate maps that will lead to the same cloaking behavior, Li and Pendry search for a map that minimizes the anisotropy in the permeability components. Defining an anisotropy factor as $\alpha = \max(n_x/n_y, n_y/n_x)$, it is possible to find transformations for which α is near unity. For such transformations, the permeability can be simply set to unity, and the permittivity varied. If the background dielectric in the original space is sufficiently greater than unity, then the values for the permittivity of the cloaking structure are always greater than unity; this feature allows the possibility of utilizing non-resonant metamaterial elements and thus making the cloak broadband.

Following the procedure outlined by Li and Pendry, we design a ground plane cloak that minimizes the anisotropy factor. Li and Pendry stated that the quasi-conformal map [80], generated by minimizing the Modified-Liao functional [81] upon

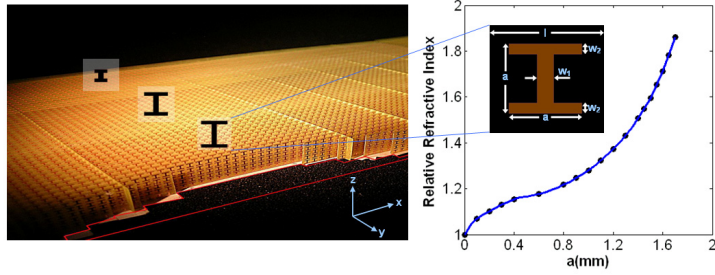


FIGURE 6.7: The unit cell design of the non-resonant element and fabricated sample according to the relationship between the geometry dimension and effective index.[26]

slipping boundary condition, minimizes the anisotropy in the permeability components. Numerical mapping technique are then applied to achieve the Jacobian matrix Λ of quasiconformal mapping from the physical system and virtual system, and then the required index distribution $n^2 = \frac{1}{\sqrt{|\Lambda^T \Lambda|}}$. In our final design, $\alpha = 1.04$, which we treat as negligible (that is, we assume $n_x = n_y = 1$). A color map indicating the transformed space and the associated refractive index distribution is shown in Fig.6.6. (The final map is generated numerically by the optimization procedure, so there are no closed form analytic expressions that define the transformation.) To simplify the design so that non-resonant metamaterial elements can be used, we assume the entire cloak is embedded in a background material with refractive index $n = 1.331$. Under these assumptions, the transformation leads to refractive index values for the ground plane cloak that range from $n = 1.08$ to $n = 1.67$. Note on the right and left side of the cloak, the refractive index distribution is uniform, taking the value of the background material.

Because it is convenient to launch waves in free space, the homogeneous background material in which the cloak is embedded presents a complication, since incident waves from free space will encounter an impedance mismatch and scatter. To avoid this complication, we add an impedance matching layer (IML) around the structure, for which the index changes gradually and linearly from the index of air

to the background dielectric. The procedure for designing the IML layer is described in Ref.[5]. Although the entire configuration is not hidden from detection by the incident waves from free space, the embedded IML and cloak structure can render an object invisible inside the background medium and above the ground plane. Because of the index gradient coupled with the cloak, we expect no amplitude scattering and only a slight redirection of the wave reflected from the ground plane structure. The effect should be similar to observing a mirror through an extremely thin, glass plate; objects on top of the mirror remain hidden from detection.

Because the required index distribution both for the IML and the cloak always take values greater than unity, it is possible to utilize metamaterial elements far from resonance to implement the cloak, which has been described in chapter five. To implement the transformation optical design for the ground plane cloak, we make use of the I-shaped particle shown in Fig.6.7. Following a well-established retrieval process, the effective permittivity for a given element can be found. By varying the geometry, a range of refractive index values can be obtained as illustrated in the inset to Fig.6.7, according to which, a rough relationship between the refractive index value and geometry dimension a is depicted. The transformation optical design in Fig.6.5 can thus be implemented by utilizing the metamaterial unit cell variations shown in Fig.6.7. The assembled cloak, shown also in Fig. 6.7, contains more than sixty thousand unit cells—roughly half of which are distinct—and is fabricated on copper-clad printed circuit board with FR4 substrate (the substrate thickness is 0.2026 mm with a dielectric constant of $3.85+i*0.02$). The completed sample is 500mm by 106mm with a height of 10mm, in which the center 250mm by 96mm corresponds to the transformed region. The shape of the object hidden within the ground plane cloak follows the curve $y = 12 * \cos^2((x - 125)\pi/125)$ (units in mm), analogous to the perturbation considered by Li and Pendry.

To address the numerical burden associated with the design of such a large-scale

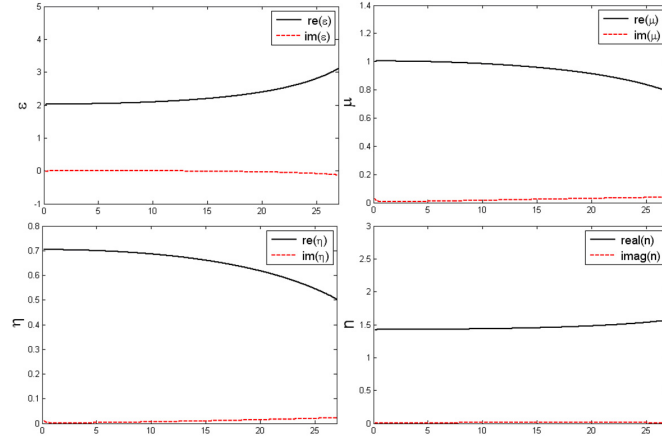


FIGURE 6.8: Effective permittivity, permeability, impedance and refractive index of I-Shape unit-cell with the dimension $a=1.4\text{mm}$. [26]

metamaterial structure, we have automated several aspects of the design process, enabling us to produce thousands of unique metamaterial elements rapidly that are consistent with the optimized transformation optical map. We define as system level the overall spatially varying constitutive parameters defined by the transformation optical procedure, and define as particle level the design of the constituent elements that form the metamaterial implementation. The first step of the automated design process—the system level design—employs numerical computation of the transformation optical mapping. The arbitrary shape of the cloaked perturbation can be modeled by a free curve regression. We then numerically computed the relationship at every spatial point between the original space and the transformed space by using a quasi-conformal mapping algorithm [81]. Once the mapping has been determined numerically, the transformation optics formula can then be used to calculate the permittivity and permeability tensors, in which a numerical derivative is taken. The conclusion of the first step, or the system level design, results in the spatial distribution of the constitutive parameters.

The second step in the process is to design and calculate the physical dimensions and structure for each unit cell that forms the cloaking. This step is the particle level

design step. We note that Li and Pendry [80] suggested a transformation optical (system level) design in which the permeability should remain unity everywhere and only the permittivity vary. Such a transformation would imply the particle level design should be relatively straightforward, since only electric response would be necessary to control. However, metamaterial structures, even those based on non-resonant elements, always exhibit spatial dispersion (i.e., constitutive parameters that depend on the direction of wave propagation) due to the finite size of the unit cell relative to the wavelength, shown in Fig.6.8. The impact of spatial dispersion is to introduce frequency dispersion into the constitutive parameters, which leads to a frequency dependent magnetic response in addition to that of the frequency dependent electric response, as shown in Fig.6.8. Thus, it is necessary to consider the spatial dispersion associated with each unit cell as part of the particle level design process. We incorporate all of the details associated with the finite unit cell into the design procedure using a quasi-analytical method previously described (Ref.[54]). The complete response of the metamaterial element, including the effects of spatial dispersion, can then be mathematically modeled by linear or nonlinear regression. Once we choose one or several physical dimensions of the unit-cell as variables for a given unit cell topology, we can then build a mathematical model to express the dispersive constitutive parameters via sampling a small set of unit-cell structures whose properties are computed by full wave simulations. Once the library of a certain type of structure is built, a rapid searching algorithm, such as the sequential Monte Carlo, can be applied to determine the appropriate physical dimension of the structure that achieves the required refractive index and impedance. In our design, the refractive index remains approximately constant with frequency but the impedance may vary as a function of frequency for different unit cell designs. In the final cloak, the unit cells on the periphery of the structure are designed to have an impedance that is nondispersive, while the impedances of the unit cells within

the cloaking region change continuously as a function of the spatial coordinate at all operational frequencies. The waves thus neither reflect at the outside edge of the cloak nor inside the cloak due to the careful design of the outside edge unit cells and the gradually varying impedance. Integrating all of these constraints into the optimization algorithm, we arrive at a metamaterial element (as shown in Fig.6.7) for which the refractive index value of the element can be directly related to its physical dimensions.

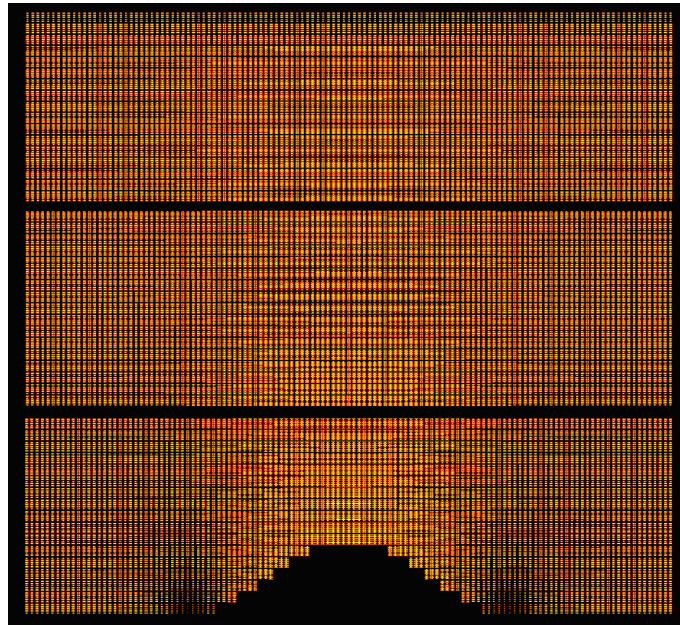


FIGURE 6.9: Ground-plane cloak mask (transformation region) generated by automatic design system. Not shown here are the cutting outlines, with slots for assembly, around which each strip (5 unit cells, 10mm, in height) is cut out by circuit board prototype milling machine (LPRF)[26]

The final step of the process is to take each unit cell geometry determined in the particle level design step and generate a large-scale mask of the entire layout for fabrication by printed circuit board (PCB) lithographic methods. The final mask, shown in Fig.6.9, has more than thirty thousand unit cells with more than six thousand unique unit cells. The mask is generated by the same Matlab program that also performs the first two steps, so that the entire process-system and particle level

designs, followed by layout and mask generation-are combined together. The Matlab program has calls to AutoCAD functions that draw all of the unit cells into the layout, producing the final mask.

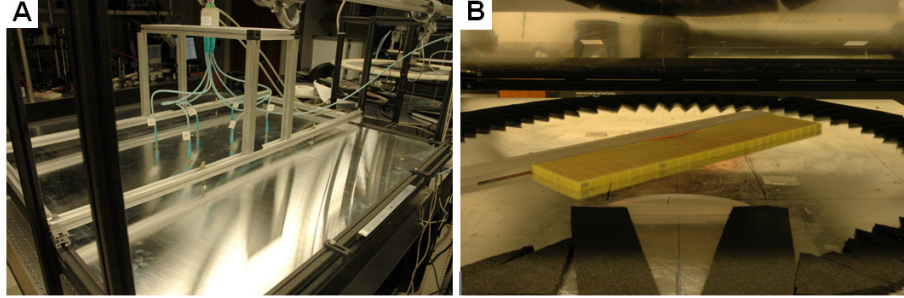


FIGURE 6.10: Ground-plane cloak mask (Experimental apparatus for the ground-plane cloak measurement. The apparatus consists of two metal plates separated by 1cm, which form a 2 dimensional planar waveguide region.[26])

To measure the fabricated sample in our lab, Fig.6.10 shows a top view of the closed mapping apparatus with six coaxial cables running from a switch to six antenna positions. Microwave measurements are made by a Vector Network Analyzer and the planar waveguide fields are launched by an X-band waveguide coupler towards a polycarbonate collimating lens, as shown in the open chamber view of Fig.6.10B, which creates the narrow beam seen in the measurements. This beam is reflected off of the ground plane at an angle of about 40 degrees from the surface normal. By scanning the top plate (with detector antenna) relative to the bottom plate (and sample) with 181 x 181 1mm steps, we can create a field map of the microwave beam incident on the ground-plane cloak. Due to the large area required for characterizing the full incident and reflected beams, at each plate step we simultaneously measure the electric field from 4 distinct antenna positions using the switch. These 4 scan areas can then be patched together into one large field map using Matlab code to match up the phase and amplitude at the boundaries of each probe region. Comparing the reflection from the ground plane, the ground plane with the perturbation and the ground plane with the cloaked perturbation (shown in Fig.S1B), we can

demonstrate the cloaking effect. Broadband performance is confirmed from mapping the field incident upon the cloak for 13 - 16 GHz for this certain experiment. While we expect that the cloak would work for much lower and higher frequencies, we do not obtain clean measurements due to constraints of the experimental apparatus. The beam, formed by the finite width polycarbonate lens and used to illuminate the ground plane is distorted by diffraction for frequencies < 13 GHz and, at the other end of the spectrum, propagating fields become multimode within the planar waveguide for frequencies > 16 GHz.

To verify the predicted behavior of the ground-plane cloak design, we make use of a phase-sensitive, near-field microwave scanning system to map the electric field distribution inside a planar waveguide. The planar waveguide restricts the wave polarization to transverse electric. The details of the apparatus have been described previously [51]. A large area field map of the scattering region – including the collimated incident and scattered beams is shown in Fig.6.11. The waves are launched into the chamber from a standard X-band coax-to-waveguide coupler, and pass through a dielectric lens that produces a nearly collimated microwave beam. The beam is arbitrarily chosen to be incident on the ground plane at an angle of 40 degrees with respect to the normal. A flat ground plane produces a near perfect reflection of the incident beam in Fig.6.11A, while the presence of the perturbation produces considerable scattering in Fig.6.11B (note the presence of the strongly scattered secondary beam). By covering the space surrounding the perturbation with the metamaterial cloaking structure, however, the reflected beam is restored, as if the ground plane were flat in Fig.6.11C. The beam is slightly bent as it enters the cloaking region due to the refractive index change of the embedding material, but is bent back upon exiting. The gradient index IML introduced into the design minimizes reflections at the boundaries of the cloaking region.

As the ground-plane cloak makes use of non-resonant elements, it is expected to

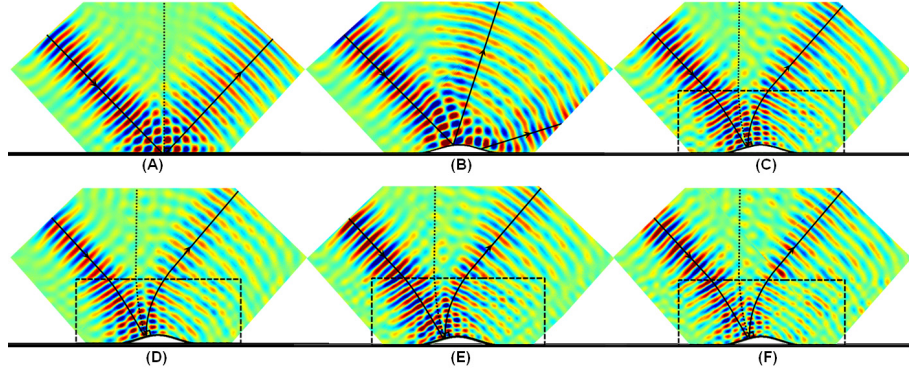


FIGURE 6.11: Measured field mapping (E-field) of the ground, perturbation and ground-plane cloaked perturbation. The rays display the wave propagation direction and the dash line indicates the normal of the ground in the case of free space and that of the ground-plane cloak in the case of the transformed space. (A) a collimated beam incident on the ground plane at 14GHz, (B) a collimated beam incident on the perturbation at 14GHz (control), (C) a collimated beam incident on the ground-plane cloaked perturbation at 14GHz, (D) a collimated beam incident on the ground-plane cloaked perturbation at 13GHz, (E) a collimated beam incident on the ground-plane cloaked perturbation at 15GHz, (F) a collimated beam incident on the ground-plane cloaked perturbation at 16GHz.[26]

exhibit a large frequency range of operation. The cloaking behavior was confirmed in our measurements from the range 13-16 GHz, though we expect the bandwidth to actually stretch to very low frequencies (less than 1 GHz) which cannot be verified experimentally due to limitations of the measurement apparatus and the beam forming lens. We illustrate the broad bandwidth of the cloak with the field maps taken at 13GHz in Fig.6.11D, 15GHz in Fig.6.11E and 16GHz in Fig.3F, which shows similar cloaking behavior to the map taken at 14 GHz in Fig.6.11C. The collimated beam at 16GHz has begun to deteriorate due to multi-mode propagation in our 2D measurement chamber, which is also observed in the flat ground plane control experiment at that frequency (not shown here). However, based on the predicted response of the broadband unit cells we expect this cloak to function up to approximately 18GHz.

With the same measurement in Fig.6.11, Fig.6.12 shows the measured field magnitude with and without ground-plane cloak. The data sets indicate the power flow in the sample (field magnitude squared is proportional to the power), providing the

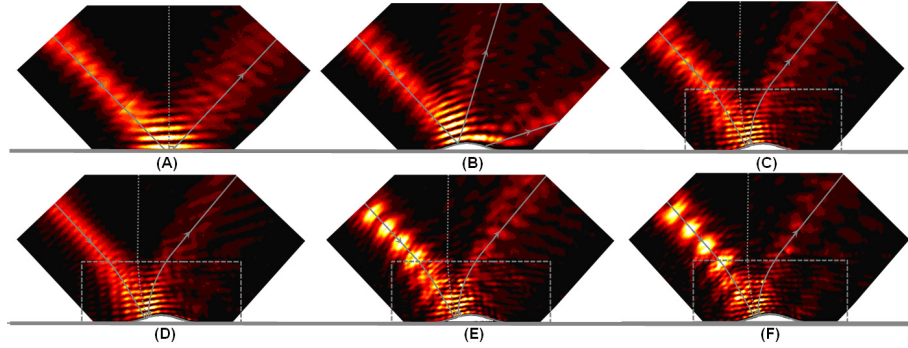


FIGURE 6.12: Measured field magnitude (E-field) of the ground, perturbation and ground-plane cloaked perturbation. The rays display the wave propagation direction and the dash line indicates the normal of the ground in the case of free space and that of the ground-plane cloak in the case of the transformed space. (A) a collimated beam incident on the ground plane at 14GHz, (B) a collimated beam incident on the perturbation at 14GHz (control), (C) a collimated beam incident on the ground-plane cloaked perturbation at 14GHz, (D) a collimated beam incident on the ground-plane cloaked perturbation at 13GHz, (E) a collimated beam incident on the ground-plane cloaked perturbation at 15GHz, (F) a collimated beam incident on the ground-plane cloaked perturbation at 16GHz.[26]

evidence of the cloaking functionality. The reflected beam for the ground plane is reduced somewhat from the incident beam for all of the scans, due to the non-ideal experimental condition at the conductive boundary and diffraction of the collimated beam. Note that the field magnitude measurement at 15GHz in Fig.6.12E and at 16GHz Fig.6.12F has a standing wave pattern for incoming and outgoing waves due to excitation of higher order modes that occurs at high frequencies in our near-field scanning apparatus; that is, the propagating wave is no longer confined to be Transverse Electric but also has a Transverse Magnetic component.

To visualize the performance of the ground-plane cloak, we illuminated the sample from the side (90 degrees from the surface normal) with a narrow collimated beam. As the ground-plane cloaked perturbation should also be cloaked with the respect to an observer located on the ground, the wave, which should follow the metric as defined by the quasi-transformation map in Fig.6.6, can be expected to detour around the perturbation and then return back to its original propagation direction. The

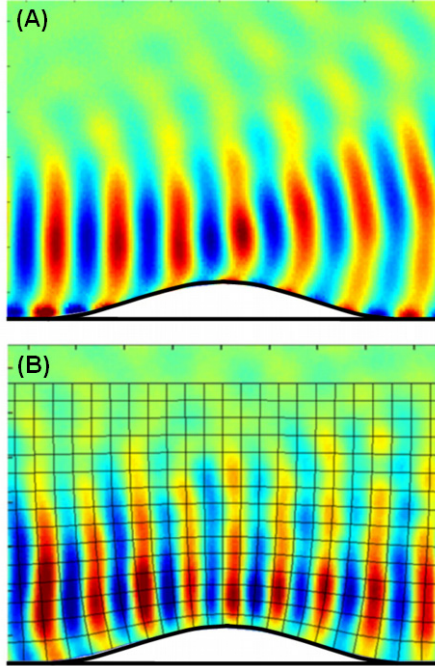


FIGURE 6.13: 2D field mapping (E-field) of the perturbation and ground-plane cloaked perturbation, illuminated by the waves from the left side (A) perturbation, (B) ground-plane cloaked perturbation. The grid pattern indicates the quasi-conformal mapping of the transformation optics material parameters.[26]

field map for this case is shown in Fig.6.13B, which corresponds with the predicted transformation extremely well (a low resolution representation of the transformation grid is overlaid on the experimental data). For comparison, Fig.6.13A shows a map of the field strongly scattered from the perturbation in the absence of the cloak.

To study the cloaking effect in more details, we conducted standing wave measurement and observe the intensity pattern within the transformed area on both control and the sample. In either of cases, the incident and the reflected waves produce a standing wave pattern that we use as a measure of the scattering produced by the perturbation on the ground plane. In the absence of the cloak, the ground plane is no longer flat, and the perturbation introduces a significant distortion into the standing wave pattern; in particular, the interference pattern is no longer parallel to the plane, as can be seen in Fig. 6.14a. However, when the ground plane cloak is present, the

perturbation is effectively removed from detection and the standing waves pattern is once again parallel with the ground, as shown in Fig. 6.14b. Moreover, since the cloak makes use of elements far away from resonance, the metamaterial cloak can be seen to have a large bandwidth, at least over the range 8-14.8 GHz confirmed in our experiment. The bandwidth of cloak is anticipated to stretch from very low frequencies (less than 1 GHz) to around 17 GHz, where the first resonance of the metamaterial elements occurs. The broad bandwidth of the cloak is illustrated by the power maps taken at 8 GHz in Figs. 6.14c,d, which show the identical behavior to the maps taken at 14 GHz.

In conclusion, the excellent agreement between the experiment and theoretical design verifies the novelty of transformation optics and the accuracy of rapid design system. According to the various experiment analysis, the coordinate space for electromagnetic waves can be effectively distorted at will by designing complex metamaterials. This compelling technology will be a crucial step towards to the optical cloaking devices design in the future and provide the opportunity of designing the large scale scatter system to manipulate electromagnetic waves in a novel manner.

Some of the work here has been published in Science[26].

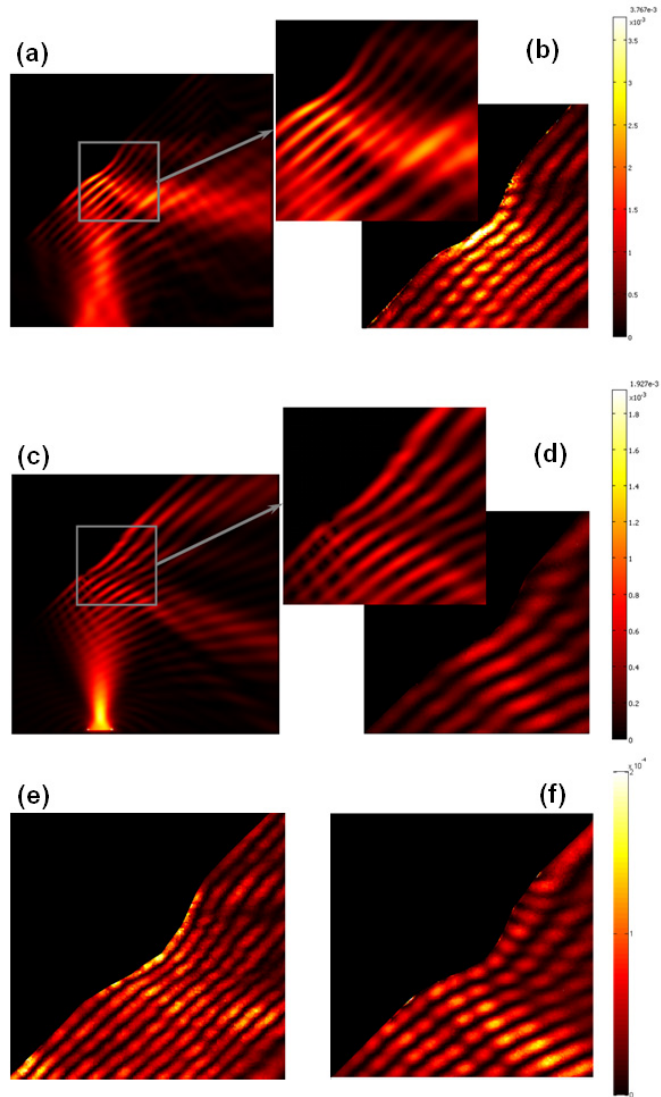


FIGURE 6.14: Power plot of the standing waves of the carpet cloak and control by simulation and experiment. (a) simulated power plot of only ground at 14GHz (b) simulated power plot of carpet cloak at 14GHz (c) simulated control scatter at 14GHz (d) experimental power plot of only ground at 14GHz (e) experimental power plot of carpet cloak at 14GHz (g) experimental power plot of control scatter at 8GHz (h) experimental power plot of carpet cloak at 8GHz[26]

Appendix A

Appendix A

Continuing the previous work[7], we start with the integral form of Maxwell's equations, and imagine averaging the fields over a unit cell. Then a finite-difference form of Maxwell's equations are derived, in which the averaged electric fields are defined on the edges of one cubic lattice, while the averaged magnetic fields are defined on the edges of a second offset lattice [7]. To simplify the analysis, we assume a wave whose electric field is polarized in the x direction and propagates along the z axis. The unit cell of the metamaterial is assumed to have a periodicity p . Under these conditions, one of the Maxwell curl equations reduces to

$$\begin{aligned}\bar{E}_x[(n + 1/2)p] - \bar{E}_x[(n - 1/2)p] &= i\omega\bar{\mu}p\bar{H}_y[np] \\ \bar{E}_x[(n + 1)p] - \bar{E}_x[np] &= i\omega\bar{\mu}_1p\bar{H}_y[(n + 1/2)p]\end{aligned}\tag{A.1}$$

in which $n = 0, \pm 1, \dots$, and the averaged electric field \overline{E}_x and magnetic field \overline{H}_y are defined by the line integrals

$$\begin{aligned}\overline{E}_x(z) &= \frac{1}{p} \int_{-p/2}^{+p/2} E(x, 0, z) dx, \\ \overline{H}_y(z) &= \frac{1}{p} \int_{-p/2}^{+p/2} H(0, y, z) dy.\end{aligned}\tag{A.2}$$

Under this form of averaging, the average permeability $\overline{\mu}$ has the form [8]

$$\begin{aligned}\overline{\mu} &= \frac{1}{p^2 \overline{H}_y(0)} \int_{-p/2}^{+p/2} \int_{-p/2}^{+p/2} \mu_a H(x, 0, z) dx dz, \\ \overline{\mu}_1 &= \frac{1}{p^2 \overline{H}_y(p/2)} \int_{-p/2}^{+p/2} \int_0^p \mu_a H(x, 0, z) dx dz.\end{aligned}\tag{A.3}$$

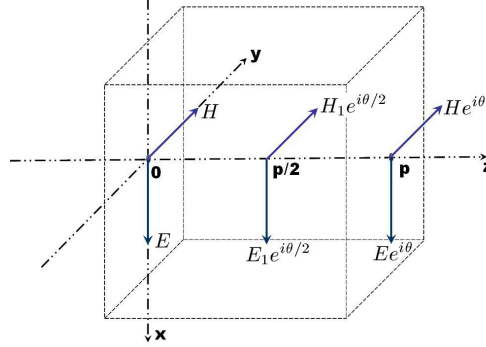


FIGURE A.1: Metamaterial composed of periodic particles, where a plane wave is incident along the z direction.

Similarly, the other Maxwell curl equation in integral form can be simplified to

$$\begin{aligned}\overline{H}_y[(n+1)p] - \overline{H}_y[np] &= i\omega \overline{\varepsilon} p \overline{E}_x[(n+1/2)p] \\ \overline{H}_y[(n+1/2)p] - \overline{H}_y[(n-1/2)p] &= i\omega \overline{\varepsilon}_1 p \overline{E}_x[np]\end{aligned}\tag{A.4}$$

after introducing the average permittivity

$$\begin{aligned}\bar{\varepsilon} &= \frac{1}{p^2 \bar{E}_x(0)} \int_{-p/2}^{+p/2} \int_{-p/2}^{+p/2} \varepsilon_a E(0, y, z) dy dz. \\ \bar{\varepsilon}_1 &= \frac{1}{p^2 \bar{E}_x(p/2)} \int_{-p/2}^{+p/2} \int_0^p \varepsilon_a E(0, y, z) dy dz.\end{aligned}\tag{A.5}$$

In Eqs.(A.1) and Eq.(A.4), ε_a and μ_a are the permittivity and permeability of the background medium. Eqs. (A.3) and Eqs.(A.5) together represent a discrete set of Maxwell's equations (DME).

In order that the DME represent an infinite periodic structure, we apply the Bloch boundary conditions shown in Fig.A.1, in which θ is the phase advance across one cell and E, E_1, H, H_1 represent the field average defined by Eq.(A.3). Substituting the boundary conditions into the DME, we obtain

$$\begin{aligned}2E \sin(\theta/2) &= \omega p \bar{\mu}_1 H_1 = \omega p \bar{\mu} H / F \\ 2H \sin(\theta/2) &= \omega p \bar{\varepsilon}_1 E_1 = \omega p \bar{\varepsilon} E / A \\ 2E_1 \sin(\theta/2) &= \omega p \bar{\mu} H = \omega p \bar{\mu}_1 H_1 F \\ 2H_1 \sin(\theta/2) &= \omega p \bar{\varepsilon} E = \omega p \bar{\varepsilon}_1 E_1 A\end{aligned}\tag{A.6}$$

in which, A and F are spatial dispersion factor of average parameters defined as

$$F = \frac{\bar{\mu} H}{\bar{\mu}_1 H_1} = \frac{B}{B_1}, \quad A = \frac{\bar{\varepsilon} E}{\bar{\varepsilon}_1 E_1} = \frac{D}{D_1}\tag{A.7}$$

Eq.(A.6) represent the ratio of electric and magnetic flux for different field average area. To model the periodic structure appropriately, we assume the unit cell sitting in the center of $z = p/2 + np$. According to the derivation in [7], the impedance varies periodically along propagation. Thus, the observation point is critical to impedance

calculation. To current configuration, the observation point should be at $z = np$, where the structure is not cut at the boundary if forming a slab. At the same time, only $\bar{\varepsilon}_1$ and $\bar{\mu}_1$ in concept represent the particle response, yielding generally the Lorentz resonance form.

According to Eq.(A.7)-Eq.(A.8), we derived the spatial dispersion and wave impedance as

$$\begin{aligned}
\sin(\theta/2) &= S_d \omega p \sqrt{\bar{\mu}_1 \bar{\varepsilon}_1} \sqrt{AF}/2 \\
&= S_d \omega p \sqrt{\bar{\mu}_m \bar{\varepsilon}_m} \cos(\theta/2)/2 \\
\eta = \frac{E}{H} &= \sqrt{\frac{A}{F}} \cdot \sqrt{\frac{\bar{\mu}_1}{\bar{\varepsilon}_1}} = \sqrt{\frac{\bar{\mu}_m}{\bar{\varepsilon}_m}}
\end{aligned} \tag{A.8}$$

in which $S_d = 1$ or -1 depending on the restriction of positive imaginary part of θ . A and F are spatial dispersion factors, grouping together with $\bar{\varepsilon}_1$ and $\bar{\mu}_1$ and taking into account the spatial dispersion to particle response average parameters. $\bar{\varepsilon}_m$ and $\bar{\mu}_m$ are the transformation and grouped form of effective average parameters due to the spatial factor A and F .

According to Eq.(A.9), we achieve that

$$\begin{aligned}
\bar{\varepsilon}_m &= \bar{\varepsilon}_1 F / \cos(\theta/2) \\
\bar{\mu}_m &= \bar{\mu}_1 A / \cos(\theta/2) \\
\bar{\varepsilon} &= AF \bar{\varepsilon}_1 \\
\bar{\mu} &= AF \bar{\mu}_1
\end{aligned} \tag{A.9}$$

and a new set of general solutions after the equivalent transformation for the average parameters,

$$\begin{aligned}\tan(\theta/2) &= S_d \omega p \sqrt{\bar{\mu}_m \bar{\epsilon}_m} / 2 \\ \eta &= \sqrt{\frac{\bar{\mu}_m}{\bar{\epsilon}_m}}\end{aligned}\tag{A.10}$$

To characterize the spatial dispersion factors A and F , we consider the following fundamental propagation modes based on the definitions from Eq.(A.5)(A.6) and (A.9):

For homogeneous cases, both E and H fields propagate sinusously and, A and F can be easily extracted that $A = 1$ and $F = 1$ according to this plane wave propagation.

For magnetic resonators, we can refer the assumption in Ref.[7] that the magnetic and electric field are off-set due to the strong magnetic resonance by the structure. The magnetic field yields the uniform phase within the region from $z = np$ to $z = (n+1)p$ and has the phase shift θ every next unit cell region. Thus, the derived A and F are $A = 1/\cos(\theta/2)$ and $F = \cos(\theta/2)$. Substitute this A and F , we can reconstruct the identical formulas in Ref.[7]. We notice that this assumption is made because of the intuition that the strong resonant unit cell dominates the phase distribution and should yield an approximated step function in the periodic system. However, the rigorous proof cannot be made under the field averaging scheme because of the lack of the physical model. Here, we will use an imperial observation from a full wave simulation on an array of SRRs to approximate the A and F value.

For electric resonators, the similar analysis, compared with the magnetic resonators, can be made that $A = \cos(\theta/2)$ and $F = 1/\cos(\theta/2)$. The identical formulas can still be generated corresponding to the electrical particle case in Ref.[7].

However, for magnetic and electric combination resonators, we do not have detailed information on the electric and magnetic field distribution because of the model

itself constrains us to the level of lattice but no connection to the unit cell. The intuition here is to make a similar assumption inspired by Ref.[7] to find a formula that can possibly fit the response to the complex metamaterial unit cell, though the assumption itself cannot be proved or is even unphysical. Thus, we can temporarily assume that the electric and magnetic field are no longer off-set but yielding uniform phase within one unit cell region from $z = np$ to $z = (n + 1)p$ and the phase shift θ every next unit cell region. Thus, the A and F are

$$\begin{aligned} A &= \cos(\theta/2) \\ F &= \cos(\theta/2) \end{aligned} \tag{A.11}$$

Substitute Eq.(A.12) to Eq.(A.9), we hope that Eq.(A.11) can provides a linkage between the particle response and system behavior for more complicated structure. We also know an important fact from mathematics that no matter which cases for A and F in Eq.(A.10), as long as the average parameters $\bar{\epsilon}_1$ and $\bar{\mu}_1$ have the Lorentz resonance form, the effective average parameters $\bar{\epsilon}_m$ and $\bar{\mu}_m$ will also yield the Lorentz resonance like form but different in value (the resonant frequency will shift to critical frequency defined in Ref.[7]). Therefore, Eq.(A.10) indicates that $\bar{\epsilon}_m$ and $\bar{\mu}_m$ can be possibly an artificial Drude-Lorentz resonance like response to a wide types of metamaterial structures and can be used to analyze complex metamaterial unit cell. The advantage of using Eq.(A.10) to fit the unit cell's response is because the pre-requirement of restricting particle to be an electric or magnetic resonator is no longer needed.

Based on Eq.(A.11), one of the most direct applications is to do a particle response retrieval for complicated structure. The effective parameters θ and η can be achieved through standard retrieval process[6]. Then we can back up the particle response $\bar{\epsilon}_m$ and $\bar{\mu}_m$ through Eq.(A.13), which are supposed to be multiple resonant Lorentz form under our assumption.

$$\begin{aligned}\bar{\epsilon}_m &= \frac{\tan(\theta/2)}{\theta/2} \epsilon_{eff} \\ \bar{\mu}_m &= \frac{\tan(\theta/2)}{\theta/2} \mu_{eff}\end{aligned}\tag{A.12}$$

The particle response retrieval can dramatically reduce the complexity in designing a unit cell, especially for combination structures such as SRR-ELC, in which, two different resonators interact strongly and experience severe spatial dispersion with each other. Moreover, one can also easily use Drude-Lorentz model to fit the average parameters and back up accurate fitting of effective permittivity and permeability using the formulas that

$$\begin{aligned}\epsilon_{eff} &= \frac{\theta/2}{\tan(\theta/2)} \bar{\epsilon}_m \\ \mu_{eff} &= \frac{\theta/2}{\tan(\theta/2)} \bar{\mu}_m\end{aligned}\tag{A.13}$$

in which

$$\begin{aligned}\bar{\epsilon}_m &= \epsilon_a \left(1 - \sum_i \frac{F_{ei} f^2}{f^2 - f_{ei}^2 + i\gamma_{ei} f} \right) \\ \bar{\mu}_m &= \mu_a \left(1 - \sum_i \frac{F_{ui} f^2}{f^2 - f_{ui}^2 + i\gamma_{ui} f} \right)\end{aligned}\tag{A.14}$$

Bibliography

- [1] J. B. Pendry, A. J. Holden, D. J. Robbins, IEEE Trans. Microwave Theory and Tech. **47**, 2075 (1999).
- [2] D. R. Smith, D. C. Vier, N. Kroll and S. Schultz Appl. Phys. Lett., 77, 2246 (2000)
- [3] D. R. Smith, D. C. Vier, Th. Koschny, C. M. Soukoulis, Physical Review E, 71, 036617 (2005)
- [4] C. R. Simovski, arXiv:cond-mat/0606622 v1 (2006).
- [5] D. R. Smith, J. B. Pendry Journal of the Optical Society of America B 23, 321 (2006).
- [6] T. Koschny, P. Markos, D. R. Smith and C. M. Soukoulis Phys. Rev. E, 68, 065602 (2003)
- [7] R. Liu, T.J. Cui, D.Huang,B.Zhao, D.R. Smith, Phys. Rev. E **76**, 026606 (2007)
- [8] C. R. Simovski, S. A. Tretyakov, Phys. Rev. B 75, 195111 (2007).
- [9] V. G. Veselago, Sov. Phys. Usp. **10**, 509 (1968).
- [10] D. R. Smith, W. J. Padilla, D. C. Vier, S. C. Nemat-Nasser, S. Schultz, Phys. Rev. Lett. **84**, 4184 (2000).
- [11] R. A. Shelby, D. R. Smith and S. Schultz, Science **292**, 77 (2001)
- [12] Simovski, C. R. and S. He, Phys. Lett. A 311, 254, 2003.
- [13] Chen, H., L. Ran, J. Huangfu, X. Zhang, K. Chen, T. M. Grzegorzcyk, and J. A. Kong, Phys. Rev. E **70**, 057605 (2004)
- [14] J. B. Pendry, Phys. Rev. Lett. **85**, 3966 (2000).

- [15] N. Garcia¹ and M. Nieto-Vesperinas, Phys. Rev. Lett. **88**, 207403 (2002)
- [16] D. Schurig, D. R. Smith, Physical Review E, **70**, 065601(R) (2004)
- [17] N Fang, H Lee, C Sun, X Zhang, Science, Vol. 308. no. 5721, pp. 534-537 (2005)
- [18] D. R. Smith and D. Schurig, Phys. Rev. Lett., 90, 77405 (2003)
- [19] D. R. Smith, D. Schurig, J. J. Mock, P. Kolinko, P. Rye, Applied Physics Letters, **84**, 2244 (2004)
- [20] D. R. Smith, J. J. Mock, A. F. Starr, D. Schurig, Physical Review E , **71**, 036617 (2005)
- [21] T. J. Yen, W. J. Padilla, N. Fang, D. C. Vier, D. R. Smith, J. B. Pendry, D. N. Basov, X. Zhang, Science, **303**, 1494 (2004)
- [22] H.T. Chen W. J. Padilla J. M. O. Zide Arthur, C. G, Antoinette J. Taylor, R. D. Averitt, Nature **444**, 597 - 600 (2006).
- [23] J. Zhou, Th. Koschny, M. Kafesaki, E. N. Economou, J. B. Pendry, and C. M. Soukoulis, Phys. Rev. Lett. **95**, 223902 (2005)
- [24] J. B. Pendry, D. Schurig, D. R. Smith, Science **312**, 1780 (2006)
- [25] D. Schurig, J. J. Mock, B. J. Justice, S. A. Cummer, J. B. Pendry, A. F. Starr and D. R. Smith, Science **314**, 977-980 (2006).
- [26] R. Liu, C. Ji, J. Mock, J. Y. Chin, T. J. Cui and D. R. Smith, Science **323**, 366-369 (2009)
- [27] U. Leonhardt, Science 312, 1777 (2006), published online 24 May 2006; 10.1126/science.1126493
- [28] M. Rahm, S. A. Cummer, D. Schurig, J. B. Pendry, D. R. Smith, Phys. Rev. Lett. 100, 063903 (2008).
- [29] M. Rahm et al ., Opt. Express 16, 11555 (2008).
- [30] A. V. Kildishev, V. M. Shalaev, Opt. Lett. 33, 43 (2008).
- [31] M. Rahm et al., Phot. Nano. Fund. Appl. 6, 87 (2008).

- [32] W. X. Jiang et al., Appl. Phys. Lett. 92, 264101 (2008).
- [33] Z. Ruan, M. Yan, C. W. Neff, M. Qiu, Phys. Rev. Lett. 99, 113903 (2007).
- [34] A. Hendi, J. Henn, U. Leonhardt, Phys. Rev. Lett. 97, 073902 (2006).
- [35] T. Koschny, P. Markos, D. R. Smith and C. M. Soukoulis, Phys. Rev. E, 68, 065602 (2003)
- [36] R. A. Depine, A. Lakhtakia, Phys. Rev. E **70**, 048601(2004).
- [37] A. L. Efros, Phys. Rev. E **70**, 048602 (2004).
- [38] D.R.Smith,unpublished (2009).
- [39] V. Varadan, Z. Sheng, S. Penumarthy and S. Puligalla, Microwave Opt. Tech. Lett. **48**, No. 8 (2006).
- [40] T. Koschny, P. Markos, E. N. Economou, D. R. Smith, D. C. Vier, C. M. Soukoulis, Phys. Rev. B **71**, 245105 (2005).
- [41] J. M. Lerat, N. Mallejac, O. Acher, J. Appl. Phys. **100**, 084908 (2006).
- [42] J. Garcia-Garcia, F. Martin, J. D. Baena, R. Marques, L. Jelinek, J. Appl. Phys. **98**, 033103 (2005).
- [43] P. A. Belov, C. R. Simovski, S. A. Tretyakov, Phys. Rev. E **67**, 059902 (2003).
- [44] R. Liu, B. Zhao, X. Q. Lin, Q. Cheng, T. J. Cui,Phys. Rev. E, Vol. 76, 026606,(2007)
- [45] K. S. Yee, IEEE Trans. Antennas Propag. **14**, 302 (1966).
- [46] D. Schurig, J. J. Mock, D. R. Smith, Applied Physics Letters 88, 041109 (2006)
- [47] R. B. Greigor, C. G. Parazzoli, J. A. Nielsen, M. A. Thompson, M. H. Tanielian, D. R. Smith, Appl. Phys. Lett. **87**, 091114 (2005).
- [48] T. Driscoll, D. N. Basov, A. F. Starr, P. M. Rye, S. Nemat-Nasser, D. Schurig, D. R. Smith, Appl. Phys. Lett. **87**, 081101 (2006).
- [49] R. Liu, A. Degiron, J. J. Mock, and D. R. Smith, Appl. Phys. Lett. **90**, 263504 (2007)

- [50] C. R. Simovski, S. He, Phys. Lett. A 311, 254 (2003).
- [51] B. J. Justice, J. J. Mock, L. Guo, A. Degiron, D. Schurig, D. R. Smith, Optics Express 14, 8694 (2006)
- [52] L. L. Hou, J. Y. Chin, X. M. Yang, X. Q. Lin, R. Liu, F. Y. Xu, and T. J. Cui, "Advanced parameter retrievals for metamaterial slabs using an inhomogeneous model", J. Appl. Phys. 103, 064904 (2008);
- [53] W. J. Padilla, M. T. Aronsson, C. Highstrete, M. Lee, A. J. Taylor, R. D. Averitt, Phys. Rev. B **75**, 041102 (2007)
- [54] R. Liu, Q. Cheng, J. Y. Chin, J. J. Jack, T. J. Cui and D. R. Smith, Optics Express 17, 21030 (2009)
- [55] J. Valentine, J. Li, T. Zentgraf, G. Bartal, and X. Zhang, Nature Mater. 8, 568-571 (2009)
- [56] L. H. Gabrielli, J. Cardenas, C. B. Poitras, and M. Lipson, Nat. Photonics 3, 461 (2009)
- [57] F. Falcone etc. Phys. Rev. Lett. 93, 197401 (2004).
- [58] R. Liu, X. M. Yang, J. N. Gollub, J. J. Mock, T. J. Cui, D. R. Smith, Applied Physics Letters 94, 073506 (2009)
- [59] Q. Cheng, R. P. Liu, J. J. Mock, T. J. Cui, D. R. Smith, Physical Review B 78, 121102 (2008)
- [60] R. Liu, et.al., Phys. Rev. Lett. 100, 023903 (2008)
- [61] S. Enoch et al., Phys. Rev. Lett. **89**, 213902 (2002).
- [62] A. Lai, C. Caloz, and T. Itoh, Microwave Magazine, vol. 5, no. 3, pp. 34-50, (2004)
- [63] M. Silveirinha and N. Engheta, Phys. Rev. Lett. 97, 157403 (2006).
- [64] P. A. Belov et al., Phys. Rev. B **67**, 113103 (2003)
- [65] R. E. Collin, Problem 8.2, Field Theory of Guided Waves, 2nd ed., New York: IEEE. Press, 1990

- [66] A. P. Hibbins, M. J. Lockyear, J. R. Sambles, *J. Appl. Phys.* 99, 124903 (2006)
- [67] Q. Cheng, R. Liu, D. Huang, T. J. Cui, D. R. Smith, *Applied Physics Letters* 91, 234105 (2007)
- [68] W. E. Kock, *Metallic delay lenses*, *Bell System Technical J.* 27, 58 (1948)
- [69] R. W. Corkum, *Proceedings of the IRE* 40, 574 (1952).
- [70] J. Brown and W. Jackson, *Proc. IEE paper no.1699R vol. 102B pp. 11-21* , January 1995.
- [71] I. Bahi, K.Gupta, *IEEE Trans. Ant. and Prop.* 22, 119-122 (1974).
- [72] Y. Mukoh, T. Nojima, N. Hasebe, *Electronics and Communications in Japan, Part 1* 82, (1999).
- [73] I. Awai, H. Kubo, T. Iribe, D. Wakamiya, and A. Sanada, *Microwave Symposium Digest, 2003 IEEE MTT-S International 2* 1085-1088 (2003).
- [74] I. Awai, S. Kida, and O. Mizue, *Korea-Japan Microwave Conference* 177-180 (2007).
- [75] I. Awai, *IEEE Microwave Magazine* 9, 55-64 (2008).
- [76] Y. Ma, B. Rejaei, Y. Zhuang, *IEEE Microwave and Wireless Components Letters* 19, 431-433 (2008).
- [77] J.B. Pendry and S. Anantha Ramakrishna, *J. Phys.: Condens. Matter* 15 6345 (2003)
- [78] S. Guenneau, B. Gralak and J.B. Pendry, *Opt. Lett.*, Vol. 30, 1204 (2005)
- [79] R. Liu, C. Ji, et.al., *2008 International Workshop on Metamaterials, Nanjing, China, Nov.10-12, (2008).*
- [80] J. Li and J. B. Pendry, *Phys. Rev. Lett.* 101, 203901 (2008).
- [81] J. F. Thompson, B. K. Soni, N. P. Weatherill, *Handbook of Grid Generation* (CRC Press, Boca Raton, 1999).

Biography

Ruopeng Liu receives his Ph.D. from the Department of Electrical and Computer Engineering at Duke University in 2009. He was born in Xi'an, China, on September 24th, 1983. He has been working on metamaterial research with Professor David R. Smith since 2006. Prior to Duke University, he received his B.S. degree at Zhejiang University in China in 2006.